

Gas Giants from a Protoplanetary Disk

Thesis report
A. M. M. Blekman

Technische Universiteit Delft

Gas Giants from a Protoplanetary Disk

Thesis report

by

A. M. M. Biekman

to obtain the degree of Master of Science
at the Delft University of Technology,
to be defended publicly on Monday July 15, 2019 at 14:00 PM.

Student number:	4109937	
Project duration:	August 28, 2018 – July 2, 2019	
Thesis committee:	Dr. S. M. Cazaux,	TU Delft, supervisor
	Prof. Dr. L. L. A. Vermeersen,	TU Delft
	Dr. A. Menicucci,	TU Delft
	Dr. Y. Miguel,	Leiden University

An electronic version of this thesis is available at <http://repository.tudelft.nl/>.

Cover image taken from <https://www.almaobservatory.org/en/press-release/revolutionary-alma-image-reveals-planetary-genesis/>. Credit: ESO/L. Calçada

Preface

"I am making planets." That is what I told anyone who asks me what I am doing, how I'm doing or even what time it is. This is one of the things that I will miss after finishing up this thesis project. This project has been very informative for me and I learned many things. I chose this project because I wanted to make a contribution to the body of knowledge about the origin of planets. To be honest, I was also a bit reluctant to graduate. For that I can thank my supervisor Stephanie Cazaux, for her very energetic and active supervision of my thesis project. Besides that I also have to thank her for getting me introducing me to ProDiMo and the development team. Yamila Miguel played a very important role in pointing me in the direction of pebble accretion. I also appreciated the feedback and critical questions I got during my mid-term review from Daphne Stam, and the spontaneous meetings with Inga Kamp. I also want to thank my friends of the ninth floor for their company and fun times during my time in the thesis room: Henno, Palash, Valerio, Caroline, Frederic, Viktor, Max, Datta, Corné, Hanneke, Maaïke, Sunayna, Rosalie and Matteo. I want to thank my family for their support during my thesis. Even though their scientific expertise could not help me forward, conversations with them always lead to a better insight on how to handle it.

*A. M. M. Biekman
Delft, July 2019*

Contents

List of Figures	vii
List of Tables	xi
Nomenclature	xiii
Summary	xvii
1 Introduction	1
1.1 Research questions	1
2 Physics and Chemistry: From PPD to planets	3
2.1 Formation of a PPD	3
2.2 Disk structure and dynamics	6
2.2.1 Dust and gas structure	6
2.2.2 Gas and dust dynamics	7
2.2.3 Planet migration	7
2.3 Radiation and disk chemistry	8
2.3.1 Sources of radiation	8
2.3.2 Gas chemistry	9
2.3.3 Grain surface chemistry	9
2.4 Giant Planet formation	10
2.5 Observations	11
2.5.1 PPD observations	11
2.5.2 Observations of gas giants	11
3 Software:ProDiMo	13
3.1 Global structure of ProDiMo	13
3.1.1 Structure	13
3.1.2 Radiation field	14
3.1.3 Chemistry	15
3.1.4 Gas thermal balance	16
3.2 Grain surface chemistry	16
3.3 Time dependent disk model	16
4 A typical ProDiMo Model	19
4.1 Simple temperature and surface density fits	19
4.2 Disk compositions	23
4.3 Working model: AA Tau	26
5 Formation of planets	31
5.1 Pebble accretion	31
5.1.1 Dust evolution	31
5.1.2 Pebble drift and (solid) surface density	32
5.1.3 Core growth	35
5.2 ProDiMo disk model modifications	37
5.3 Gas giant atmospheres	41
6 Planet composition	47
6.1 Pebble core compositions	47
6.2 Atmosphere composition	55
6.3 C/O ratio of the atmosphere	57
6.3.1 C/O of the cores	57
6.3.2 Tracing atmospheres to location of formation	58

7 Discussion	65
7.1 Composition	65
7.2 Pebble accretion model	66
7.3 Discussion of the C/O ratios	66
8 Conclusions and Recommendations	69
Bibliography	71
A Input files ProDiMo	75
B Core and atmosphere compositions	81
B.1 Core compositions	81
B.2 Atmosphere compositions	84

List of Figures

2.1	Four images showing different stages in the process of forming a PPD.	4
2.2	Sketches of the evolution of a PPD at different stages.	5
2.3	Graphic of a protoplanetary disk surrounding a protostar, from Henning and Semenov (2013). The left-hand side shows some aspects of the disk solids structure and dynamics, the right-hand side shows the volatiles temperature structure and chemical conditions. In the centre the protostar is shown with the magnetic field and a accretion region in green.	6
2.4	Simulations of type-I and type-II migration from Chambers (2009). The figures have the planet in the centre. The black regions on the left-hand-sides of the figures are not empty but left out of the simulation. The same hold s for the right-hand black region of the left figure. Credit:Pawel Artymowicz.	8
2.5	Chemical processes that take place on dust grains. In this figure the products of each reaction are singular and in gas phase for clarity of the figure. However, the three reactions on the right hand side can result in multiple products, each of which can be in gas-phase or in the form of ice.	10
2.6	Graphics describing how observations of transits can provide information about exoplanets.	12
3.1	Flow diagram of the global code structure of ProDiMo, adjusted from Rab (2018). The solid blue arrows indicate the sequence that is used in case of opted for no iterations. The dotted blue arrows are optional module paths and the red arrows mean that iterations are used inside of the module to make it self-consistent. The left-hand yellow boxes are a selection of the input data for the modules in the blue boxes. The bottom green box is an optional module.	14
3.2	Grid point distribution and density distribution of the disk.	15
3.3	Comparison of H ₂ O (gas) abundances of a disk without (left) and with (right) surface chemistry using ProDiMo disk models. Credits: W.-F. Thi.	17
4.1	Aperture synthesis images of submillimeter continuum emission for the AA Tau, DR Tau, RY Tau and WaOph 6 disks. The contours indicate the intensity, beginning at 3 σ and each following contour has a step of 2 σ . The ellipse in the left lower corner of each image represent the Full width at half maximum (FWHM) dimensions and orientations of the naturally weighted synthesised beams. Combined figure from Andrews and Williams (2007).	20
4.2	Mid-plane temperature profiles for the dust(left) and the gas(right) as computed by ProDiMo as the solid green, dash-dotted blue and dashed purple lines for case 1, 2 and 3 respectively, for 4 different disks. The reference temperature profiles from the Lewis (1974) simple solutions are indicated by the dotted black lines. In addition the error bars of the mid-plane temperatures at 1 AU are shown.	22
4.3	Surface density profiles as computed by ProDiMo as the solid red, green, yellow and purple lines for case 1, 2, 3 and 4 respectively, for 4 different disks. The reference surface density profiles from the Lewis (1974) simple solutions are indicated by the dotted black lines. In addition the error bars of the surface density at 1 AU are shown.	24
4.4	Recreation of the C/O ratio in the mid-plane as seen in Öberg <i>et al.</i> (2011). The thick solid line shows the C/O ratio in the gas phase, the dashed line is the C/O ratio in the grains and the dotted line indicates the solar C/O ration of 0.5455 for reference. The snowlines for H ₂ O, CO ₂ and CO are indicated from left to right.	25

4.5	SED fitted by <i>Woitke et al. (2019)</i> . The red line is the stellar fit, the black dotted line with black circles is the fitted PPD including the star. The coloured diamonds are the observations and the dark green line is the UV data. In addition IR observation from the Spitzer telescope that are used to fit the SED of the PPD is shown in orange.	27
4.6	Properties of the ProDiMo AA Tau model: gas to dust ratio, number of H nuclei $n_{<H>}$, Midplane temperatures, and the mid-plane C/O.	28
5.1	Schematic of the development of a PPD forming planets through pebble accretion. Each bar represents a specific time in the disk. The purple dashed line represents the pebble production line as described in subsection 5.1.1. The red dashed rectangles are used to describe where the composition of the ices comes from.	32
5.2	Solid surface densities of L&J14 for different times. The solid lines represent the dust surface density and the dotted lines are the pebble surface densities.	34
5.3	Visualisation of different pebble sizes passing a planetary core from <i>Lambrechts and Johansen (2012)</i> . Black lines are pebbles with $S_t = 1$, and are all accreted by the core, grey lines indicate pebbles with $S_t = 0.01$ (solid) and $S_t = 1$ (dashed) of which only some of the pebbles are accreted depending on the distance x/r_H at which the core is passed.	36
5.4	Reproduction of core growth over time as calculated by (<i>Lambrechts and Johansen, 2014</i>). The circles on the first two cores indicate the isolation of the core from pebbles to halt the mass growth. The dashed lines are the paths the mass would have followed if the core would continue accreting the pebbles that are drifting by after pebble isolation. The shaded region on the right hand side of the plot indicates that the gas t exceeds the disk dissipation time scale τ_{disk}	38
5.5	Initial gas and dust surface densities of <i>Lambrechts and Johansen (2014)</i> and ProDiMo.	39
5.6	Solid surface densities of <i>Lambrechts and Johansen (2014)</i> on the left and ProDiMo on the right, for different times. The solid lines represent the dust surface density and the dotted lines are the pebble surface densities.	40
5.7	Core growth over time for the AA Tau evaluated with both the Σ calculated by ProDiMo and the simple exponential Σ	41
5.8	Mass evolution with adjusted coagulation efficiency and dust to gas mass ratio respectively.	42
5.9	Mass evolution for Disk 1 with $Z_0=0.03$, and $\epsilon_{d,g} = \epsilon_p = 0.17$ at several radii.	43
5.10	Final core mass as a function of the radius.	43
5.11	Flow diagram of the method used to compute the Planet mass when it forms a gap of $2r_H$ at the radius of core formation.	44
5.12	The dashed blue line is the core mass, the dotted black line is the mass of the atmosphere, and the solid red line is the total planet mass.	45
6.1	Flow diagram of the calculation of composition of the core mass accreted through pebble accretion.	48
6.2	Core mass evolution for formation radii specified in the legend. The dashed s indicates the mass evolution path without pebble isolation. The solid lines are the mass evolution paths of the different cores, and the circles indicate the isolation time an mass if it is reached.	49
6.3	Abundance of the columns of the ices represented most in the core formed via pebble accretion. The unit of the colorbar is $\log_{10}(n_x/n_{<H>})$. The red lines indicate the ice-lines of the species.	50
6.4	Origin of the pebbles accreted as function of radius and time of accretion. The markers indicate where and when the last pebbles to be accreted originate.	51
6.5	Origin of the pebbles accreted as function of radius and time of accretion. The scale is applied so that it can easily be compared to the composition panels in Figure 6.3.	51
6.6	Core composition found by the planetesimal accretion scenario for different accretion radii. In the upper left corner dust and ice percentages are shown	52

6.6	Core composition found for the pebble accretion scenario on the left and the planetesimal accretion scenario for different accretion radii. In the upper left corner of each panel the dust and ice percentages of the total core mass are shown. The large pie charts show the mass percentage of the ice in the core.	53
6.7	Gas compositions of the formed giant planets.	55
6.8	Column density evolution of the species most common in the atmospheres shown in Figure 6.7a.	60
6.9	C/O of the disk gas over the total disk height and the atmospheres of the formed gas giants.	61
6.10	C/O of the total disk height in the gas as function of time and radial distance. The colour is scaled up to 15, so the bright yellow region is means that the C/O is 15 or higher (also see Figure 6.9).	61
6.11	C/O of the total disk height in the ice is shown as the dotted and solid lines from light blue to dark blue, the cores formed via pebble accretion indicated by red triangles and the planetesimal cores as red squares. The selected core formation locations are indicated by a black edge of the mark.	62
6.12	C/O in the disk ices as function of time and radial distance.	62
6.13	C/O of the atmospheres with and without core ices dissolved into the atmosphere. . . .	63
6.14	Core mass fraction of the total planet mass.	63
7.1	$(C/O)_{planet}/(C/O)_{stellar}$ of the atmospheres. The black dotted line with asterisks represents the isolated atmosphere, the blue triangles are the atmosphere mixed with the ices of the core formed from pebble accretion, the atmosphere mixed with the planetesimal core ices is shown as the magenta squares. In addition the mean of the observed values from Brewer <i>et al.</i> (2017) is given as the blue dotted line, with the error margins as the orange areas.	68

List of Tables

4.1	Input parameters for the simulations of the AA Tau, DR Tau, RY Tau and WaOph 6 disks that have differences between disks. The gray boxes indicate that no value was found for and that the standard T Tauri value of pre-programmed in ProDiMo was assumed.	21
4.2	Dust sizes for the different cases.	23
4.3	Abundances and evaporation temperatures of C- and O-bearing species. In the cases where a range is indicated the value in parentheses is used.	25
5.1	Input parameters for the core growth Lambrechts and Johansen (2014)	37
5.2	Core theoretical core isolation mass $M_{c,isco}$, computed isolation time t_{iso} and the final mass at 3Myr. 'no iso' indicates that the isolation mass is not reached in the first 10 Myr.	37
5.3	Core isolation masses with times if they are reached. The mass at 3 Myr is also shown in the columns $M_{c,3Myr}$	39
A.1	List of the species considered in the model AA Tau by ProDiMo.	79
B.1	List of all ice species for cores in percentages.	83
B.2	List of the most abundant species in the atmospheres in percentages	84
	List of symbols	

Nomenclature

Roman Symbols

\dot{M}_c	Core mass accretion rate	M_\oplus/yr
\dot{M}_{peb}	Pebble flux throughout the disk	M_\oplus/yr
a	Semi major axis	s
A_v	Extinction	\square
c_s	Speed of sound	m/s
H	Scale height	m
M_*	Central star mass	M_\odot
M_c	Core mass	M_\oplus
n	Number density	cm^{-3}
P	Pressure	erg/m^2
r_g	Pebble production front line	m
R_H	Hill radius	m
T	Temperature	K
t	Time variable	s
v_H	Particle velocity at the edge of the Hill sphere	m
v_{kep}	Keplerian orbital velocity	m/s

Greek Symbols

β	Normalisation constant	kg/m^2
ϵ_d	Dust growth parameter	-
ϵ_p	Pebble coagulation efficiency	-
$\epsilon_{g,d}$	Dust coagulation efficiency	-
η	Radial gas pressure support	-
Ω_K	Keplerian frequency	s^{-1}
ρ	Density	kg/m^3
Σ	Surface density	kg/m^2
τ_{KH}	Kevin-Helmoltz time scale	yr
ξ	particle growth parameter	-
S_t	Stokes number	-

Constants

c	Speed of light in vacuum	2.99792458×10^8 m/s
G	Gravitational constant	$6.6725985 \times 10^{-11}$ m ³ kg ⁻¹ s ⁻²
M_{\odot}	Solar mass	1.9889225×10^{30} kg
M_{\oplus}	Earth mass	5.9742×10^{24} kg
Å	Angström	10^{-10} m
AU	Astronomical unit	1.4959787×10^{11} m
pc	Parsce	$3.085680250 \times 10^{18}$ m

Elements & molecules

Al	Aluminium
AR	Argon
C	(Atomic) Carbon
C ₂	(Molecular) Carbon
Ca	Calcium
CH ₄	Methane
CO	Carbon monoxide
CO ₂	Carbon dioxide
Fe	Iron
H	(Atomic) Hydrogen
H ₂	Molecular Hydrogen
H ₂ O	Water
HCN	Hydrogen cyanide
He	Helium
K	Potassium
Mg	Magnesium
N	Nitrogen
Na	Sodium
Ne	Neon
NH ₃	Ammonia
Ni	Nickel
O	Oxygen
O I	Atomic oxygen
O ₂	(Molecular) oxygen
S	Sulphur
Si	Silicon

Ti	Titanium
TiO	Titanium monoxide
V	Vanadium
VO	Vanadium monoxide

Acronyms

IR	Infrared
ISM	Interstellar Medium
MMSN	Minimum Mass Solar Nebula
PAH	Polycyclic Aromatic Hydrocarbon
PPD	Protoplanetary Disk
SED	Spectral Energy Distribution
SPH	Smooth Particle Hydrodynamics
UV	Ultra Violet
YSO	Young Stellar Object

Summary

The Earth is not the only planet in the universe. It has been known for millennia that there are other planets and other bodies in the solar system. Moreover, as recent as, 1995 it has been confirmed that other stars also host planets. But how did they form? This is the main question that planet formation research has been trying to answer for at least a century. Since planet formation can not be observed directly due to instrumental limitations and limitations on human life times, this takes many generations. Each project contributing a small part to the puzzle that is planet formation. This thesis aims to address a small part of this puzzle.

Planets are formed from same material as their host star. Interstellar space houses vast clouds of gas and dust. Under the influence of interstellar radiation, turbulence, magnetic fields, gravity and gas dynamics, pockets of higher density are formed in these clouds, called molecular cloud cores. Upon the collapse of a molecular cloud core (MCC), the material in the MCC will divide itself between the central body, the protostar, and a disk of material orbiting the protostar. This disk is mostly made up of gas and $\sim 1\%$ of dust. Because planets are formed from these disks, these are referred to as a protoplanetary disks (PPDs).

Observations of both PPDs and exoplanets are improving. However, current instruments are not able to observe planet formation in action. Therefore, models are used to predict the conditions and activities inside PPDs. This is where the availability of the thermo-chemical protoplanetary disk model ProDiMo presents the opportunity to link the observed composition of exoplanets to their formation path. ProDiMo is a 2D steady-state simulation code that solves the radiative and chemical equilibrium self-consistently. Moreover, it generates a great deal of information about the PPD model. The temperature, pressure, density and chemical composition are just a few of the properties that it provides.

Firstly, to benchmark the code, ProDiMo models are compared to a set of simple disk models. The comparison shows that ProDiMo is a very advanced code that is able to predict the PPD environment much better than other models that try to link the formation path to the composition. In addition AA Tau is found to be the most suitable PPD to perform planet formation. Because it has parameters that are found close to median values.

The ProDiMo model is used in combination with a mass accretion scenario. The formation scenario that is applied is called pebble accretion. In this scenario it is proposed that pebbles formed from dust at large radii drift to the inner disk where the pebbles are accreted by a planetesimal. As a result, the planetesimal can grow in mass up to tens of Earth masses (M_{\oplus}), and is now called a core. The moment the core has a high enough mass and the pebble accretion has terminated early in the disk life time, before ~ 3 Myr, it becomes a gas giant. This is done by accreting a massive amount of gas from the disk, and thereby clearing an annulus of gas from the disk. In the case of the AA Tau model, gas giants only form at radii between 2 and 8 AU. The largest gas giant at 4 AU has a mass of $110 M_{\oplus}$.

By combining the model of AA Tau with the pebble accretion scenario, the composition of the resulting gas giants is determined. Planetesimal accretion leads to a stellar C/O of the ices in all of the cores formed between 0.5 and 25 AU. The atmospheres of gas giants formed between 2 and 4.8 AU, with C/O between 1.3 and 13, are up to an order of magnitude away from other similar models and observations. From 4.8 to 8 AU the model predicts a slowly decreasing C/O from 2.2 to 1.3.

Compared to observations the C/O ratios computed for the AA Tau model are similar for planets formed beyond 4.8 AU. On the other hand, below 4.8 AU very large differences are seen. However, to determine why there is a large discrepancy between the computed C/O and the observed C/O, further research is required.

Introduction

The universe seems to be an inexhaustible source of fascinating mysteries and questions. Not the least of which: "Is life in the universe rare, is the universe teeming with life or are we alone?" To answer this question is certainly not a trivial task. For many generations we have been working towards the answer. Each generation with their solution to parts of the puzzle. The latest contribution of the puzzle is the discovery of planets outside of our solar system orbiting other stars in the Milky Way and the determination of their characteristics.

For a long time it has been thought that the 9 and later 8 planets in our Solar system were representative of all planets that could be formed. Since the discovery of larger quantities of exoplanets with "exotic" mass, radius and orbital radius combinations, this notion has been shed. Moreover, these discoveries were not as enlightening as they were surprising. Jupiter sized planets with an orbital radii way interior to the orbit of Mercury, planets as massive as Uranus with the density of a rocky planet are just a few of them. This is the era of expanding our understanding of the variety of planets that exist, and how they are formed.

Planets take in the order of millions of years to form. So there is no chance that we see a planet forming from dust to planets under our eyes or in a human life time. If we want to understand how planets form, ingenious methods have to be invented to investigate the formation process. Astronomers, in particular, the field of planet formation, have taken on this challenging task. It takes many disciplines to address the fundamental questions on the formation of planets; chemistry, magnetism, dynamics, aerodynamics, stellar physics. The models rely on the increasing power and efficiency of computer. Moreover, without engineering to design instruments, precise and accurate measurements of this would not be possible. This thesis aims to contribute a very tiny piece of the puzzle of planet formation. This is done by answering the research questions posed in section 1.1. The remainder of the report will describe how these questions are answered.

1.1. Research questions

Planet formation is a very interesting topic at this time. Only recently protoplanetary disks (PPDs) are observed at spatial resolution to see evidence of planet formation. Moreover, there is an increasing number of exoplanet detections and characterisations. This presents an opportunity to take planet formation theories to a higher level of tests and validations. As mentioned, formation of planets from PPDs is a highly complex field of research. This makes it difficult for a single study to add significant value to the field. Therefore this study only addresses a small part of the planet formation process: the composition of planets formed via pebble accretion. Moreover, the accessibility to a thermo-chemical

model code, ProDiMo(Woitke, 2013; Woitke *et al.*, 2009, 2016; Kamp *et al.*, 2017) presents the opportunity to investigate chemical and environmental conditions of planet formation. From this opportunity a research question is formulated, with sub-questions whose answers contribute to the answer of the main question:

1. How can ProDiMo be used to investigate the formation pathways of hot Jupiters through composition analysis?
 - (a) How must ProDiMo be used to get the most realistic disk model?
 - (b) How can the pebble accretion and planetesimal accretion scenarios be applied to a ProDiMo model?
 - (c) What are the resulting compositions of the gas giants formed?
 - (d) How can the composition of the formed gas giants be linked to the formation process?

Because of the complexity and extensiveness of the problem the questions are very specific. This is done on purpose to be able to answer these questions accurately and completely.

In order to address the research questions, chapter 2 gives a brief description of the background theories of the Protoplanetary disk and how planet formation is viewed. Then in chapter 3 the code that is used and analysed, ProDiMo is described in some detail. Which aspects are considered, which are not considered and how is the model set up. The first sub-question is addressed in chapter 4. Here the ProDiMo model is analysed and compared to other, simpler models. In chapter 5 the pebble accretion scenario is explained in detail and the method to calculate planet core masses is given. To apply this method to ProDiMo the method to find the core masses is adjusted and implemented. In addition a method to find the atmospheric mass once a core has formed is given. Then, finally the composition of several formed gas giants from chapter 5 is determined in chapter 6. A discussion of the results is given in chapter 7. To conclude the report, a reflection of the research questions is presented and recommendations on continuation of planet formation research while making use of ProDiMo is given in chapter 8.

2

Physics and Chemistry: From PPD to planets

The process to form planets involves many aspects. To understand why the structure and characteristics of PPDs are the way they are, first a brief introduction of PPD formation is given. The parameters and processes governing PPDs are also discussed. These aspects are divided over two categories; structure and dynamics in section 2.2 and chemistry and radiative transfer in section 2.3. Section 2.4 briefly goes over some planet formation scenarios. Finally, an explanation of some of the observation processes is given to understand how observations are used to constrain characteristics and the formation of planets, and the limitations are shown in section 2.5.

2.1. Formation of a PPD

The formation of PPDs starts with the formation cloud core inside a molecular cloud (MC). This is a region where the particle density is relatively high. The number density is ranging between $10^2 - 10^6 \text{ cm}^{-3}$, in comparison to the interstellar space diffuse interstellar medium (ISM) of $\sim 0.0065 - 50 \text{ cm}^{-3}$ (Ferrière, 2001). For reference, the atmosphere at sea level has a particle density of $\sim 10^{31} \text{ cm}^{-3}$ (Mohr *et al.*, 2007). Typical masses of MCs vary between $10^2 - 10^6$ solar masses (M_{\odot}) (Montmerle *et al.*, 2006) and have sizes of 30 to 1200 light-years (ly) or 10 to 400 parsecs (pc) (Murray, 2011). An image of an MC is shown in Figure 2.1a¹; the Eagle nebula. Here it is seen how the gas and dust in the cloud is lit up from the inside by massive newly formed stars. These massive stars do not only emit light, but their stellar winds and strong ionising UV radiation also blows the gas and dust in the nebula outward forming a large cavity in the cloud. It is also seen that the cavity is not completely cleared from the cloud material; there are several dark streaks and patches around the centre of the image. These are regions where the cloud is denser than their surroundings, leading to self-shielding of the cloud material so that the radiation can not penetrate the material to ionise and blow the gas and dust away. Under the influence of turbulence, magnetic fields, gravity and radiation from nearby stars, smaller pockets where the density is slightly higher are formed. This stage is depicted in Figure 2.2b and is also visible in Figure 2.1b². This is a zoomed in section of the centre of Figure 2.1a, the tip of the left of the two parallel pillars in the centre of the image. These two pillars remain while the surrounding cloud material has been blasted away. In the zoomed image, the cloud cores are identified, in the small worm-like structures seeming to protrude from larger structure. When these cloud cores collapse, it means a star will start to form. The condition for the collapse of these cores is that a critical mass, the Jean's mass M_J is reached within a spherical region with diameter equal to the Jean's length λ_J and a given temperature (Lissauer and de Pater, 2013). In this way the MCs give birth to great numbers of stars at orders of magnitude of $10^2 - 10^3$. This is why MCs are sometimes called stellar nurseries.

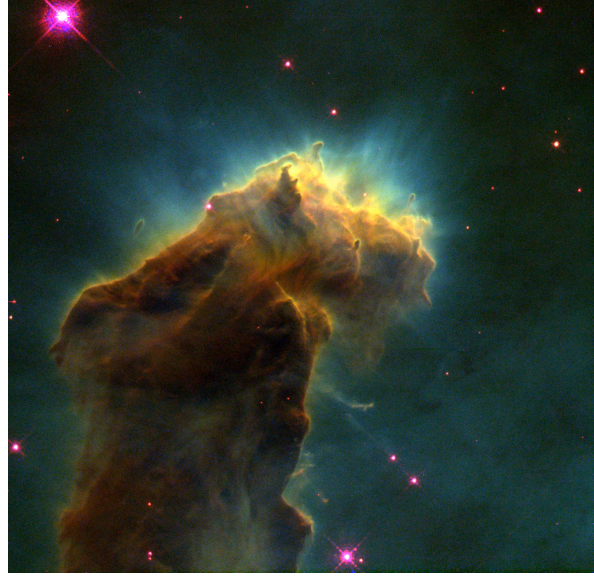
For the study of star formation the start of the collapse means that the clock for star formation starts ticking. From this moment on the elemental composition of the future star and star system is essentially

¹<https://www.eso.org/public/images/eso0926a/>

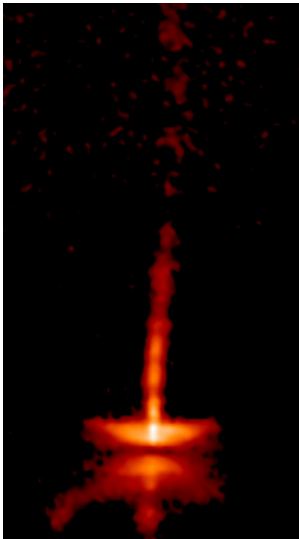
²<https://www.spacetelescope.org/images/opo9544b/>



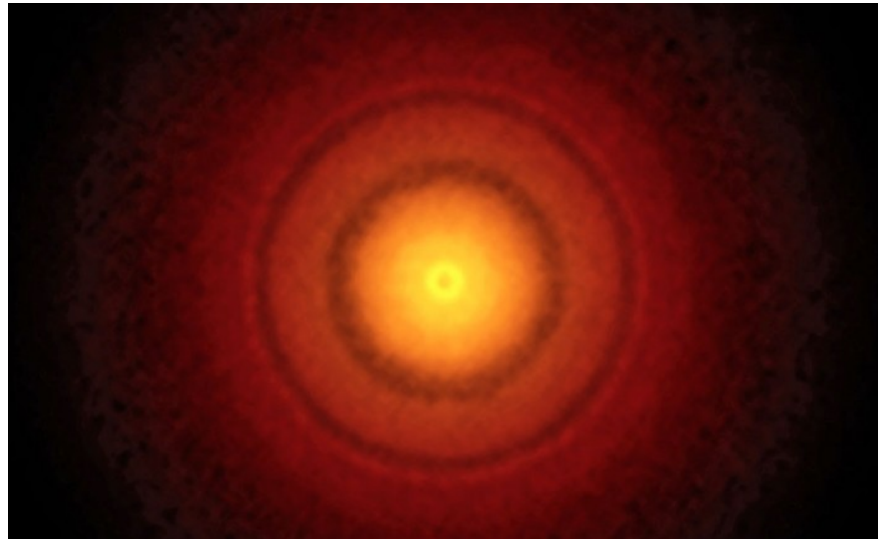
(a) Image by the MPG/ESO 2.2-metre telescope of the Eagle nebula. It is a composite image with 3 filters in the visible range; $\lambda_{eff} = 445, 551, 645$ nm for blue, green and red respectively. Just below the center the famous 'Pillars of creation' are visible. Credit: ESO.



(b) Zoomed section of Figure 2.1a. Tip of one of the "Pillars of creation". Credit: Jeff Hester and Paul Scowen (Arizona State University), and NASA/ESA



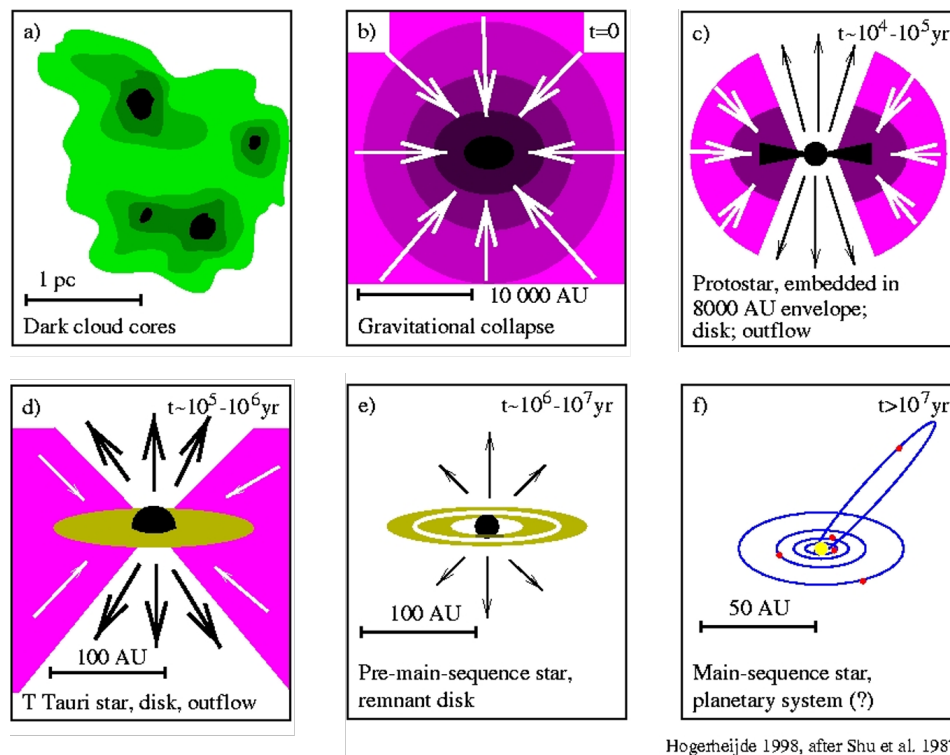
(c) Image of HH-30, a stellar object with bipolar outflows and a disk that is oriented so that the view is nearly edge on. The image is taken by WFPC 2 on the Hubble at a wavelength of 675 nm.



(d) Image of the 870 μm continuum emission from the TW Hydrae disk observed by ALMA. The wide bands are dusty and the darker rings are empty spaces in the disk where planets may be forming and clearing out concentric gaps in the disk. Credit: S. Andrews (Harvard-Smithsonian CfA); B. Saxton (NRAO/AUI/NSF); ALMA (ESO/NAOJ/NRAO).

Figure 2.1: Four images showing different stages in the process of forming a PPD.

fixed. Due to gravitational collapse, all material starts acceleration on a trajectory towards the centre of the cloud. The material coming together in the centre will form a star depending on the mass. If the mass is greater than $0.08 M_{\odot}$ nuclear fusion of hydrogen will fuel the star to become illuminating (Richer *et al.*, 2006; Montmerle *et al.*, 2006). The protostar will start to spin up as the central body accretes more material to conserve the angular momentum.



Hogerheijde 1998, after Shu et al. 1987

Figure 2.2: Sketches of the evolution of a PPD at different stages.

On the other hand, some of the material will go into orbit around the forming star. As depicted in Figure 2.2c, at first this is a spherical envelope surrounding the star because the material orbits the protostar in random planes. But over time the material in the envelope will spin in a single plane in the direction of the net angular momentum, forming a disk due to collapse. This disk acts as reservoir for the protostar as it feeds the protostar to become more massive from its inner rim. So the disk is sometimes also referred to as an accretion disk. Furthermore, accretion of material onto the star comes with a bipolar outflow of a fraction of the accretion mass, from regions near the poles perpendicular to the disk. This results in highly collimated jets ejecting disk material out of the proto-stellar environment. This is caused by the interaction between the stellar magnetic field and the remnant magnetic field believed to be present in the disk (Montmerle *et al.*, 2006; Ferreira *et al.*, 2000; de Gouveia Dal Pino, 1995). In this thesis, magnetic fields are not considered any further.

After $\sim 10^5$ - 10^6 most of the envelope material has collapsed onto the disk as seen in Figure 2.2d. This is also the first time the envelope is optically thin enough to observe the embedded disk. Figure 2.1c³ shows an image of this stage, the bipolar jets are clearly visible and the central star illuminates the upper layers of the disk and the envelope with a shadow of the disk seeming to divide the envelope horizontally.

Figure 2.2e shows the stage of the PPD where the main components are the luminous star and the disk. In Figure 2.1d⁴ one of the best images of PPD is shown. This is an image of the continuum emission, so the dust disk, as observed by ALMA (Atacama Large Millimeter/submillimeter Array). Here the dark circular bands indicate dust density depletion, maybe indicating that planets are forming in this disk (Andrews *et al.*, 2016). From this disk a planet or planetary system forms as shown in Figure 2.2f. As this thesis focuses on planet formation, the disk stage is the most important stage and will be discussed in more detail in the remaining sections of this chapter.

The lack of observations of PPDs that are older than 10 Myr indicates that disks have short lifespans and the planet formation process has to be relatively fast, before the disk is depleted from material

³<https://spacetelescope.org/images/opo0032g/>. Credit: NASA, Alan Watson (Universidad Nacional Autonoma de Mexico), Karl Stapelfeldt (Jet Propulsion Laboratory), John Krist and Chris Burrows (European Space Agency/ Space Telescope Science Institute). [Date accessed: 17-06-2019]

⁴<https://public.nrao.edu/news/2016-alma-twhya/>. [Date accessed: 2-7-2019]

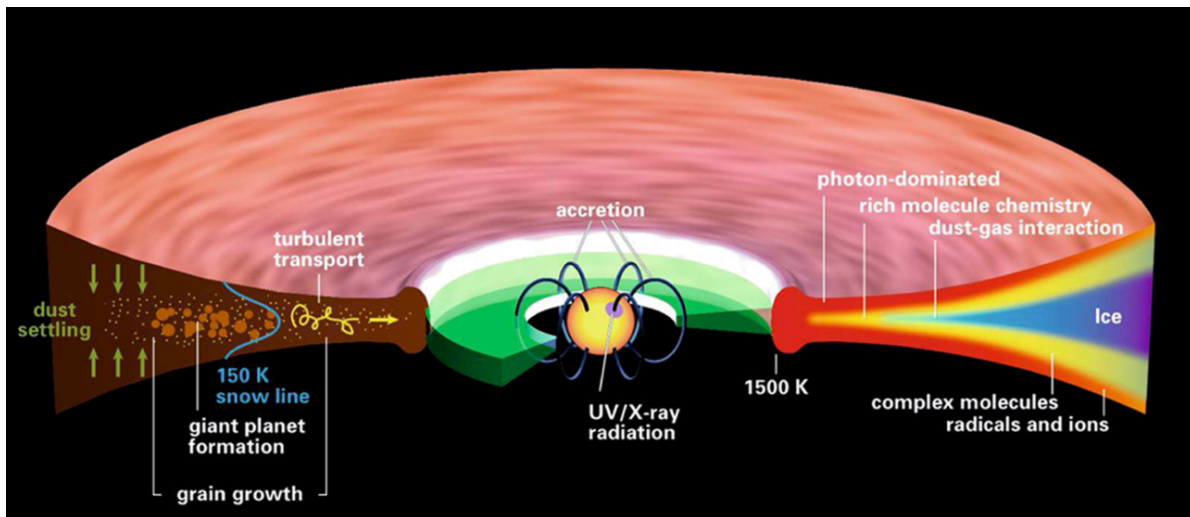


Figure 2.3: Graphic of a protoplanetary disk surrounding a protostar, from Henning and Semenov (2013). The left-hand side shows some aspects of the disk solids structure and dynamics, the right-hand side shows the volatiles temperature structure and chemical conditions. In the centre the protostar is shown with the magnetic field and a accretion region in green.

(Montmerle *et al.*, 2006). This is especially true for gas giants, as they require a large gas disk reservoir to acquire a massive gaseous atmosphere.

2.2. Disk structure and dynamics

The structure and dynamics of the disk are an essential topic in the formation of planets. One way or another the disk material comes together to form planets. With current instruments it is not possible to observe the dynamics of the disk mid-plane where the planets form. So instead of observations on dynamics and structures theoretical models are used to predict the behaviour of a gas disk orbiting a illuminating disk, showing how the dust behaves and how it evolves into larger bodies and finally planet. When the solid bodies reach a certain size, not only the body's dynamics are affected by the disk, but also the other way around; meaning that there is a mutual interaction between the disk and the body.

Figure 2.3 shows a graphic of a PPD. Here the most important aspects in of the PPD are shown. In this section the aspects on the left-hand side of the figure will be addressed. In section 2.3 the right-hand side will be discussed in further detail.

2.2.1. Dust and gas structure

The dust mass is assumed to make up just 1% of the total disk mass, just as in the ISM. At the start it is assumed that the dust and gas are well mixed, so that the dust to gas ratio is uniform for all radii and disk heights. Moreover, at this point the dust particles are small so that their dynamics and temperature are coupled to the gas. Over time, as the dust grows, the dust decouples dynamically from the gas (Weidenschilling, 1977a). This allows the dust particles to redistribute through the disk, settling to the mid-plane and thereby enhancing the dust to gas ratio of the mid-plane. The now higher density of solids increases the collision area and speeds up the dust coagulation which is necessary to form planets before the disk has disappeared. In addition to settling to the mid-plane, the decoupled dust particles also radially drift inward. This is explained in more detail in subsection 2.2.2.

In PPD research, usually the column density distribution in cm^{-2} is used instead of the spatial density distribution cm^{-3} . The column density or surface density is simply the sum or integration of all of the mass that is in a column of disk material perpendicular to the disk. The surface density generally decreases with increasing radius. On the other hand, the disk height increases with radius as shown in Figure 2.3. From observations of the spectrum of PPDs, it is found that there is an excess of IR with respect to the SED for static disk. The only explanation that can fully account for this excess is that the disk is not constant in thickness. Instead the disk height increases with radius, increasing the surface that of the disk that is illuminated by the star. This allows the upper layers of the disk to re-radiate the incoming solar radiation at IR wavelengths, indicating that the disk is flared (Kenyon and Hartmann,

1987).

PPDs are sometimes also called accretion disks. This refers to accretion of the disk material onto the central star. The disk is not attached to the star, there is space between the star and the inner edge of the disk the column density or surface density falls off with increasing radius. This can be different if there are gaps in the disk or the local environment or other dynamical effects where there is a sudden drop or increase. However, unless explicitly stated it is assumed that there are no gaps or material build ups in the disk for the remainder of this report.

2.2.2. Gas and dust dynamics

In a vacuum the velocity of an object with a circular orbit around a central body is given by Equation 2.1.

$$v_K = \sqrt{gr} = \sqrt{\frac{GM_*}{r}} \quad (2.1)$$

Where G is the standard gravitational parameter, M_* is the mass of the central body and r is the radius of a stable circular orbit. g is the gravitational acceleration from the central star. This relation is independent of mass and will be followed by any object in a vacuum without any other perturbation. To the first approximation, Equation 2.1 is still valid for the PPD. The gas of a PPD however, will not follow this motion exactly. There is a deviation from v_K due to the internal pressure of the gas. This due to the negative pressure gradient, the net pressure force acts in the opposite direction from the gravitational force of the central star. This means that the stable orbit is not only governed by the gravitational force but and additional force dictated by the hydrostatic equilibrium Δp given in Equation 2.2. The velocity of the gas is thus given by Equation 2.3.

$$\Delta p = \frac{1}{\rho} \frac{dP}{dr} \quad (2.2)$$

$$v_{gas} = \sqrt{(g + \Delta p)r} = \sqrt{\frac{GM_*}{r} + \frac{r}{\rho} \frac{dP}{dr}} \quad (2.3)$$

Where ρ is the gas density and P is the internal gas pressure. Knowing that the pressure gradient dP/dr is negative, v_{gas} is reduced with respect to v_K . So the gas of the PPD orbits the parent star at a sub-Keplerian velocity.

Weidenschilling (1977b) has shown a study for particles of different sizes behave differently. Small particles are coupled to the gas, so they do not move with respect to the gas. When particles reach size in the order of 1 m, high velocities can be reached with respect to the gas due to the aerodynamic drag. When the particles grow even larger the momentum will be large compared to the aerodynamic drag, making the aerodynamic drag less important and the particle will stay in orbit decoupled from the gas without a significant radial velocity.

2.2.3. Planet migration

As seen in the previous subsection, particles of different sizes behave differently in a gas disk. When the scale of the body embedded in the disk becomes higher, the body also starts to affect the disk itself. Interior and exterior to the body or protoplanet spiral density waves are formed due to gravitational interactions with the disk. This can be seen in Figure 2.4a. The spiral density waves in turn exert a torque on the planet. The outer wave is slightly closer to the planet than the interior wave. This result in a net torque so that the planet is pushed inward and gets an inward radial velocity. This is called type-I migration and concerns bodies with a mass on the order magnitude of an Earth mass, not massive enough to accrete the gas in its orbit and create a gap in the disk.

For larger bodies in a PPD that are massive enough to clear a gap in the disk, torques from the disk material force the planet in the centre of the gap. This means that the planet cannot move with respect to the disk, and the planet is again tied to the disk. This can be seen in Figure 2.4b. So the planet migrates at the rate of the inwards motion of the disk material.

In addition to type-I and type-II migration, turbulence and anomalies of the disk can have any effect on the migration of the planet. After the gas disk had dissipated completely and only solid bodies

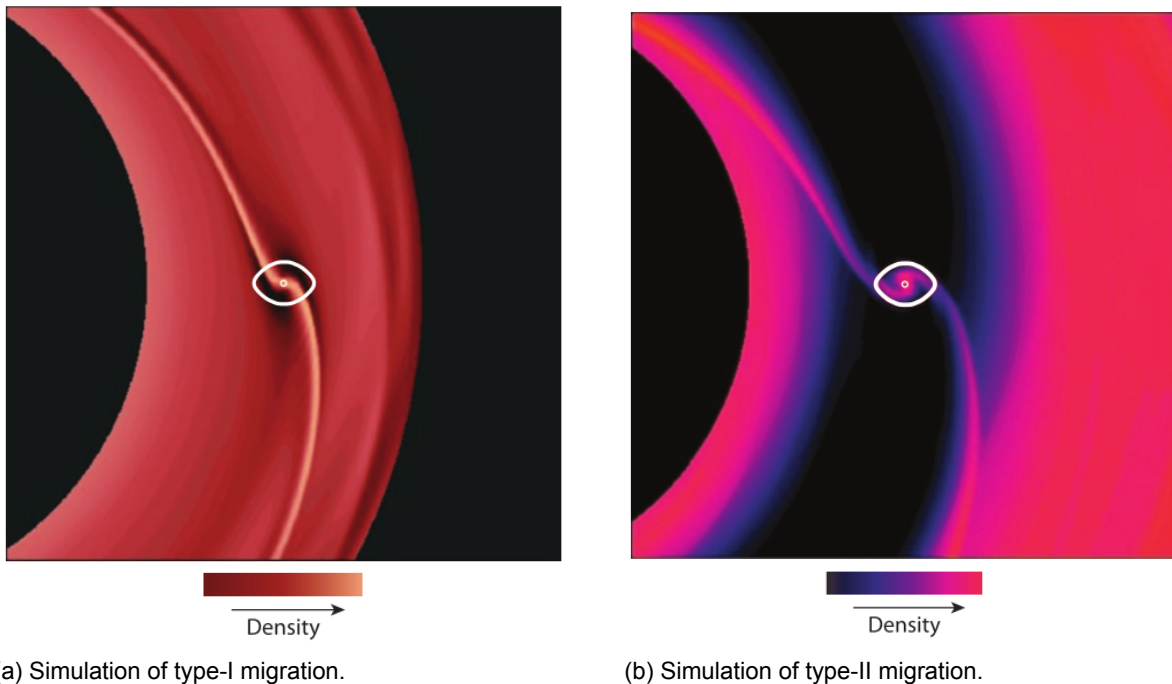


Figure 2.4: Simulations of type-I and type-II migration from Chambers (2009). The figures have the planet in the centre. The black regions on the left-hand-sides of the figures are not empty but left out of the simulation. The same hold s for the right-hand black region of the left figure. Credit:Pawel Artymowicz.

are left, pure n-body dynamics will still play a role in planet migration. So the link between observed exoplanets and the radius of formation is not only dependent on predictable motions in the first 10 Myr after formation of the PPD. But also on unpredictable random motions in the first 10 Myr and the dynamics after disk dissipation. The planetary systems that are observed have had billions of years to dynamically after disk dissipation. Thus the relation between the current planet orbit and the radius of formation is very complex. Another approach to relate planets to their formation location is to look at their chemical composition. This is the aim of this thesis; linking the gas giant location of formation to the observed chemical composition of the atmosphere.

2.3. Radiation and disk chemistry

The local environment in the disk chemistry besides the density, is determined by the radiation field and the composition. In this section first the radiation is introduces, then the gas and dust grain surface chemistry is treated separately.

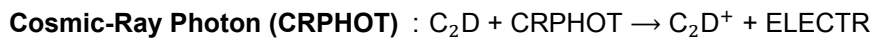
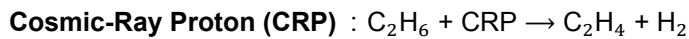
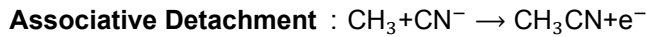
2.3.1. Sources of radiation

The radiation field is required to determine the conditions in the disk for the chemistry and the dust temperature. The radiation has two origins; the irradiation by the central star and the irradiation by external stars that are present nearby. These two sources heat up the disk from the outside so that especially the outer layers are irradiated. Moreover, the particles in the upper layers scatter the incident radiation up to a certain depth, so that the subsurface layers also feel the effect of some of the stellar and interstellar radiation. But from a certain depth the outer layers are self-shielding the deepest layers and the mid-plane which leaves the mid-plane dark and cold as can be seen on the right-hand side of Figure 2.3.

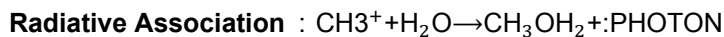
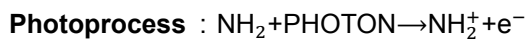
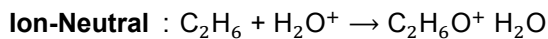
Especially in the outer disk this means that there are more solids to form planetesimals. Moreover, ice-grains that are covered in a layer of ice are stickier, which means that the growth of solid bodies can be faster. This is favourable for planet formation because gas giant need their cores to form early and fast.

2.3.2. Gas chemistry

In this thesis chemistry plays an important role. The conclusions drawn from this research depend greatly on the accuracy of the chemical model. The chemistry inside the disk cannot be observed directly. But, using results from laboratory experiments for astrochemistry, models are designed to simulate the chemistry inside the disk. Chemical reactions can be categorised in several ways. In this case the reactions are categorised in gas-phase reactions and grain-surface reactions. Gas phase reactions are reactions where the reactants and the products are all in gaseous form. A list of the type of gas-phase reactions that are considered in Mcelroy *et al.* (2013) is shown below, with an example reaction:



Dissociative Recombination



2.3.3. Grain surface chemistry

The dust in PPDs is different from what we call dust in everyday life, both in composition and in size. The dust particles consist of a combination of mostly silicate and some carbonaceous material Williams and Cieza (2011). Dust sizes in the ISM and MCs range from $0.005 \mu\text{m}$ to $0.25 \mu\text{m}$ with most dust particles having a size of about $0.1\text{-}1 \mu\text{m}$ Weingartner and Draine (2001); Natta *et al.* (2007). During the evolution from cloud core to the PPD, the dust does not undergo significant changes. During the PPD phase on the other hand the dust particles collide and stick together to form larger grains. The dust grains themselves are not considered to change composition over time. However, in the cooler regions of the disk, especially in the mid-plane, ices will form on the dust grains. This ice formation on the grains is also what improves the sticking efficiency of the dust to each other Wang *et al.* (2005).

Once the ices have formed the chemistry does not stop. On the contrary, there are species that can only form in the observed amounts by chemical reactions that involve ice species. Grain surface reactions involve at least one reactant or product that is condensed onto the surface of a dust grain (Cuppen *et al.*, 2017). The types of reactions that can take place on the surface of dust are shown in Figure 2.5.

Adsorption or accretion is the freeze-out of a gas species onto a dust grain. Ice-formation requires a solid surface to freeze onto, to absorb some of the thermal energy of the species reaction. Desorption is the reverse process from adsorption. This can be thermal desorption, photo-desorption or desorption due to cosmic rays. The reactions can be split up into reactions with reactants both in ice form, the Eley-Rideal mechanism, or one ice species and one gas species reactant the Langmuir-Hinshelwood mechanism. Furthermore, there exists a third type of grain surface reaction, namely the hot-atom mechanisms. This is a combination between the other two surface reaction mechanisms, but not important for the ice-forming regions where the dust and gas have similar temperatures.

Besides reactions, in order for ice-species to meet each other for reactions, there are also mechanisms to relocate species. This can be achieved through diffusion or tunnelling as the bottom two reactions in Figure 2.5.

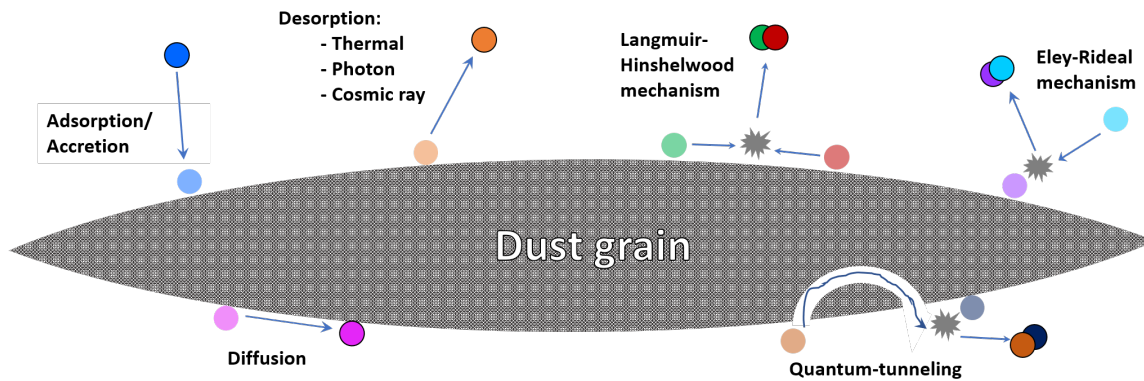


Figure 2.5: Chemical processes that take place on dust grains. In this figure the products of each reaction are singular and in gas phase for clarity of the figure. However, the three reactions on the right hand side can result in multiple products, each of which can be in gas-phase or in the form of ice.

2.4. Giant Planet formation

As the name suggests protoplanetary disks are the birthplaces of planets and provide the material from which they form. When it comes to the process that forms planets, several theories are developed to explain their formation. The two predominant theories are the core accretion scenario and the disk instability (gravitational instability) scenario (Lissauer, 2005). The latter describes a disk in which a gravitational instability results in the collapse of material into a planet, much like the molecular cloud core collapses into a star. This means that the formation can be relatively fast, within ~ 1000 yr (Lissauer, 2005). The core accretion model on the other hand suggests that the orbiting dust in the disk coagulates due to collisions over a few millions of years. Collisions of the dust particles leads to larger dust particles, these particles then collide to form even larger particles. Over time these collisions result in progressively larger particles, pebbles, boulders, and planetesimals. This continues until all the dust has come together in just a small number of large bodies of a few kilometer in diameter. When and if the mass and thereby the gravitational attraction of a body is large enough, the gas will also start to be accreted by the body. This gas accretion continues until the gas is depleted from the direct environment of the body, or the gas is dissipated from the disk entirely. The core accretion model is the formation theory that is explored in this research project. The details of the core accretion mechanisms are explained in further detail below.

Planetesimal accretion

The core accretion model can be divided into two separate approaches to form the planetary core. The most commonly explored model is the planetesimal accretion model (Lissauer, 2005; Montmerle *et al.*, 2006). Until relatively recently, most numerical studies have been focused on formation of planetary cores through pairwise collisions resulting in combined masses of progressively larger bodies (Ida and Lin, 2004; Cridland *et al.*, 2016).

The planetesimal accretion model to form the solid cores has several issues. Once the dust particles grow to between mm and cm sized particles, gas drag causes the particle to rapidly drift inward. This results in migration of dust particles of the inner disk (up to ~ 40 AU) into the protostar within 100 to 1000 yr (Weidenschilling, 1977a). Furthermore, over time, the number of bodies decreases as their masses are combined through collisions. Due to the decreasing number, the probability of collisions occurring also decreases. Of course, over vast periods of time the planetesimals will collide. However, not all collisions lead to a combination of the masses of the bodies. Some collisions result in only a partial combination of the bodies, others end in a total obliteration of both bodies. This means that the time it takes to reach masses required for gas accretion exceeds the gas dissipation time of the disk. This also means that no gas envelope accretion is possible and no gas giants are able to form.

Pebble accretion

Since large numbers of gas giants have been observed, there is a good reason to look for an another mechanism that could overcome these issues. An alternative mechanism is planet formation by pebble

accretion (Lambrechts *et al.*, 2014; Lambrechts and Johansen, 2014, 2012; Ormel, 2017). In chapter 5 this method is described in detail.

Giant atmosphere formation

One way or another the cores will form in the PPD. From research on the gas giants in the solar system, Jupiter and Saturn, it is found that the amount of gas that they contain is ~ 300 and $\sim 75 M_{\oplus}$ respectively. So, to form gas giants or ice giants, these cores need to acquire massive amounts of gas to become gas giants the size of Jupiter and Saturn. Furthermore, the number of gas giants that are being discovered implies that gas giants are common. Since the disk has a limited lifespan due to gas dissipation, this means that there has to be a gas accretion mechanism that is both fast and effective.

It is proposed that once a planet core reaches a certain size before the gas disk is dissipated, the giant atmosphere can accumulate large amounts of gas in a relatively short amount of time

2.5. Observations

Observations are an essential part of planet formation research. Acquiring valuable observations of PPDs and exoplanets is not straightforward. However, by analysis of spatially and spectral resolved data some of the properties can be determined such as the dust temperature, dust disk size, dust sizes, composition of the outer layers of the atmospheres. Other properties must be determined by models of disks that are validated by comparison to the spectra and SED.

2.5.1. PPD observations

From flux densities and spectra of PPDs the composition is probed can be probed. Absorption lines reveal the chemical species that are present in the gas of the disk's outer layers. Even though the dust only accounts for about 1% of the disk mass, it is responsible for most of the opacity (Williams and Cieza, 2011). This makes it practically impossible to probe the denser and colder deeper layers of PPDs with current instruments.

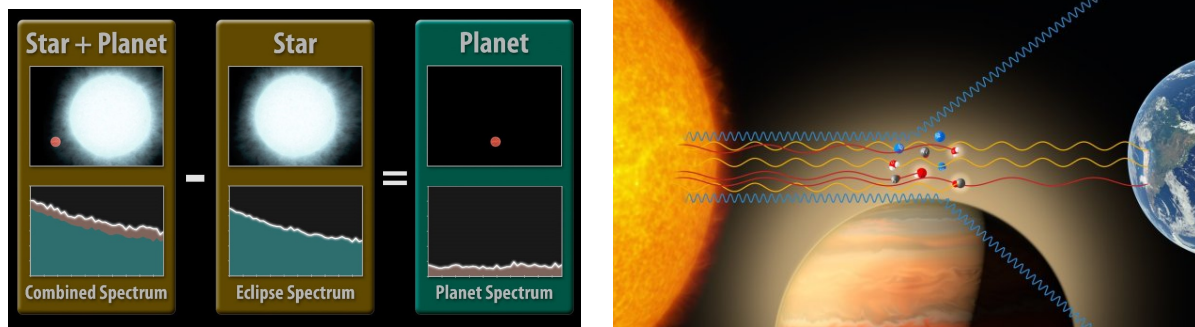
The gas only emits at specific wavelengths depending on its constituents. These emission lines or spectral lines are used to determine the species. From experimental laboratory research it is known which combination of absorption lines correspond to what chemical species. The difficulty is that these spectral lines are very narrow so high spectral resolution is required to distinguish one spectral line from another. Furthermore, there are species with strong spectral line features and others have weak features. So not the complete composition can be determined by these emission spectra.

2.5.2. Observations of gas giants

It has not been long since the first confirmed detection of an exoplanets in 1995 by Mayor and Queloz (1995). Since then, not only thousands of other planets have been discovered, but also some of their orbits and physical properties are characterised. There are several methods to detect exoplanets. One of these methods is to observe the brightness of a star over a period of time. If a planet orbits this star on an orbital plane that is approximately aligned with the line of sight from Earth, it can temporarily obscure part of the starlight. This is called the primary transit of the planet. The brightness of the star will be slightly less during this transit. If the observing instrument can detect this dip in the brightness, a planet can be detected. There are of course other causes of a dip in the brightness of a star, so a single transit is not enough to prove that it is caused by a transiting planet. Confirmation of a potential planet detected using transit method can be confirmed if the dip can be observed periodically. This takes means that the observation period has to be at least 2 full orbital periods which means that only relatively short period planets can be confirmed using this method. However, there are other methods that can be used to confirm the transiting planet, i.e. direct imaging, radial velocity variation of the star (Doppler effect), astrometry or a secondary transit.

The transit of a planet can also be used to characterise its atmosphere. The primary transit occurs when the planet passes the line of sight in front of the star. A secondary transit is defined as the period during which the planet passes behind the star. This means that, assuming that there are no other planets contaminating the observation, the purely stellar transmission is now observed. As shown in Figure 2.6a the difference in transmission between observations during no transit and the secondary transit, describes the transmission from the isolated planet. From this the planetary temperature and the temperature structure can be determined. In addition from the emission spectrum atmospheric

composition can be characterised.⁵



(a) Graphic of the process to obtain the isolated emission spectrum of an exoplanet. The left column describes observations during no transit; the combined spectrum. The middle column is during secondary transit, here called the eclipse spectrum and the right column presents the isolated planet spectrum.

(b) Graphic of the how chemical species in an exoplanetary atmosphere absorb and scatter some of the starlight, while transmitting light of other wavelengths. The transmitted spectrum reaches Earth, where it can be analysed to see which wavelengths have a reduced brightness. This is visible in the form of absorption lines in the spectrum. The and determine what atmospheric composition is responsible for these.

Figure 2.6: Graphics describing how observations of transits can provide information about exoplanets.

Instead of looking at the flux density of a the transit or the emission spectrum, one could look at the spectra of the transit. The atmosphere of a planet is not completely opaque for all wavelengths because, the molecules in the atmosphere each have their own signature set of wavelengths that they absorb and scatter. The wavelengths that are not absorbed or scattered by the atmosphere are transmitted so that instruments can observe it. So by analysing which wavelengths are absent from the spectra, the absorption lines, the chemical species in the atmosphere of the planet can be determined. This is depicted in Figure 2.6b⁶.

⁵<http://www.spitzer.caltech.edu/info/227-Extrasolar-Planets>, created by NASA. [Date accessed: 13-06-2019]

⁶<https://wasp-planets.net/tag/wasp-19b/>. Credit: ESO/M. Kornmesser. [Date accessed: 13-06-2019]

3

Software:ProDiMo

As mentioned before, it is very difficult to see the interior of PPDs. With the sensitivity of current instruments, only a thin outer <https://www.overleaf.com/project/5b9125618fb20252a56422e0> layer of the PPD can be probed. This means that the properties of the interior have to be inferred from the information that is comes from the outer layers of the PPD. As mentioned in chapter 2 many aspects affect the physical and chemical properties of the interior. In order to understand what is going on inside PPDs are modelled with various types of simulations.

In order to make a comprehensible model of a PPD, it is necessary to make simplifications. In fact the first PPD models were the modelled as simple disk in hydrostatic equilibrium, radiating as a black body (Chiang and Goldreich, 1997). From the understanding of these early studies, more detailed models have been developed to understand the properties and processes in PPDs. Each generation if PPD models provides a little better insights of PPDs. Therefore more and more aspects are coded to create more detailed models.

Hydrodynamics codes are used to model the behaviour of the disk as a fluid. N-body simulation codes are used to model the dynamics between bodies, i.e. planets, planetesimals, asteroids, and the central star as a result of their gravity. Chemical codes simulate the chemistry of the gas and sometimes dust in the PPD. In this thesis the focus lies in on chemical disk codes, in particular ProDiMo (PROtoplanetary Disk MOdel).

ProDiMo recently celebrated its 10th anniversary. In 2009 the first version of ProDiMo was presented by Woitke *et al.* (2009). The code can be downloaded after applying and getting accepted for a user account at via <http://forge.roe.ac.uk/trac/ROEforge/wiki/NewUserForm>.

ProDiMo is a versatile disk simulation code written in FORTRAN with many options to customise the PPD as desired. However, for this thesis not all functions are relevant. Therefore the descriptions given in this thesis report are limited to a standard or typical T Tauri disk PPD and additions that are used.

3.1. Global structure of ProDiMo

ProDiMo is a radiation thermo-chemical disk modelling code. This means that for a given disk structure the radiation field, thermal balance for the gas and dust and the chemical abundances are solved. Because these aspects are coupled to each other, it is not sufficient to solve these aspects separately. An iterative scheme is applied to achieve a self-consistent disk model. The idea behind ProDiMo is to simulate PPDs with a self-consistent radiation thermo-chemical code. This is achieved by iterative process as shown in Figure 3.1.

3.1.1. Structure

The first step of ProDiMo is to determine the disk structure given the input parameters. By this it is meant that the physical distribution of material is determined. This is done for a set of grid points that are distributed overe the disk radius and heighth.

ProDiMo allows you to provide a disk structure, but also gives you the option to use a built in parameterized disk structure. ProDiMo works with a 2-dimensional structure (2D) which implies that

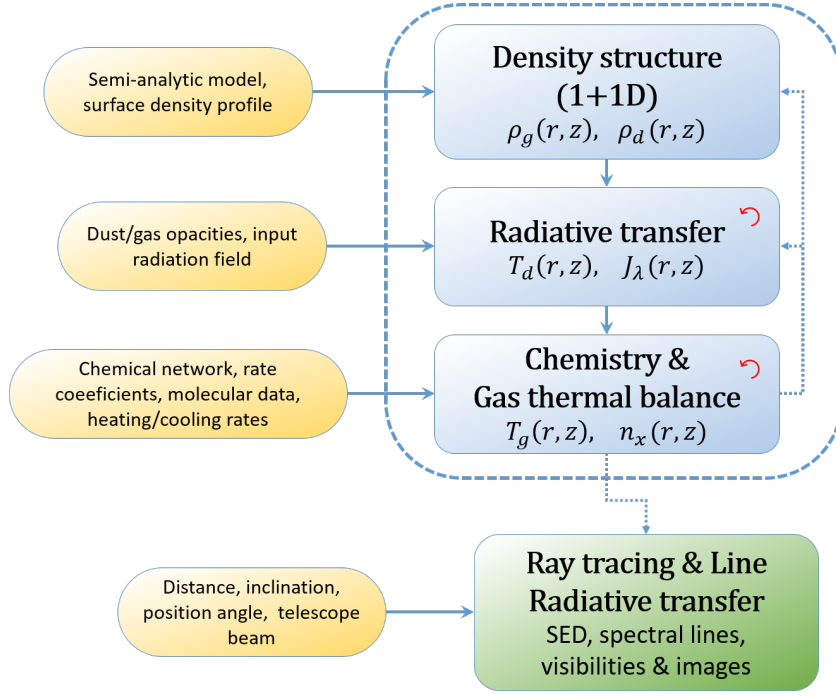


Figure 3.1: Flow diagram of the global code structure of ProDiMo, adjusted from Rab (2018). The solid blue arrows indicate the sequence that is used in case of opted for no iterations. The dotted blue arrows are optional module paths and the red arrows mean that iterations are used inside of the module to make it self-consistent. The left-hand yellow boxes are a selection of the input data for the modules in the blue boxes. The bottom green box is an optional module.

the disk is assumed to be azimuthally symmetric. The spatial properties in the disk are computed from the disk inner radius R_{in} to the outer edge of the disk R_{out} and from the mid plane at $z=0$ cm upward. The disk lower half of the disk is assumed to be symmetric with the upper half.

The reason that the density structure is considered 1+1D as shown in Figure 3.1, is that the radial and vertical mass distributions are treated separately. First the radial distribution is determined using a power-law, with adjustments to taper the outer edge and smooth out the inner rim for a physically realistic termination of the disk.

$$\Sigma(r) = \Sigma_0 \left(\frac{r}{R_{in}} \right)^{-\epsilon} \exp \left(\frac{r}{R_{tap}} \right)^{2-\epsilon} \quad [\text{g/cm}] \quad (3.1)$$

$$M_{disk} = \int_{R_{out}}^{R_{in}} \Sigma(r) r dr \quad [\text{g}] \quad (3.2)$$

Where R_{tap} is the radius from which the disk starts to taper, ϵ is the surface density power index, and Σ_0 is the scaling factor that is determined by the disk mass using Equation 3.2. When the radial distribution of mass, so the column or surface density Σ , is known the vertical structure is solved, either hydrostatically or parametrically.

The grain sizes are not solved by ProDiMo. Instead the minimum and maximum dust sizes, $[a_{min}, a_{max}]$ are required as an input with a power index a_{pow} to compute the dust size distribution of the particle radius a . Initially this distribution is attributed to the whole disk. If desired, the effect of dust settling of larger dust grains to the mid-plane can be taken into account in the code. However, the radial dust distribution remains fixed. Dust settling only redistributes the dust grain sizes vertically. (Woitke *et al.*, 2016). Besides the dust size distribution the composition of the dust has to be predefined in the input file. However, effects of composition of the dust are not considered.

3.1.2. Radiation field

In ProDiMo two sources of irradiation are considered; stellar radiation from the central star and inter-stellar radiation from other stars near the location of formation. The stellar radiation is simulated by a

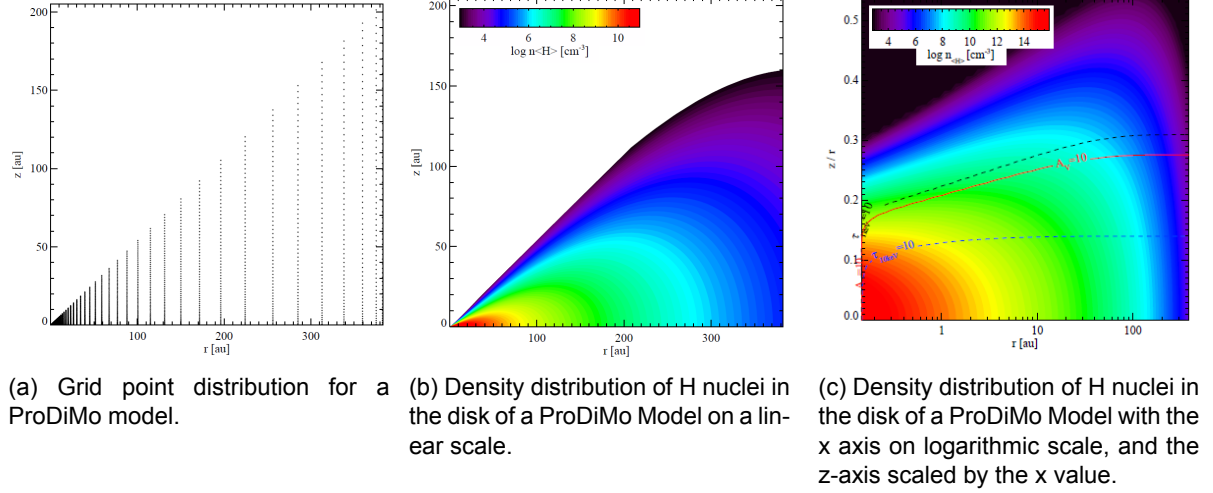


Figure 3.2: Grid point distribution and density distribution of the disk.

stellar atmosphere model called PHOENIX. PHOENIX models the photo-sphere of a star only. However, young stars that also accrete material from the disk have an excess UV and X-ray emission. This can also be included in the radiation model of ProDiMo. In addition to these sources, scattering of radiation and thermal emission is also taken into account. Here, the radiation field is not explained in more detail because the effects of the radiation is not in the scope of the thesis. A more detailed description of the radiative transfer is available in Woitke *et al.* (2009). It suffices to understand that radiation is taken into account to relatively high level, and that the outer mid-plane is shielded from radiation so that ices are readily formed.

3.1.3. Chemistry

Once the disk density structure, dust temperature T_d and radiation field are determined, the chemistry module is initiated. ProDiMo allows to use a custom list of elements and species that are to be considered. The standard T Tauri disk has 12 elements: H, He, C, N, O, Ne, Na, Mg, Si, S, Ar, Fe. They are present in a range of 242 different chemical species in the form of atoms, molecules, ions, double ions and ices. The Ne and He abundances are adopted from Lodders (2003), the remaining elemental abundances are taken from Savage and Sembach (1996) with Na, Mg, Si, S and Fe reduced by a factor 100 following Graedel *et al.* (1982). The initial distribution of elements is assumed to be in the most ionised species for each elements, i.e. H^+ , He^+ , C^{++} , N^{++} , O^+ , Ne^{++} , Na^+ , Mg^{++} , Si^+ , S^+ , Ar^+ , Fe^{++} . The abundances of each species are taken from a number of sources. By chemical reactions over time the elements are redistributed over all species. The species that are considered in this project are listed in Appendix A in `Species.in`.

The abundance of each species is dependent on the net formation rate $\frac{dn_i}{dt}$. For a chemical species i the rate is given by Equation 3.3.

$$\frac{dn_i}{dt} = \sum_{j \in F_j} k_j(T_g) n_l n_m + \sum_{j \in F_j^{phot}} k_j^{phot} n_l + \dots \quad (3.3)$$

$$- \sum_{j \in D_j} k_j(T_g) n_i n_m - \sum_{j \in D_j^{phot}} k_j^{phot} n_i + \dots \quad (3.4)$$

F_j and D_j are the complete sets of 2-body reactions that respectively form and destroy species i . Where k_j^{phot} is the rate of photo-reactions such as photo-ionisation and photo-dissociation. Photo-ionisation occurs when a photon encounter an atom or molecule with an energy high enough to kick an electron out of the species. Photo-dissociation is the separation of a molecule into two molecules or atoms. Again this occurs when the molecule encounters a photon with an electron of sufficient energy. Beside the

$k_j(T_g)$ is the 2-body reaction rate which is dependent on the gas temperature T_g according to Arrhenius equation shown in Equation 3.5.

$$k_j(T_g) = A \exp \frac{-E_a}{k_B T_g} \quad (3.5)$$

Besides these two terms for formation and destruction by thermal gas phase reactions and photo-reactions there are also other types of reactions that change the composition. The types of reactions that are taken into account are; photo reactions, neutral-neutral reactions, ion-neutral reactions, charge-exchange reactions, cosmic ray and cosmic ray particle induced photo reactions and three-body reactions. Most of the reactions are taken from the University of Manchester Institute of Science and Technology (UMIST) database for Astrochemistry (UDfA) ⁷. This database that is used is the most recent version from 2012 called "RATE12", and consists of 6173 gas-phase reactions with their rate coefficients (Mcelroy *et al.*, 2013).

In addition to the UMIST gas-phase only database there is also the option to add reactions if desired. Only reactions with two reactants are considered. The number of products per reactions varies between one and four. In ProDiMo gas-phase species and their icy counterparts are considered separate species. So the standard ProDiMo disk model makes use of the option to add reactions that convert gaseous species into ice species by thermal adsorption and ice species back into gas via thermal, cosmic ray induced and photo-desorption.

3.1.4. Gas thermal balance

As can be seen in Equation 3.5 the rate of chemical reactions is dependent on the gas temperature. In many studies, the gas temperature is simply assumed to be equal to the dust temperature. For the mid-plane where the disk is dense, this assumption is a good approximation. However, for the upper layers of the disk where the density is low, the gas temperature can deviate significantly from the dust temperature. So ProDiMo also computes the gas temperature for each grid point. The gas temperature is calculated so that there is a thermal balance as shown in Equation 3.6.

$$0 = \sum_k \Gamma_k(T_g, n_{sp}) - \sum_h \Lambda_h(T_g, n_{sp}) \quad (3.6)$$

Where Γ_k and Λ_h are the heat gain and heat loss rates for the k heating and h cooling processes. These rates have the units of $\text{erg s}^{-1} \text{cm}^{-1}$. Can be seen in the equation, the heating and cooling rates are dependent on the gas temperature T_g and the species densities n_{sp} . This means that the gas composition and temperature are interdependent. In order to solve this ProDiMo uses an iterative scheme to determine both the composition and the gas temperature consistently.

3.2. Grain surface chemistry

The original ProDiMo only includes chemical reactions in the gas phase. This means that gas-gas reaction and conversion from gas species into ice species on dust grains and vice-versa are included. It also means that reactions between ice-ice and gas-ice reactions are neglected. This simplification can have a significant impact on the results. Certain chemical and especially complex chemical species are not formed or not efficiently enough without a grain surface to absorb the energy released by the chemical reaction. Therefore, for this thesis a formerly developed grain surface chemistry module is switched on. One of the chemical species, that is significantly affected by the addition of surface chemistry to the disk model, is water. As can be seen, especially in the outer disk the abundance of water has increased multiple orders of magnitude.

3.3. Time dependent disk model

The standard disk model in ProDiMo is the solution to a steady state disk, so a time independent model. The disk size, incoming radiation sources, gas and dust densities, dust sizes and dust size distributions are fixed. The chemistry is set to continue evolving regardless of the time period it takes to get there. The modules are iterated until thermo-chemical equilibrium is reached.

⁷<http://udfa.ajmarkwick.net/index.php?mode=downloads>

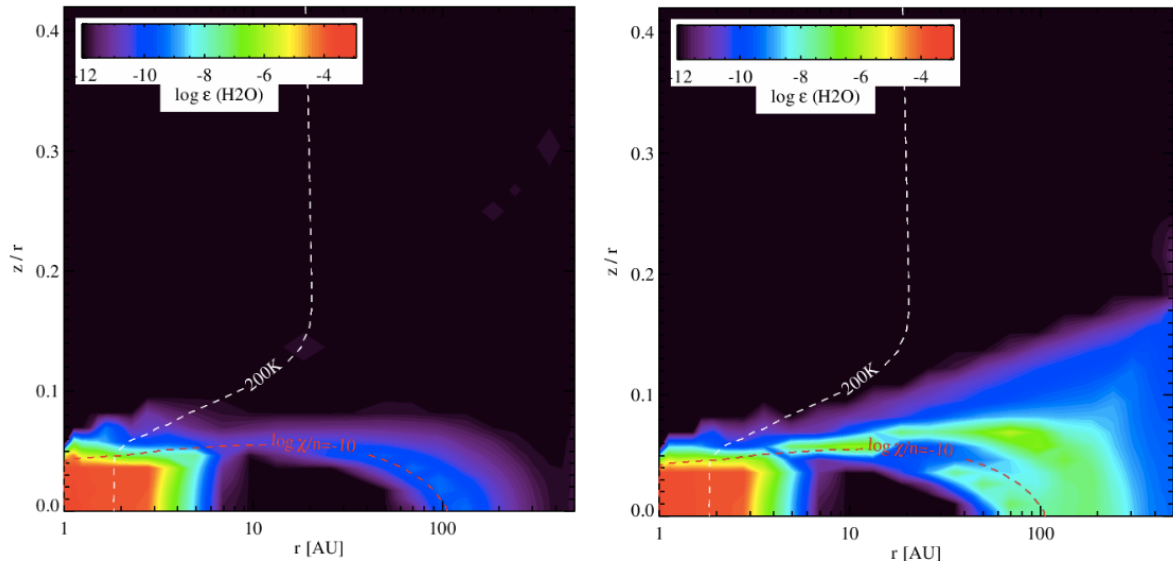
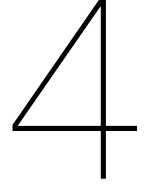


Figure 3.3: Comparison of H_2O (gas) abundances of a disk without (left) and with (right) surface chemistry using ProDiMo disk models. Credits: W.-F. Thi.

A switch in ProDiMo gives the user option to calculate the disk chemistry at specified time disk times. The time dependent disk model in ProDiMo is very similar to the time independent model. The only thing that is different is that the chemistry and thermal balance are not iterated until conversion to thermal equilibrium, but rather considers the time-steps that are called for.

It is important to keep in mind that the disk is not fully time dependent, only the composition and temperature evolves over time. This must be kept in mind when interpreting the results of a PPD model produced by a ProDiMo time-dependent disk model.

For the purpose of planet formation research the time-dependent disk is important. Giant planet formation is predicted to be relatively fast (Montmerle *et al.*, 2006). If there are large variations in composing of the disk over time, the timing of planet formation can have a significant impact on the composition of the planets. Especially the atmospheres of gas giants which accrete the bulk of their atmospheric mass in ~ 1 Myr. (Woitke *et al.*, 2016)



A typical ProDiMo Model

In order to do a research with ProDiMo it is important to be aware of how ProDiMo compares to a simple solution derived from observations. This will allow to check the effects of the simplifications and will help to validate ProDiMo for the purpose of predicting the PPD conditions. To do this, the temperature profiles of the mid-plane of ProDiMo and the simple solution, that was developed by Lewis (1974) and used since then, are compared. In this chapter the aim is to compare the simple solution described above to the results of the extensive model ProDiMo.

In the first section the density and temperature from observational data in several disks will be discussed, as well as the different temperature and density profiles. In the second section different disks temperature and density obtained with ProDiMo will be compared to simple temperature profiles derived from observations.

4.1. Simple temperature and surface density fits

A simple relation for the estimate of the temperature profile of a disk can be fully described by Equation 4.1. This equation is derived by Lewis (1974) by analysing the composition of bodies like moons and planets in the solar system. From the composition it is determined what the temperature was during formation and thus in the PPD of the solar system, sometimes referred to as proto-solar disk or solar nebula.

$$T_r = T_1 \left(\frac{r}{1\text{AU}} \right)^{-q} \quad (4.1)$$

Where T_1 is the reference temperature of the mid-plane at the reference radius, usually at 1 AU, and q the power-law index which characterises the steepness of the temperature profile.

For the flat disk model, as opposed to a flared disk model, this parametrized temperature profile of the mid-plane temperature is accompanied by a similar parametrized surface density profile as shown in Equation 4.2 Shu *et al.* (1987):

$$\Sigma_r = \Sigma_5 \left(\frac{r}{5\text{AU}} \right)^{-p} \quad (4.2)$$

Where Σ_5 is the reference surface density at the reference radius at 5 AU, and p the power-law index. In PPD models these equations are widely used to model the PPD, see for example Eistrup *et al.* (2016); Andrews and Williams (2007); Cridland *et al.* (2019); Öberg *et al.* (2011); Madhusudhan *et al.* (2016a). Furthermore, for a flat disk model, the opacity spectrum κ_ν is assumed to follow Equation 4.3.

$$\kappa_\nu = \kappa_0 \left(\frac{\nu}{\nu_0} \right)^{-\beta} \quad (4.3)$$

Where κ_0 is the reference opacity and ν_0 is the reference frequency. In this section this method to model the temperature and density is compared to disk models simulated by ProDiMo.

Andrews and Williams (2007) conducted a study with a sample of 24 observed PPDs. The observations consist of spatially distributed submillimeter continuum emissions from a single wavelength (from the submillimeter array (SMA) on Mauna Kea, Hawaii) and continuum flux densities are used to find

characteristic parameters of a sample of 24 PPDs. The continuum flux densities are acquired from a number of sources mentioned in Andrews and Williams (2007). The parameters T_1 , q , Σ_5 , p and the outer disk radius r_{out} are fitted to the spectral energy distribution (SED) of a flat disk and the spatial distribution of continuum emission at a single wavelength, an image, simultaneously. The aperture synthesis images of the spatially distributed continuum emissions are shown in Figure 4.1.

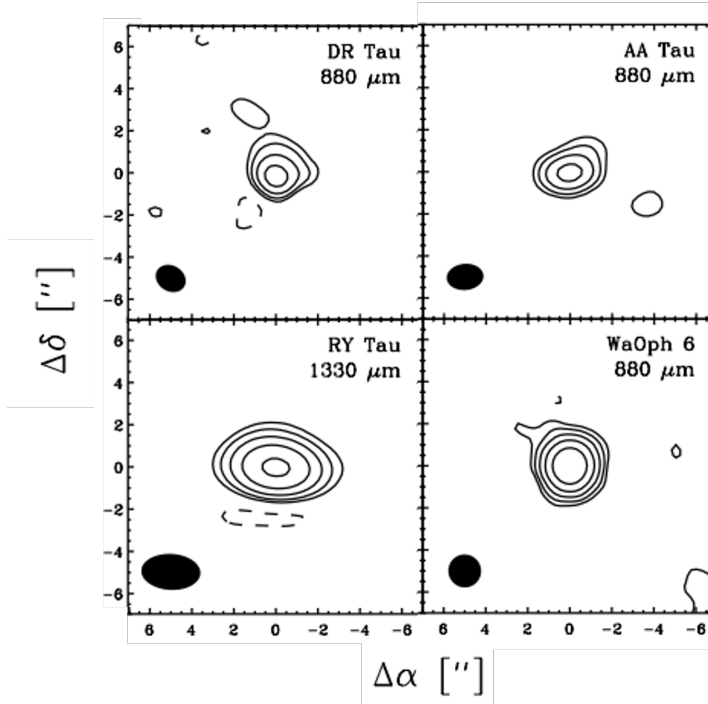


Figure 4.1: Aperture synthesis images of submillimeter continuum emission for the AA Tau, DR Tau, RY Tau and WaOph 6 disks. The contours indicate the intensity, beginning at 3σ and each following contour has a step of 2σ . The ellipse in the left lower corner of each image represent the Full width at half maximum (FWHM) dimensions and orientations of the naturally weighted synthesised beams. Combined figure from Andrews and Williams (2007).

Andrews and Williams (2007) fits the SED observations to the flux density profile of the flat disk model. For the flat disk case the flux density F_ν at frequency ν is given by Equation 4.4.

$$F_\nu = \frac{\cos i}{d^2} \int_{r_{in}}^{r_{out}} B_\nu(T_r) \left(1 - e^{-\frac{\tau_{\nu,r}}{\cos i}}\right) 2\pi dr \quad (4.4)$$

Where r_{in} and r_{out} the inner and outer radius of the disk. The SED of the disk can be fitted if a few parameters of the disk are estimated beforehand. The inclination i , position angle P.A. and r_{in} are taken from the earlier mentioned sources or a Gaussian fit with the continuum emission if they were not found in literature. The opacity spectrum κ_ν is assumed to follow Equation 4.3. Here the reference opacity is assumed to be $\kappa_0 = 0.1 \text{ cm}^2 \text{ g}^{-1}$ at 1000 GHz, this implies a gas to dust mass ratio of 100:1. The power law index of the opacity is assumed to be $\beta = 1$. The optical depth $\tau_{\nu,r} = \kappa_\nu \Sigma_r$ and $B_\nu(T_r)$ is the Planck function at a given radial temperature and d the distance to the observer.

In order to compare ProDiMo to the simple temperature profile as given in Equation 4.1, the input parameters must resemble the same input conditions as for the simple solution as much as possible. From the sample of 24 disks, 4 are chosen to compare to ProDiMo: AA Tau, DR Tau, RY Tau and WaOph6. These are selected from Andrews and Williams (2007), based on their fitted parameters, so that a large variety of disk characteristics is represented. In this way it can be investigated whether

the comparison between ProDiMo and the simple models is different for different types of disks. Moreover, AA Tau has parameters that are close to the median values of the complete sample of 24 disks. Estimated parameters of the 4 chosen disks are presented in the upper 5 rows of Table 4.1.

To model the same PPDs with ProDiMo, many more parameters have to be provided. The mid-plane temperature and surface density profiles found by are compared to the results by ProDiMo. Some of the parameters are given by Andrews and Williams (2007), while other parameters on the disks properties and the central stars characteristics are found in other studies (Bouvier *et al.*, 1999; Muzerolle *et al.*, 2003; O'sullivan *et al.*, 2005; Greaves, 2004; Güdel *et al.*, 2007; Andrews *et al.*, 2016). All of the used parameter are provided in Table 4.1. Some papers have conflicting parameters, in those cases it is indicated in the table how this is handled. Furthermore, for some cases the standard ProDiMo values are used.

Table 4.1: Input parameters for the simulations of the AA Tau, DR Tau, RY Tau and WaOph 6 disks that have differences between disks. The gray boxes indicate that no value was found for and that the standard T Tauri value of pre-programmed in ProDiMo was assumed.

Object name	Std. TTauri	AA Tau	DR Tau	RY Tau	WaOph 6
T_1 [K]	-	195^{+7}_{-15}	315 ± 5	985^{+70}_{-68}	173 ± 5
q	-	$0.59^{+0.07}_{-0.05}$	0.61 ± 0.02	0.70 ± 0.04	0.65 ± 0.03
Σ_5 [g/cm ²]	-	16	11	12	69
p	-	0.9	0.5	0.5	0.7
R_{out} [AU]	600	400	100	150	275
M_* [M_\odot]	0.7	0.76^c	1.11^e	2.37^c	0.9^f
T_{eff} [K]	4000	4060^c	4000^*	5080^c	4205^f
L_* [L_\odot]	1	$0.8^{a,c}$	0.96^e	7.6^c	2.9^f
L_X [erg/s]	$1 \cdot 10^{30}$	$1.04 \cdot 10^{30}{}^c$	$1 \cdot 10^{30}{}^*$	$5.24 \cdot 10^{30}{}^c$	$1 \cdot 10^{30}{}^*$
dust/gas mass ratio	0.01	0.01^*	0.16^c	0.01^*	0.01^*
M_{disk} [M_\odot]	0.01	0.02^b	0.002^c	0.02	0.077^f
R_{in} [AU]	0.07	$0.07^{(b+g)/2}$	$0.15^{g,d}$	0.54^g	0.12^f
R_{tap} [AU]	100	100^*	30^h	40^h	100^*

^a Bouvier *et al.* (1999)

^b O'sullivan *et al.* (2005)

^c Güdel *et al.* (2007)

^d Muzerolle *et al.* (2003)

^e Greaves (2004)

^f Andrews *et al.* (2009)

^g Andrews and Williams (2007)

^h Estimate

* ProDiMo standard TTauri value

Small dust grains are an effective way to shield the mid-plane of the disk from stellar and interstellar radiation. This leads to a very cold environment on the mid-plane of the disk. The same amount of dust coagulated into fewer larger grains on the other hand allow the radiation to penetrate deeper into the disk. Which leads to higher mid-plane temperatures. So the dust size distribution is an important factor in determining the mid-plane temperature. The size distribution is not a factor in Andrews and Williams (2007) so unknown. So a number of dust size distribution is used to make multiple disk model of each PPD and analyse how well they agree with the flat disk model.

In Table 4.2 the minimum and maximum dust sizes, a_{min} and a_{max} respectively, for 3 cases are shown. In case 2 the default settings by ProDiMo are used. After evaluation of this case, the grain sizes are varied in order to try to approach to the flat disk solution based on observations resulting in case 1 and case 3.

Mid-plane temperature

The comparisons of the temperature for the different disks and the ProDiMo results are shown in Figure 4.2. Firstly, when looking at the results for case 2 it is noticed that the shape of the ProDiMo results roughly resemble the simple case. However on the extremities of the curves, so the far inner region

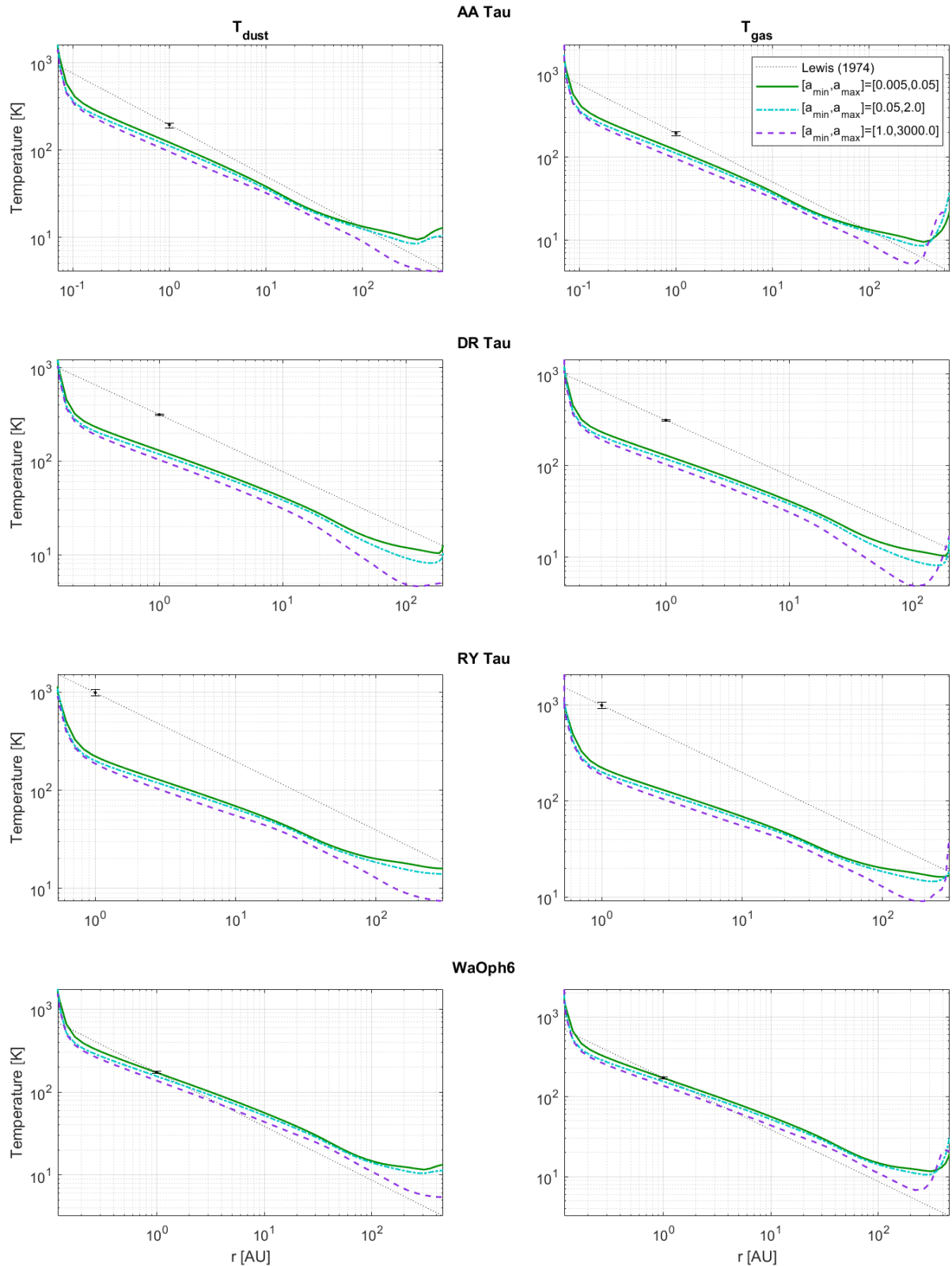


Figure 4.2: Mid-plane temperature profiles for the dust(left) and the gas(right) as computed by ProDiMo as the solid green, dash-dotted blue and dashed purple lines for case 1, 2 and 3 respectively, for 4 different disks. The reference temperature profiles from the Lewis (1974) simple solutions are indicated by the dotted black lines. In addition the error bars of the mid-plane temperatures at 1 AU are shown.

Table 4.2: Dust sizes for the different cases.

	a_{min} [mic]	a_{max} [mic]
Case 1	0.005	0.05
Case 2	0.05	2.0
Case 3	1.0	3000

and far outer region of the disks, the temperature profiles start to deviate from the exponential curve. This is most prominent in outer regions of the disks for the gas temperature profiles.

As expected in the mid-plane, the dust and gas temperatures are almost identical up very high radii. The difference between the gas and dust temperature of the outer region can be explained by the low density, which results in a decoupling of the gas and dust temperatures.

By looking at the results for case 2 it is seen that the temperature produced by ProDiMo is generally much lower than the simple model. Particularly at 1 AU it is desired to have comparable temperatures, because this is the region to which the data is fitted. At 1 AU the temperature differs by about a factor of 2, 3 and 5 for the AA Tau, DR Tau and RY Tau disks respectively. The only PPD where the simple model and ProDiMo are similar is the coldest disk WaOph 6 on the bottom panel. The significant differences between the simple solution and case 2 is attributed to the environmental conditions in ProDiMo like the level of dust coagulation. In order to address how the coagulation of dust changes the temperature profile of the disk, the maximum size of dust particles is changed in case 1. It is expected that this will decrease the temperature, due to the more effective shielding of the dust particles. The resulting temperature profile from the grain size distribution with a range of smaller dust particle sizes are shown in green. This curve shows an increase in temperature as opposed to the expectation. A third set of disk models, case 3, is shown as the purple dashed curve in Figure 4.2. Here the dust sizes are increased so higher temperatures are expected. Again, the opposite is seen, the temperature decreases.

This unexpected behaviour can be attributed to the fact that the PPD is a complex system. By changing the dust grain sizes the disk changes significantly due to dust settling. Larger dust grains means that more of the dust mass will settle down to the mid-plane. This leads to deeper penetration of the stellar and interstellar radiation into the disk. Moreover, larger dust grains also decrease the surface area on which ice species can form. These are just a few of the aspects that are changed when the dust grain sizes are adjusted. So it is not a straightforward relationship.

This example shows how the effects of changing a single parameter on other parameters are not easily predictable. The exact reason for this unexpected result could be investigated. However, the focus of this project lies elsewhere. The message to take away from this is that the PPD is a complex system.

The fact remains that, for all four PPDs, a slight overall improvement can be achieved. However, the difference in temperatures are still not within the error bars, and are difficult to obtain. There are 2 possible explanations for this; (1) the input parameters and or switches in ProDiMo do not correspond to the real conditions that produce the observations that the simple solution is fitted to; (2) or the temperatures are over estimated by Andrews and Williams (2007). The latter explanation is discussed extensively in Andrews and Williams (2007), where it states that the estimated parameters are sensitive to all of the observations.

In the same way the temperature profiles of AA Tau, DR Tau, RY Tau and WaOph 6 are compared, the surface density profiles are compared in Figure 4.3. The surface density profiles computed by ProDiMo in all three cases are identical. This is because $\Sigma(r)$ is independent on the level of coagulation. Moreover, for 2 of the 4 disks, AA Tau and DR Tau, the surface density at 5 AU are within the error bars of the data derived from observations. Since the combination of surface density and temperature profile equations in Equation 4.2 and 4.1 respectively are fitted simultaneously, they are expected to be consistent with each other. However, the fact that the surface density can be achieved with a self consistent model, ProDiMo, but not the temperature suggests that the flat disk model is not consistent.

4.2. Disk compositions

The composition of the gas in PPDs is difficult to observe in detail, due to limited spectral ranges and resolutions. There are however a few species that have emission lines that can be detected relatively easily with current instruments, namely H_2O , CO_2 and CO . Therefore, the abundance and

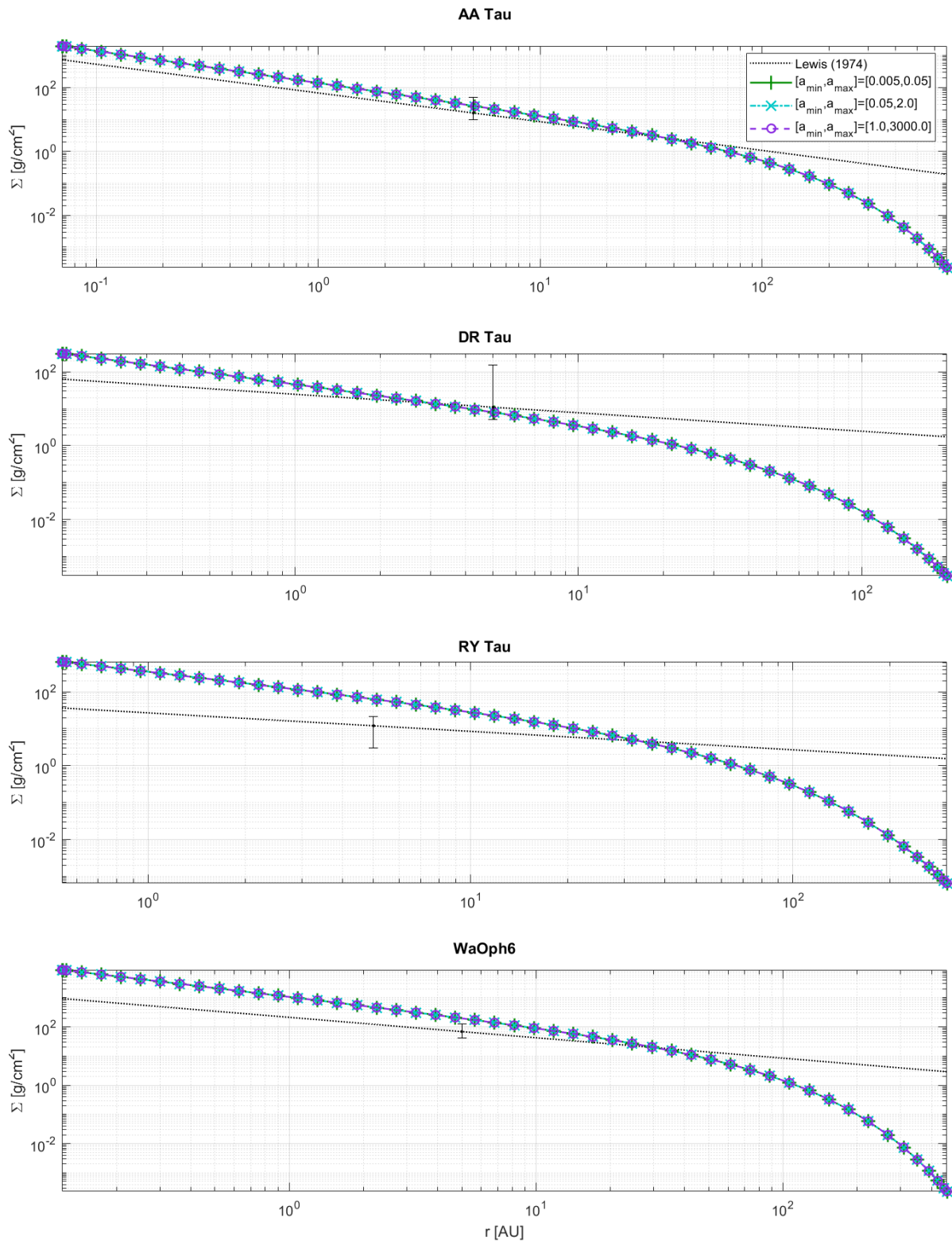


Figure 4.3: Surface density profiles as computed by ProDiMo as the solid red, green, yellow and purple lines for case 1, 2, 3 and 4 respectively, for 4 different disks. The reference surface density profiles from the Lewis (1974) simple solutions are indicated by the dotted black lines. In addition the error bars of the surface density at 1 AU are shown.

spatial distributions are relatively well constraint (Pontoppidan, 2006; Henning and Semenov, 2013). Öberg *et al.* (2011) makes use of this in an attempt to predict the C/O ratio in planets formed at a certain location. This is done with a simple composition model, which only takes into account the three species H_2O , CO_2 and CO .

The temperature profile of the mid-plane is described by Equation 4.1. Öberg *et al.* (2011) uses values for T_1 and q that are taken from Andrews and Williams (2007) which was the source of the temperature comparison described above. From the set of 24 PPDs, a median for the temperature at 1 AU $T_1 = 200$ K and index $q = 0.62$ are found, which are used by Öberg *et al.* (2011) in Equation 4.1. Furthermore, the abundances of C- and O-bearing species are taken from Pontoppidan (2006). The abundances for a single YSO are estimated. In Table 4.3 the abundances of the most abundant C- and O-bearing species are given. In addition the evaporation temperatures are given.

Species	T_{evap}^a (K)	$n_{\text{O}} (10^{-4} \times n_{\text{H}})$	$n_{\text{C}} (10^{-4} \times n_{\text{H}})$
CO	18-22 (20)	0.9-2 (1.5)	0.9-2 (1.5)
CO ₂	42-52 (47)	0.6	0.3
H ₂ O	120-150 (135)	0.9	
Carbon grains	>150 (500)		0.6-1.2 ^c (0.6)
Silicate	≈1500 (1500)	1.4 ^c	

Table 4.3: Abundances and evaporation temperatures of C- and O-bearing species. In the cases where a range is indicated the value in parentheses is used.

With this information Öberg *et al.* (2011) is able to compute the C/O-ratios of the gas and the dust grains in the mid-plane of a typical disk. This is shown in Figure 4.4

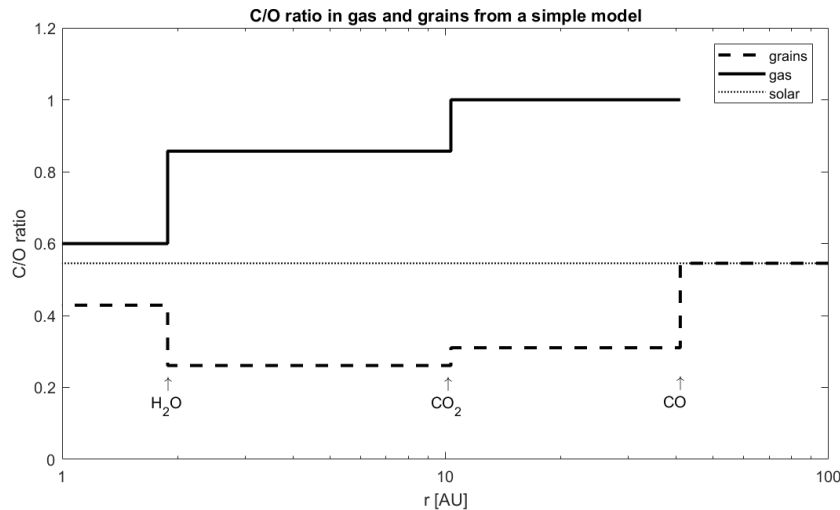


Figure 4.4: Recreation of the C/O ratio in the mid-plane as seen in Öberg *et al.* (2011). The thick solid line shows the C/O ratio in the gas phase, the dashed line is the C/O ratio in the grains and the dotted line indicates the solar C/O ratio of 0.5455 for reference. The snowlines for H_2O , CO_2 and CO are indicated from left to right.

The C/O is plotted for both the gas and the ices in the disk. As can be seen they change in steps. This is due to the assumption that solely the temperature dictates the phase of the molecules. This creates the steps at so called ice-lines of each species that contains Carbon or Oxygen. The location of the ice-lines, the radius where the disk temperature is equal to the evaporation temperature, for each of the considered molecules is indicated on the plot. It is seen that the C/O ratio of the gas is always higher than the star or super-stellar and the icy grains are always lower or sub-stellar. To the right of the water ice-line, the H_2O freezes out. This means that the concentration of elemental O goes down in the gas and up in the grains, and the relative elemental abundance of C goes up in the gas and down in the grains. When the CO_2 ice-line is crossed, both the C/O in the gas and in the grains go up. In the gas this is logical, more O goes out than C. For the grains it also goes up because the C/O of CO_2 is higher, 0.5, than of the ices before the ice-line, ~ 2.5 . From the CO ice-line all the molecules carrying C or O atoms, in the mid-plane are assumed to be in the ice phase.

To reproduce this figure with a ProDiMo model, approximately the same temperature profile should be used. As shown in section 4.1 the temperature profiles of the solution as used by Öberg *et al.* (2011) and ProDiMo have substantial differences. Therefore it will be impossible to reproduce the C/O ratio. This is attributed to the fact that the model of the mid-plane temperature is too simplistic. As a first general approximation this may be a good estimate however, for a specific PPD this model cannot be used to predict the mid-plane temperature and thus the C/O ratio in the mid-plane. Nevertheless, in section 4.3 the C/O of AA Tau is plotted. But this is not for comparison to the Figure 4.4.

4.3. Working model: AA Tau

As stated in chapter 3, ProDiMo is developed to produce synthetic SEDs of observed disks.

In the previous section it was attempted to fit the temperature profile computed by ProDiMo to a parametrized temperature profile of several observed disks. There, the flux density F_ν in Equation 4.4 was used to find a parametrized temperature profile. This resulted in a poor similarity of the temperatures. An alternative technique is to use the observed flux density instead of the parametrized temperature. As mentioned earlier, ProDiMo can produce a synthetic SED from the disk model. So by varying the parameters of the disk model, the fit of the model to the observations can be optimised. This is the strength of the synthetic observations of ProDiMo over parametrized fitting.

From several observational sources an SED are constructed by Woitke *et al.* (2019). Flux density observations include infra-red (IR) spectra from the Spitzer space telescope. ProDiMo is used to create a synthetic SED that fits the observations from several models. It is noted that among these models is again the PPD AA Tau.

Modelling of AA Tau is done in two steps. First the stellar parameters are fitted separately with a genetic algorithm. The stellar parameters include the stellar mass M_* , stellar luminosity L_* and the effective temperature of the star T_{eff} . Moreover, the UV and X-ray photons radiated onto the disk are determined. These parameters are essential to be able to reproduce the radiation field of the disk, which in turn has a great effect on the PPD model. In addition the interstellar extinction A_V is determined to correct for reddening of the SED due to interstellar dust. Reddening is caused by interstellar dust, it absorbs and scatters the stellar radiation of shorter or bluer wave-lengths more than longer redder wavelengths. This makes stars appear dimmer, but also redder than they actually are. To account for this in the synthetic SED, the spectrum is reddened by reducing the flux of the UV region more than the flux of the optical and IR region according to standard reddening law (Fitzpatrick and L., 1998). The reddened stellar SED is shown as the red line in Figure 4.5. Note that the left most region with the dark green line is the UV observation, the stellar UV is well fitted, so that the two lines almost exactly coincide.

The second step is to fit the SED of the star together with the PPD. This is done by ProDiMo, again with a genetic algorithm. The parameters that the disk is fitted to, are in the case of AA Tau: r_{in} , r_{out} , the radius at which the disk height starts to taper off r_{tap} , the total disk mass M_{disk} , surface density powerlaw index ϵ , reference scale height H_0 , flaring index β , strength of the turbulence α_{settle} , minimum dust grain size, maximum dust grain size and powerlaw index a_{min} , a_{max} and a_{pow} respectively. These fitted parameters are used in to generate the ProDiMo model. In Appendix A the complete set of input parameters is shown in `Parameters.in`. The resulting synthetic SED generated by ProDiMo is shown in Figure 4.5 as the black dotted line. To see the difference between the synthetic SED and the observations, larger black dots are indicated on the SED at the same wavelengths as the observations.

The AA Tau model that is determined by Woitke *et al.* (2019) is fitted to the observations with the time independent mode and without surface chemistry. As mentioned in section 3.3 and 3.2. The model that is used for the planet formation model does include time dependency and surface chemistry. Note that this means that the fit to the SED is not valid anymore. Some of the results are shown in Figure 4.6.

In Figure 4.6a it is seen that the dust is redistributed. However this is only done within each column. The colour bar has a logarithmic scale, so green means the dust to gas ratio is $10^{-2} = 0.01$, the global value. The dark red region in the outer disk at the mid-plane means that many dust particles have settled. The dust from the upper layers, the white region is depleted of dust.

Figure 4.6b shows the number of H nuclei in cm^{-3} . This is referred to as the density structure, because for the density, the abundance of other elements are negligible in comparison to the density of the number of H nuclei. The red inner disk close to the mid-plane is the densest region. Moving upwards or out ward decreases the density. The dark blue is the most tenuous region of the disk.

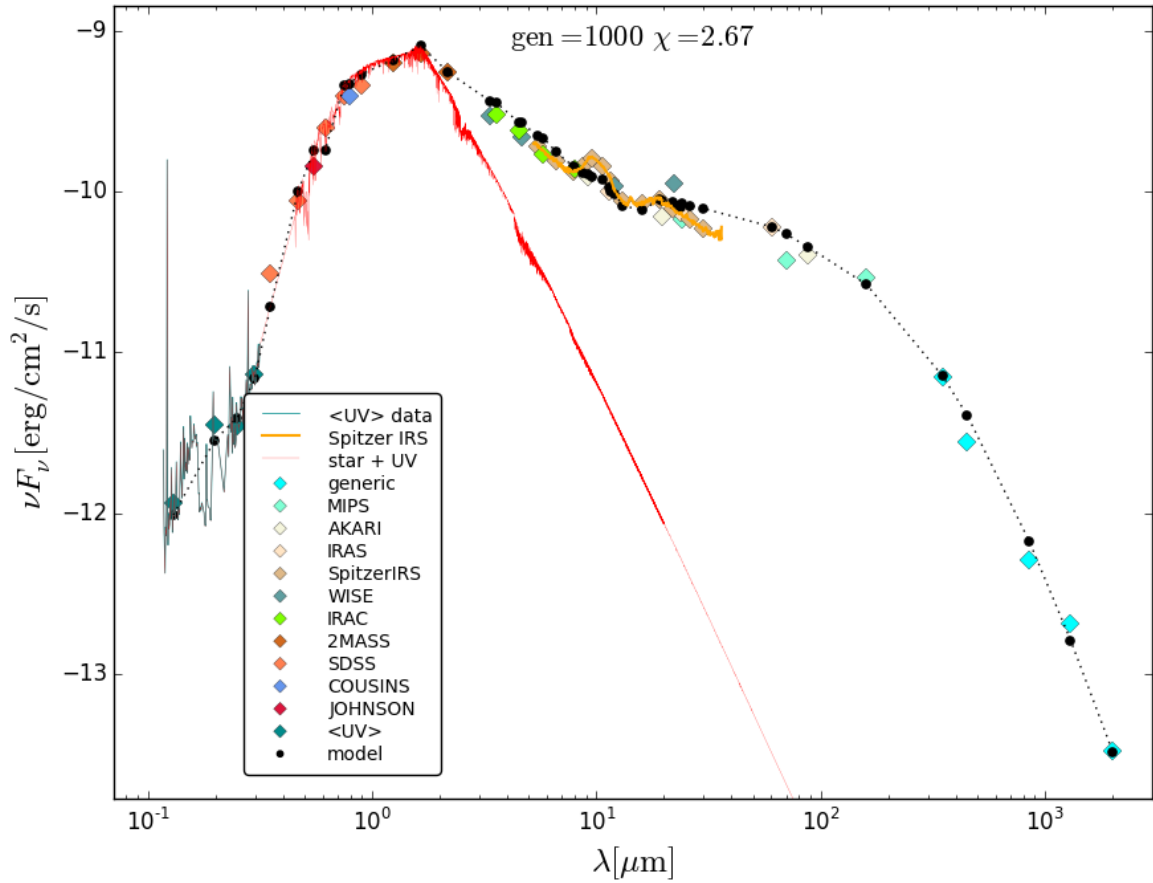
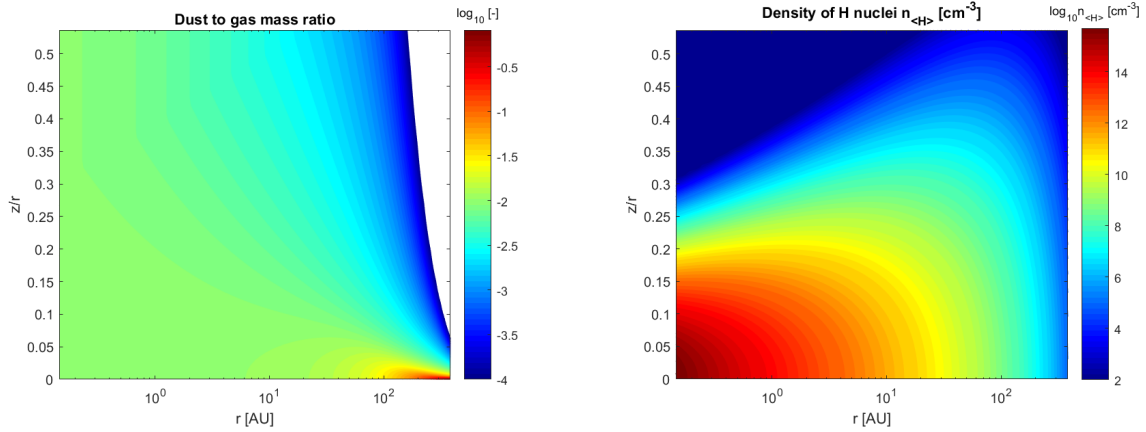
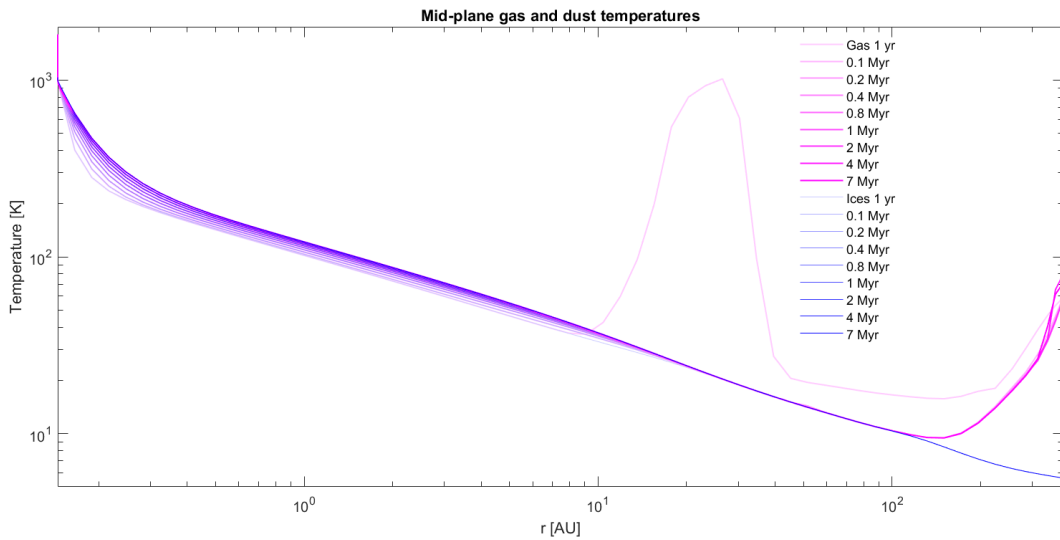


Figure 4.5: SED fitted by Woitke *et al.* (2019). The red line is the stellar fit, the black dotted line with black circles is the fitted PPD including the star. The coloured diamonds are the observations and the dark green line is the UV data. In addition IR observation from the Spitzer telescope that are used to fit the SED of the PPD is shown in orange.

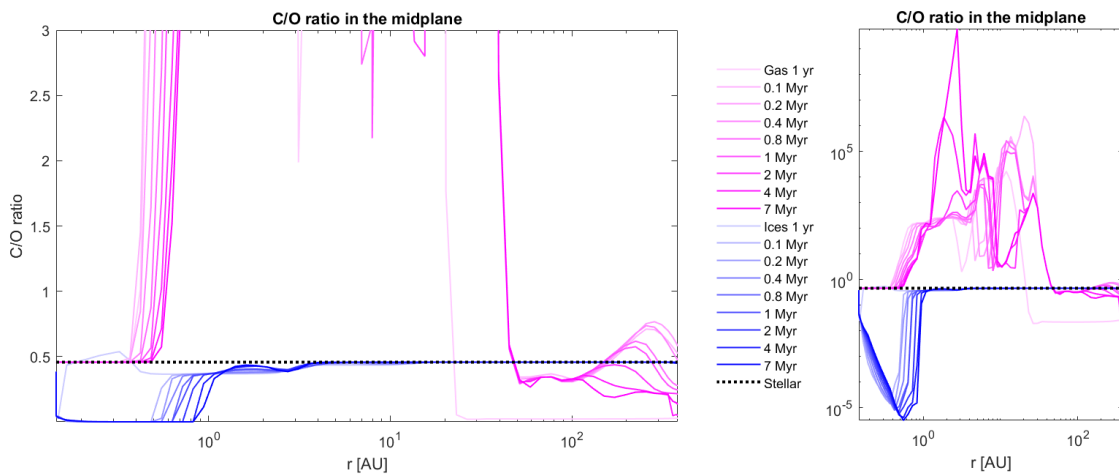


(a) Dust to gas ratio. A single colour would indicate a uniform dust to gas mass ratio.

(b) H nuclei distribution. This is also referred to as the density structure.



(c) Mid-plane gas and dust temperature, both the temperature and the radius are on a logarithmic scale. The magenta curves are gas temperature and the blue curves are the dust temperature. The curves at 1 yr are very light, the stronger the colour gets, the later in the disk life time.



(d) Mid-plane C/O ratio. The magenta lines are the gas C/O and the blue lines are the C/O of the ices. To scale of the left plot is to compare it to Figure 4.4. The right plot is to indicate the extreme values of the C/O ratio, especially of the gas.

Figure 4.6: Properties of the ProDiMo AA Tau model: gas to dust ratio, number of H nuclei $n_{<H>}$, Midplane temperatures, and the mid-plane C/O.

Note that the curves for gas and dust temperature in Figure 4.6c coincide for the most from the very inner disk up to 210 AU. The exception is the gas temperature at 1 yr, which shows a strong peak around 30 AU. This is attributed to a numerical error. 1 yr is very short for ProDiMo to converge to self-consistent steady state solution. Furthermore, the temperature of the disk increases over time.

Figure 4.6d is shown for comparison with the simple disk model in Figure 4.4. A detailed analysis of the C/O ratio of AA Tau is provided in section 6.3.

For the planet formation part of the thesis a single disk, AA Tau, will be used to generate results. A comparison between several disk would also be capable of characterising the types of planets that are formed in which type of disks. However, the focus is to find a way to correlate planet formation to the formation mechanism. Not how planet formation differs from disk to disk. Therefore a single disk is chosen which will be the working model. By choosing AA Tau, one of the PPDs fitted by Woitke *et al.* (2019), the results of the planet formation are as close to realistic as possible. Moreover, AA Tau will be simulated with the options for time-dependency and surface chemistry switched on. The input-files of the model, `Parameter.in` and `Elements.in` are shown in Appendix A together with a list of all species considered. There is another input file that is required to run ProDiMo; `Reactions.in`. However, this file contains over 2000 lines, so for practical reasons it is not included.

5

Formation of planets

The goal of the previous chapters was to simulate PPDs as close to reality as possible in preparation of forming planets. In this chapter the planet formation method as developed by Lambrechts and Johansen (2012, 2014); Lambrechts *et al.* (2014) is described. Then, in section 5.2, to be able to use the method with the ProDiMo model, some adjustments to the method and the model have to be made. These modifications are described in section 5.2. Finally, section 5.3, presents a simple method to determine the atmospheric mass of the planets given the core masses.

5.1. Pebble accretion

In this section the scenario of pebble accretion is described. In Figure 5.1 the scenario is visualised. The coloured bars represent the disk at increasing times. The first bar represents the initial disk defined at $t = 0$. This is where subsection 5.1.1 starts. The graphics at the remaining times will be described afterwards.

5.1.1. Dust evolution

Initially, the disk mass is assumed to consist of 1% dust mass of sizes comparable to ISM dust sizes only. This is depicted in the first bar of Figure 5.1. It was found by Mathis *et al.* (1977) that typical values of the ISM dust grains have radii varying between $R = 0.005 - 0.25 \mu\text{m}$. This very fine material is coupled to the gas. Collisions between the dust particles themselves can have several outcomes; fragmentation of both particles, erosion of both particles, ricocheting, partial mass transfer from one particle to another or sticking (Windmark *et al.*, 2012). Only the latter two outcomes result in overall growth of the particles, which seems not favourable. However, observations of PPDs prove that the particles grow to mm-sizes (Lambrechts and Johansen, 2014).

Once the dust reaches about $R \approx 1 - 10\text{mm}$, the dust particles, now called pebbles, become decoupled from the gas in the disk. This means that the gas pressure no longer supports sub-Keplerian speed of the particle. It tries to follow the Keplerian orbital velocity but feels the slower moving gas as a headwind. The aerodynamic drag force from the head wind slows the particle down causing orbit decay of the particle. This inward radial motion of pebbles decoupled from the gas is called pebble drift.

The growth time of the particles is given by Equation 5.1, which is a function of the orbital radius through the Keplerian frequency Ω_k in Equation 5.2.

$$t_g(r) = \frac{4}{\sqrt{3}\epsilon_g Z \Omega_K(r)} \quad (5.1)$$

$$\Omega_K(r) = \sqrt{\frac{GM_*}{r^3}} \quad (5.2)$$

Where ϵ_g is the particle growth efficiency and Z is the local dust to gas mass ratio. From the equations it can be seen that the larger the disk radius, the longer it takes for the dust to reach drift size. Note that

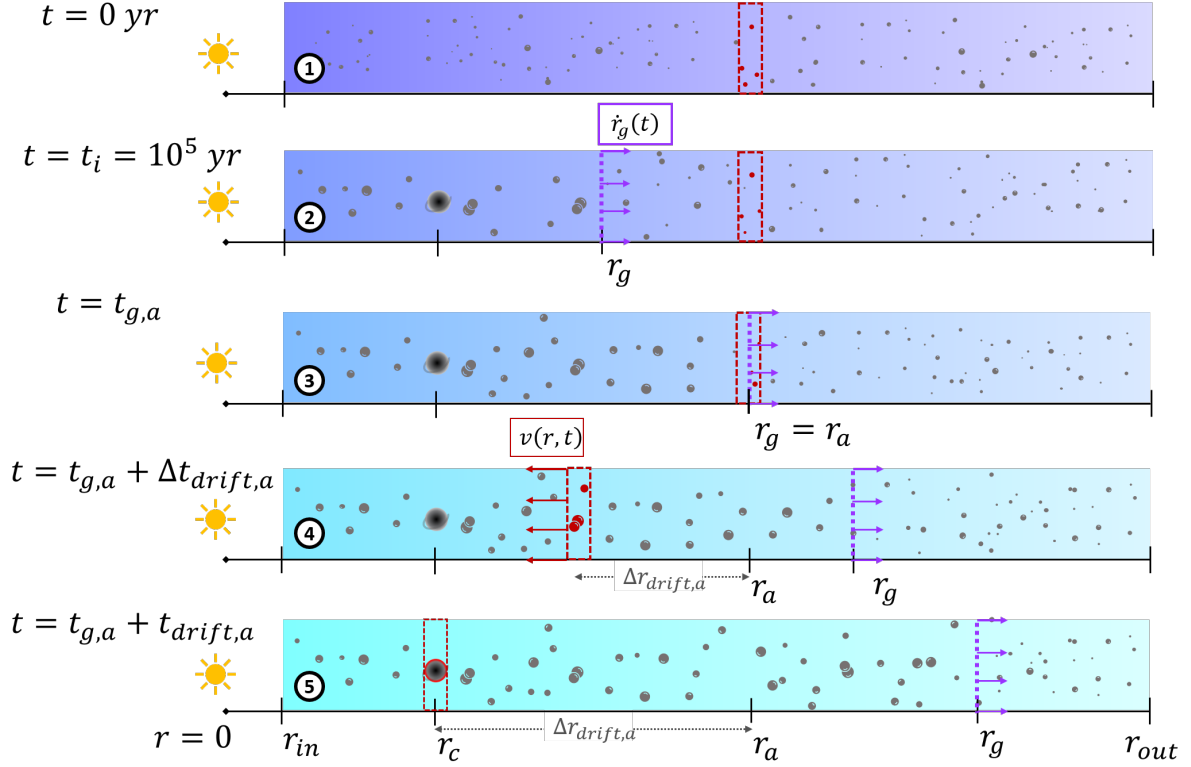


Figure 5.1: Schematic of the development of a PPD forming planets through pebble accretion. Each bar represents a specific time in the disk. The purple dashed line represents the pebble production line as described in subsection 5.1.1. The red dashed rectangles are used to describe where the composition of the ices comes from.

here the t_g is not dependent on the actual size of the dust, this is by design. Because it is not known a priori at what radius R_{drift} pebbles will start to drift.

To avoid having to define R_{drift} , a particle growth parameter ξ is introduced. This parameter is based on the ratio between the initial dust size, which is assumed to be of the same magnitude as the predominant sizes in the ISM $R_0 \approx 0.1-1\mu\text{m}$, and the size that seems to be consistent with observations $R_{drift} \approx 1-10\text{mm}$. So $\xi = \ln(R_{drift}/R_0) \approx 10$. $\epsilon_{g,d}$ is the dust sticking efficiency, and together with ξ , the growth parameter for the formation of drifting pebbles from ISM dust ϵ_d is defined as $\epsilon_d = \epsilon_{g,d}\xi^{-1}$. Using the same equation as Equation 5.1 the growth time from ISM dust to drifting pebbles Δt is given in Equation 5.3.

$$\Delta t = \frac{4}{\sqrt{3}\epsilon_d Z_0 \Omega_K(t)} \quad (5.3)$$

Where the Z_0 is the initial global gas to dust ratio.

5.1.2. Pebble drift and (solid) surface density

By drifting, the pebbles shift the solid mass distribution from the outer regions inward. At the inner disk, there is an influx of pebbles from the disk exterior to that which acts as a reservoir of pebbles. So a body in the inner region of the disk has the chance to gravitationally capture these pebbles that are drifting by. This process is shown by the last for disks in Figure 5.1.

The pebbles grow from the dust that is present in the disk and drift inwards depending on the gas density. So a model of a very large disk is set up by Lambrechts and Johansen (2014). As in most other disk models, the gas surface density profile in this model is described by a simple radial power law with a normalisation factor β . The gas surface density profile is given in Equation 5.4.

$$\Sigma_g(r, t) = \beta \left(\frac{r}{\text{AU}} \right)^{-1} \quad (5.4)$$

$$\beta(t) = \beta_0 e^{(-t/\tau_{\text{disk}})} \quad (5.5)$$

Where β_0 is a normalisation parameter controlling the disk surface density and is the surface density at 1 AU at $t = 0$. To mimic the natural dissipation of the gas in the disk during its life time, the initial surface density parameter is multiplied by a decaying exponential factor $\exp(-t/\tau_{disk})$. With τ_{disk} the dissipation time scale of the disk. This means that at time $t = \tau_{disk}$ the disk mass is only $e^{-1} \approx 0.367$ of the original disk mass. Subsequently, the dust surface density Σ_d is a constant fraction Z_0 of the surface density.

$$\Sigma_d(r, t) = Z_0 \beta \left(\frac{r}{\text{AU}} \right)^{-1} = Z_0 \Sigma_g(r, t) \quad (5.6)$$

This means that the dust surface density also decreases according to the exponential decay, simultaneously with the gas.

The Stokes number S_t is an important measure of particles in a fluid because the behaviour of a particle is not dependent on the characteristics of the particle only. Besides particle characteristics such as density and radius, its behaviour is also dependent on the local density, pressure, Keplerian frequency. Aerodynamically, a small particle behaves the same in a thin disk as a larger particle in a denser gas disk. Therefore, instead of analysing the behaviour of the particles as a function of physical size, it is chosen to use the Stokes number as the variable. This gives a better understanding of the dynamics of the particles.

The radial pebble drift time scale t_r is dependent on S_t as can be seen in Equation 5.7.

$$t_r = \frac{r}{v_r} \quad (5.7)$$

$$v_r = -2 \frac{S_t}{S_t^2 + 1} \eta v_K \approx -2 S_t \eta v_K \quad (5.8)$$

Where v_r is the radial speed of the inwards drifting pebbles, $v_K = r\Omega_K$ is the local Keplerian velocity and η is a measure of radially outward gas pressure support from the disk as shown in Equation 5.9.

$$\eta = -\frac{1}{2} \left(\frac{H}{r} \right)^2 \frac{\partial \ln P}{\partial \ln r} = \eta_0 \left(\frac{r}{\text{AU}} \right)^{1/2} \quad (5.9)$$

The pebble growth time $t_{g,peb}$ is shown in Equation 5.10. Note the similarity with Equation 5.1.

$$t_{g,peb} = \frac{4}{\sqrt{3} \epsilon_p (\Sigma_p / \Sigma_g) \Omega_K} \quad (5.10)$$

Where ϵ_p is the coagulation efficiency of pebbles between each other, Σ_p is the pebble surface density. So Σ_p / Σ_g is the pebble to gas ratio where in previous equations the dust to gas ratio Z_0 was used.

The Stokes number of the drifting pebbles can be found by calculating how much the pebbles have grown in the time that it has drifted. This means setting the drift Equation 5.7 and growth time Equation 5.10 equal to each other. The result is shown in Equation 5.11.

$$S_t \approx \frac{\sqrt{3} \epsilon_p \Sigma_p}{8 \eta \Sigma_g} \quad (5.11)$$

Since the pebbles are drifting, it is not sufficient to take the dust profile and convert it to pebbles at each radius. The solid mass redistribution by pebble drift should be taken into account. To do this the global pebble mass flux throughout the disk \dot{M}_{peb} is calculated as shown by Equation 5.12.

$$\dot{M}_{peb}(t) = 2\pi r_g \frac{dr_g}{dt} \Sigma_{d,0}(r_g(t), t) \quad (5.12)$$

The subscript 0 in $\Sigma_{d,0}(r_g(t), t)$ indicates that it is the initial dust surface density at time t , before pebbles have drifted away. Note that this is not necessarily the dust surface density at $t = 0$. The flux of pebbles is regulated by the time it takes the dust to grow to pebble size. The larger the disk radius the longer it takes to grow to drift sizes. This is depicted by Figure 5.1 as the purple dashed line that moves outward over the last four disks. This is referred to as the pebble production line. Equation 5.1 and 5.2

are rewritten to find the location r_g as function of time t where the pebbles just reached drift size, this is given in Equation 5.13. The derivative, $\frac{dr_g}{dt}$, is the speed at which r_g , or the pebble flux front, moves outward through the disk and is shown in Equation 5.14.

$$r_g(t) = \left(\frac{3}{16}\right)^{1/3} (GM_*)^{1/3} (\epsilon_d Z_0)^{2/3} t^{2/3} \quad (5.13)$$

$$\dot{r}_g = \frac{dr_g(t)}{dt} = \frac{2}{3} \left(\frac{3}{16}\right)^{1/3} (GM_*)^{1/3} (\epsilon_d Z_0)^{2/3} t^{-1/3} \quad (5.14)$$

The total pebble mass flux in the disk in Equation 5.12 can also be written as a function of the pebble surface density. It is equivalent to the relation shown in Equation 5.15.

$$\dot{M}_{peb}(t) = 2\pi r v_r \Sigma_p \quad (5.15)$$

Combining Equation 5.15, Equation 5.8 and Equation 5.11 results in Equation 5.16, the pebble surface density Σ_p .

$$\Sigma_p(r, t) = \sqrt{\frac{2\dot{M}_{peb}\Sigma_g}{\sqrt{3}\pi\epsilon_p r v_K}} \quad (5.16)$$

In Figure 5.2 the pebble surface density is shown for different times as well as the dust surface density for radii where the dust has not yet reached pebble sizes.

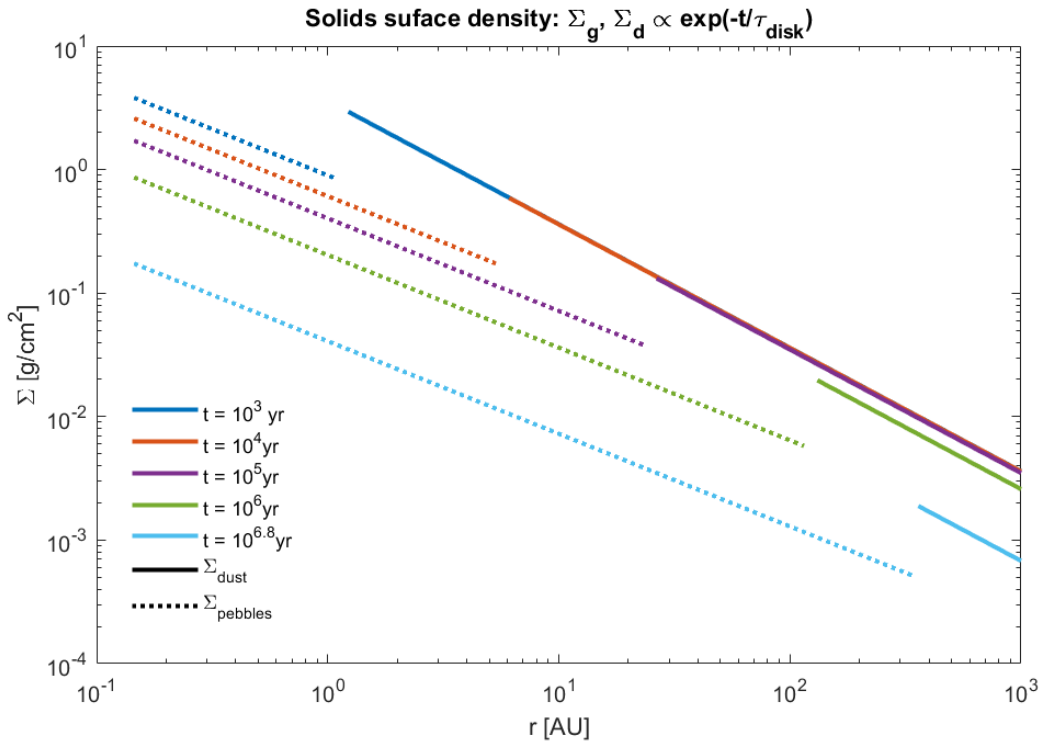


Figure 5.2: Solid surface densities of L&J14 for different times. The solid lines represent the dust surface density and the dotted lines are the pebble surface densities.

The different colours indicate different times, the solid lines are the dust surface densities and the dotted lines represent the pebble surface densities. The transition between the dotted and solid lines indicate the pebble production line r_g . Over time both the pebble and dust profiles are decreasing.

Upon careful examination of the lines, it is noticeable that the slope of the density is different for the pebbles and the dust. The slope of the dust $\Sigma_d \propto r^{-1}$ while the slope for the pebble surface density

is less negative $\Sigma_p \propto r^{-3/4}$. This slope difference is due to the fact that the dust does not move as a column, but rather spreads out over a larger radial section making the surface density lower.

Note that in this figure the total solid mass, $\Sigma_d + \Sigma_{peb}$ is not conserved. This is computationally explained by the fact that the pebble surface density $\Sigma_{peb}(r, t)$ is calculated with the surface density at time t but at a different radius, namely $r_g(t)$. Because as seen in Equation 5.12. Moreover, the pebbles drift inward to the star, reducing the overall mass and thus the local surface density of the region interior to the pebble production line.

5.1.3. Core growth

A planet-embryo with an initial mass $M_{c,0} \approx 10^{-3} M_{\oplus}$ is assumed to be present in the disk. Equation 5.17 shows the core accretion rate \dot{M}_c of the pebbles by the core.

$$\dot{M}_c(r, t) = 2 \left(\frac{S_t}{0.1} \right)^{2/3} r_H v_H \Sigma_p \quad (5.17)$$

$$(5.18)$$

Where r_H is the Hill radius of the planet for which the equation is given in Equation 5.19. The Hill radius is defined in a two-body system in a vacuum as the outer distance of the minor body, where a particle will orbit the minor body instead of the larger body. In 3-dimensional space this radius is translated to a sphere, the Hill sphere. So in this case the minor body is the planet embryo, the larger body is the central star and the particles are the pebbles. v_H is the velocity at the edge of the Hill sphere relative to the planet embryo calculated using Equation 5.20.

$$r_H = r \left(\frac{M_c}{3M_*} \right)^{1/3} \quad (5.19)$$

$$v_H = \Omega_K r_H \quad (5.20)$$

The accretion of pebbles from an arbitrary orbit around the core inside the Hill sphere to actual accretion onto the core is caused by the gas drag reducing the orbital energy. However, not all particles entering the hill sphere will be accreted by the core. Lambrechts and Johansen (2012) show that only pebbles with $S_t \approx 0.1$ will be accreted. This is visualised in Figure 5.3. Pebbles with $S_t \lesssim 0.01$ are too closely coupled to the gas and will only accrete onto the core when they pass the core at distances well inside the Hill sphere of the core. If $S_t \gtrsim 1$, then even pebbles crossing the orbit further than r_H will be deflected from its original path. However, the deflection does not always result in accretion but can lead to a horseshoe orbit of the pebbles. This can be seen as the grey dashed line on the bottom, starting at $x/r_H \approx -0.2$ curving back to the negative y/r_H direction.

So, Equation 5.17 corresponds to the accretion of pebbles crossing the orbit of the core within the distance of 1 Hill radius r_H of the core. The factor $(S_t/0.1)^{2/3}$ indicates that only and all pebbles with $S_t < 0.1$ are accreted. Writing out each of the variables and rewriting Equation 5.17, the result is shown in Equation 5.21.

$$\dot{M}_c(r, t) = \frac{dM_c}{dt} = \frac{2^{7/18} 3^{23/36} AU^{4/3} G^{13/36} \epsilon_d^{5/9} Z_0^{25/18} M_c^{2/3} \beta_0 e^{-t/\tau_{disk}}}{9\eta_0^{2/3} 0.1^{2/3} r^{5/12} M_*^{11/36} \epsilon_p^{1/6} t^{5/18}} \quad (5.21)$$

To get an expression for the core mass at time t , integration and some rewriting of Equation 5.21 is required as shown in Equation 5.22 to Equation 5.25.

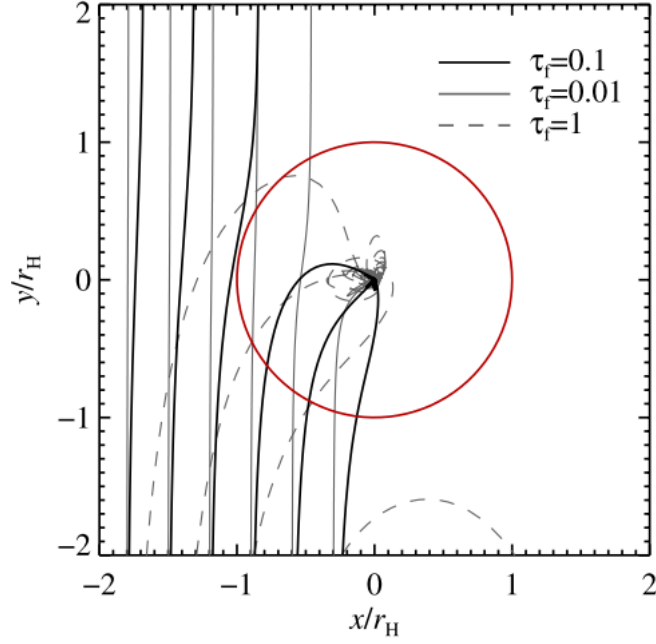


Figure 5.3: Visualisation of different pebble sizes passing a planetary core from Lambrechts and Johansen (2012). Black lines are pebbles with $S_t = 1$, and are all accreted by the core, grey lines indicate pebbles with $S_t = 0.01$ (solid) and $S_t = 1$ (dashed) of which only some of the pebbles are accreted depending on the distance x/r_H at which the core is passed.

$$\int_{M_{c,0}}^{M_c} M_c^{-2/3} dM_c = M_c^{1/3} - M_{c,0}^{1/3} = F_1 T_1 \quad (5.22)$$

$$F_1 = \frac{2^{7/18} 3^{23/36} AU^{4/3} G^{13/36} \epsilon_d^{5/9} Z_0^{25/18} \beta_0}{9 \eta_0^{2/3} 0.1^{2/3} r^{5/12} M_*^{11/36} \epsilon_p^{1/6}} \quad (5.23)$$

$$T_1 = \int_{t_i}^t \frac{e^{-t/\tau_{disk}}}{t^{5/18}} dt = -\tau^{13/18} \left(\Gamma\left(\frac{13}{18}, \frac{t}{\tau_{disk}}\right) - \Gamma\left(\frac{13}{18}, \frac{t_i}{\tau_{disk}}\right) \right) \quad (5.24)$$

$$M_c = \left(\frac{1}{3} F_1 T_1 + M_{c,0}^{1/3} \right)^3 \quad (5.25)$$

Where t_i is the time at which the planet embryo is introduced in the disk and $\Gamma(a, x)$ stands for the incomplete gamma function.

Furthermore, in order to find the core mass evolution for a specific disk case, each of the parameters have to be defined. The values of the required disk parameters are shown in Table 5.1. The values β_0 , M_* , Z_0 , τ_{disk} and η_0 are chosen because they represent the properties of a typical PPD. The values of $M_{c,0}$ and t_i are chosen to be reasonable. The results of the core mass development are minimally affected by the choice of these two values. The last three entries show the assumptions about the behavioural parameters of solids a disk environment. These are chosen to produce results that are comparable with numerical codes and observations (Birnstiel *et al.*, 2012; Weingartner and Draine, 2001).

The resulting mass development for four different core locations $r_c = 5, 8, 15, 20$ AU is shown in Figure 5.4. It is assumed that only a single core forms in the disk, and no migration is taken into account. From the figure it can be seen that there is a direct link between the radius of the introduced embryo and the mass it can accrete; the larger the orbital radius, the smaller the resulting core mass. The last two cores, $r_c = 15, 20$ AU, do not reach their isolation mass in the first 10 Myr.

$$M_{c,iso} \approx 20 \left(\frac{r}{5AU} \right)^{3/4} M_{\oplus} \quad (5.26)$$

Parameter	Symbol	value
Initial surface density at 1 AU	β_0	500 g/cm ²
Stellar mass	M_*	$1M_\odot$ (Solar mass)
Global dust to gas mass ratio	Z_0	0.01
Disk time scale	τ_{disk}	3×10^6 yr
Gas pressure coefficient	η_0	0.0015
Initial core mass	$M_{c,0}$	$10^{-3}M_\oplus$
Embryo insertion moment	t_i	10^5 yr
Dust sticking efficiency	$\epsilon_{g,d}$	0.5
Pebble coagulation efficiency	ϵ_p	0.5
Growth coefficient	ξ	10

Table 5.1: Input parameters for the core growth Lambrechts and Johansen (2014)

At some point the core will stop accreting solids. The mass at which the core stops accreting pebbles is called the isolation mass M_{iso} . This happens when the core is massive enough to perturb the gas just inside and outside of its orbit to form a shallow gap. The core keeps the gas out of this gap which can be seen as pushing the gas out of the gap. So the gas of the disk just outside of the outer edge of the gap experiences an increased radially outward pressure (Johansen and Lambrechts, 2017; Lambrechts *et al.*, 2014). The mass at which this isolation from pebbles is shown in Equation 5.26.

Table 5.2 shows the core isolation masses and the time of the isolation t_{iso} .

r_c [AU]	M_{iso} [M_\oplus]	t_{iso} [Myr]	$M_{c,3Myr}$ [M_\oplus]
5	20	1.42	20
8	28.5	2.36	28.5
15	45.6	no iso	16.8
20	56.6	no iso	11.9

Table 5.2: Core theoretical core isolation mass $M_{c,isco}$, computed isolation time t_{iso} and the final mass at 3Myr. 'no iso' indicates that the isolation mass is not reached in the first 10 Myr.

5.2. ProDiMo disk model modifications

The method that is used to calculate the core mass evolution is adopted from Lambrechts and Johansen (2014), as explained in section 5.1. However, instead of using the standard simple logarithmic prescription of the surface density profile from Equation 5.4, Σ_g is taken from the disk AA Tau as discussed earlier in chapter 4. The profiles for gas and dust surface densities are shown in Figure 5.5 together with the simple power-law as adopted by Lambrechts and Johansen (2014). The disk structure computed by ProDiMo has a better resemblance to what a real PPD looks like. So, this modification should result in a more realistic surface density especially in the outer region. In the power-law the outer edge the disk is resembled by a sudden drop of the density and pressure which is physically impossible.

In order to compare the two methods, the original and a modified version of Lambrechts *et al.* (2014), some of the parameters of the disk of Lambrechts and Johansen (2014) are adjusted. β_0 is changed from 500 g/cm² to 360 g/cm². Furthermore, the central star of Lambrechts and Johansen (2014) has mass of $M_* = M_\odot$ which is changed to $M_{*,AATau} = 0.85M_\odot$. The dust to gas ratio Z_0 is the same for both model. The density profile provided by ProDiMo is not time dependent. To mimic gas dissipation over time the same exponential decay function as in Equation 5.5 is used with the same τ_{disk} .

Following the procedure described in section 5.1 the solid surface densities are determined for the modified disks. In Figure 5.6 dust and pebble surface density profiles for different times are shown. The shape $\Sigma_{d,pr}$ for each time stays clearly recognisable. Moreover, for $\Sigma_{p,pr}$ the shape is also still noticeable.

Note that the latest time for which the surface densities are shown is not $t = 10^7$ but $t = 10^{6.8}$. It is assumed that the mass flux in the disk is uniform over all radii at any time. The quantity of pebble flux is determined by the amount of pebbles that start drifting at the pebble production line. Once the

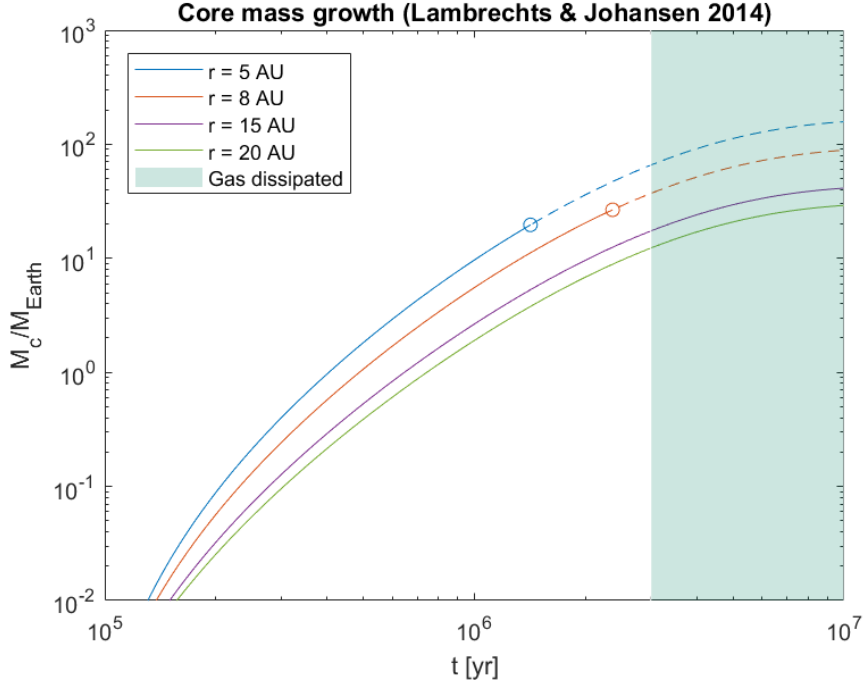


Figure 5.4: Reproduction of core growth over time as calculated by (Lambrechts and Johansen, 2014). The circles on the first two cores indicate the isolation of the core from pebbles to halt the mass growth. The dashed lines are the paths the mass would have followed if the core would continue accreting the pebbles that are drifting by after pebble isolation. The shaded region on the right hand side of the plot indicates that the gas t exceeds the disk dissipation time scale τ_{disk} .

pebble production line reaches the outer edge of the disk there is no more dust to convert into pebbles, leading to a termination of the pebble flux. So M_{peb} and in turn Σ_p is terminated at the time that pebble production line reaches the outer edge of the disk. This final pebble production time $t_{g,fin}$ is calculated by Equation 5.27.

$$t_{g,fin} = \frac{4}{\sqrt{3}\epsilon_g Z \Omega_K(r_{out})} \quad (5.27)$$

$$\Omega_K(r_{out}) = \sqrt{\frac{GM_*}{r_{out}^3}} \quad (5.28)$$

The outer edge of the AA Tau model is 383 AU, so the pebble flux is terminated at $t_{g,fin} = 10^{6.8}$ yr. In reality the pebbles that are already drifting will not stop drifting because of the termination of pebble production. But the drift time is small compared to $t_{g,fin}$ so this is not taken into account which has insignificant consequences.

To compute the core growth as a function of time the equations used by Lambrechts and Johansen (2014) have to be modified. Equation 5.29 is the same as Equation 5.21 but without all of the variables written out to their basic elements.

$$\dot{M}_c(r, t) = \frac{dM_c}{dt} = \frac{2^{2/3} r^{7/6} [r_g(t) \dot{r}_g(t) \Sigma_{d,0}(t)]^{5/6} \Sigma_g(r, t) \Omega_K(r)}{3^{3/4} \eta(r)^{2/3} 0.1^{2/3} v_K(r)^{5/6} M_*^{2/3} \epsilon_p^{1/6}} M_c^{2/3} \quad (5.29)$$

This gives an insight into the variables that are dependent on t and which ones are not.

In section 5.1 $\Sigma_{d,0}$ was a simple function of time which can be integrated analytically. However, when using ProDiMo to describe the disk, the relation between $\Sigma_{d,0}$ and t is not analytical, so it is not possible to do an analytic integration to find the core mass. The equation is solved using a numerical method, the trapezium rule is used.

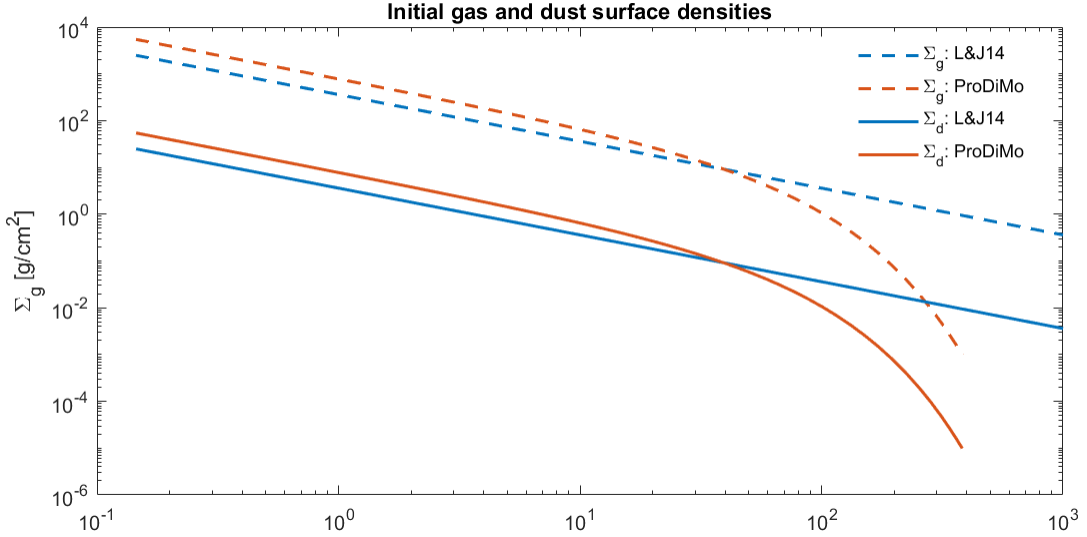


Figure 5.5: Initial gas and dust surface densities of Lambrechts and Johansen (2014) and ProDiMo.

$$\int_{M_{c,0}}^{M_c} M_c^{-2/3} dM_c = M_c^{1/3} - M_{c,0}^{1/3} = F_2 T_2 \quad (5.30)$$

$$M_c = \left(\frac{1}{3} F_2 T_2 + M_{c,0}^{1/3} \right)^3 \quad (5.31)$$

$$F_2 = \frac{2^{2/3} r^{7/6} \Sigma_g(r, t) \Omega_K(r)}{3^{3/4} \eta(r)^{2/3} 0.1^{2/3} v_K(r)^{5/6} M_*^{2/3} \epsilon_p^{1/6}} \quad (5.32)$$

$$T_2 = \int_{t_i}^t (r_g(t) \dot{r}_g(t) \Sigma_{d,0}(t))^{5/6} dt \quad (5.33)$$

$$\approx \sum_{j=1}^{n_t} [r_{g,j-1} \dot{r}_{g,j-1} \Sigma_{d,0,j-1}(r)]^{5/6} + [r_{g,j} \dot{r}_{g,j} \Sigma_{d,0,j}(r)]^{5/6} \frac{\Delta t_j}{2} \quad (5.34)$$

Where n_t is the number of time steps for which r_g , \dot{r}_g and $\Sigma_{d,0,j-1}$ are evaluated. The resulting core growth is shown in Figure 5.7.

r_c [AU]	$M_{c,iso}$ [M_\oplus]	$\Sigma \propto r^{-1}$		Σ by ProDiMo	
		t_{iso} [Myr]	$M_{c,3Myr}$ [M_\oplus]	t_{iso} [Myr]	$M_{c,3Myr}$ [M_\oplus]
5	20	2.3	20	<i>no iso</i>	0.81
8	28.5	5.3	28.5	<i>no iso</i>	0.47
15	45.6	<i>no iso</i>	7.58	<i>no iso</i>	0.23
20	56.6	<i>no iso</i>	5.40	<i>no iso</i>	0.16

Table 5.3: Core isolation masses with times if they are reached. The mass at 3 Myr is also shown in the columns $M_{c,3Myr}$.

From this figure it can be concluded that there is no radius for at which a core forms of even $1 M_\oplus$. This is problematic for gas giants to form since the critical mass for rapid gas accretion is $M_{crit} = 10 M_\oplus$. Analysis of the method gives an insight on the reasons why the cores stay so small. With the present set of parameters, the formation of small cores is not possible. In the next paragraph, we describe the uncertainties coming from the model.

Dust to gas ratio :

As explained in chapter 2 once dust particles reach a certain size, they become invisible for

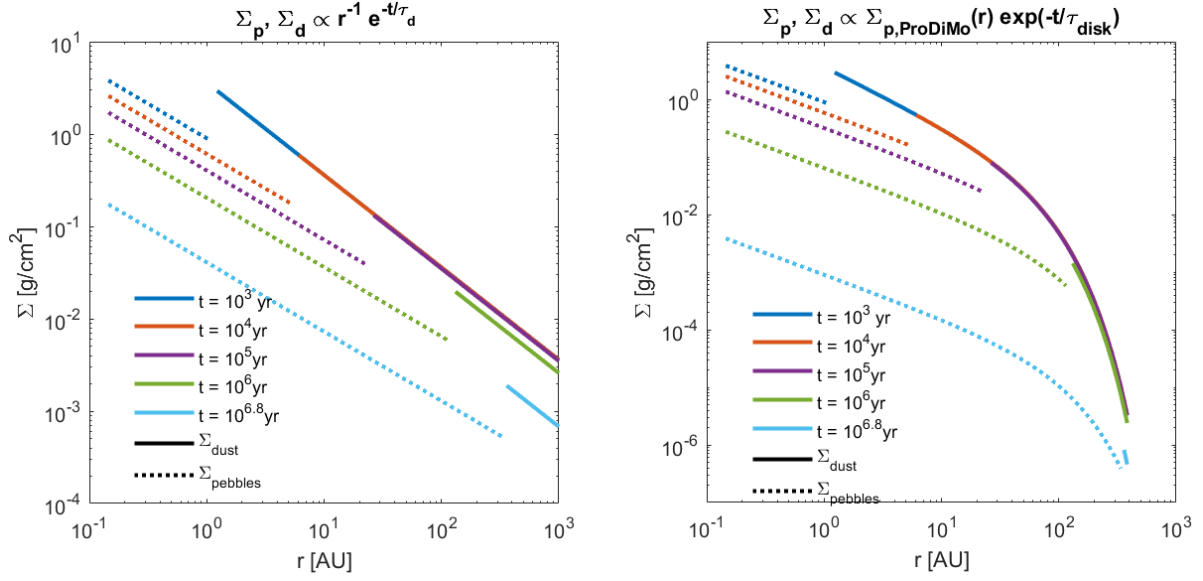


Figure 5.6: Solid surface densities of Lambrechts and Johansen (2014) on the left and ProDiMo on the right, for different times. The solid lines represent the dust surface density and the dotted lines are the pebble surface densities.

observations with the current instruments. This means that the dust mass that is actually in the disk can be much higher than what can be observed. (Z_0 is not one of the fitting parameters for ProDiMo's AA Tau *Woitke et al. (2019)*).

Dust coagulation efficiency :

The value of $\epsilon_{g,d} = 0.5$ as used by Lambrechts and Johansen (2014) seems very optimistic. This means that for every two collisions of two dust particles, one will result in a combined particle with the combined mass of the two original dust particles. According to *Fraser et al. (2015)* the majority of the collisions result in bouncing.

Increasing Z_0 or reducing $\epsilon_{g,d}$ will increase the mass accretion rate as can be seen in Equation 5.21. However, it will also result in rapid depletion of pebbles due to the higher speed of the pebble production line through the disk. This can be analysed from Equation 5.14. In addition Figure 5.8a shows the mass evolution when Z_0 is kept the same, while the dust coagulation efficiency is reduced to $\epsilon_{g,d} = 0.5/3 = 0.17$, and Figure 5.8b when the dust to gas ratio is increased to $Z_0 = 0.01 \cdot 3 = 0.03$.

By reducing $\epsilon_{g,d}$ the dust is converted into pebbles at a slower rate so the pebble production line has a reduced velocity. This results in a lower \dot{M}_{peb} , and a reduced \dot{M}_c leading to very slow mass accretion. So in this case only on critical cores are formed before the gas is dissipated.

Increasing only Z_0 results in very rapid pebble formation. The pebble production line moves through the disk so fast that the outer edge of the disk is reached at ~ 2 Myr. So there is a large influx of pebbles early in time, and then stops early as well. This can be recognised as the steep slope early in the plot, and the end of the curves at ~ 2 Myr. Moreover, the amount of pebbles that the core can accrete at a time is limited. Especially at low core masses the fraction of the pebble flux that can be accreted is small. So by the time the core is large enough to accrete the larger fractions of the pebbles, the pebble flux itself has already declined.

So changing each of the parameters separately does not lead to larger cores. Changing Z_0 and $\epsilon_{g,d}$ together the pebble production line can be held at the same speed, while increasing \dot{M}_c . The Z_0 is multiplied by 3 while $\epsilon_{g,d}$ is divided by 3, which will be referred to as Disk 1. This keeps the pebble production line equivalent to the original values. The result is shown in Figure 5.9.

In Figure 5.10 the final core mass as a function the radius is shown for core radii between 0.5 and 26 AU. It can be seen that the curve consists of two parts; 0.5 up to 4.8 AU, and from 4.8 AU upward. This division is caused by the fact that up to 4.8 AU the isolation mass is reached before the pebbles stop coming by. Further out from this, the pebble accretion stagnates due the termination of \dot{M}_{peb} .

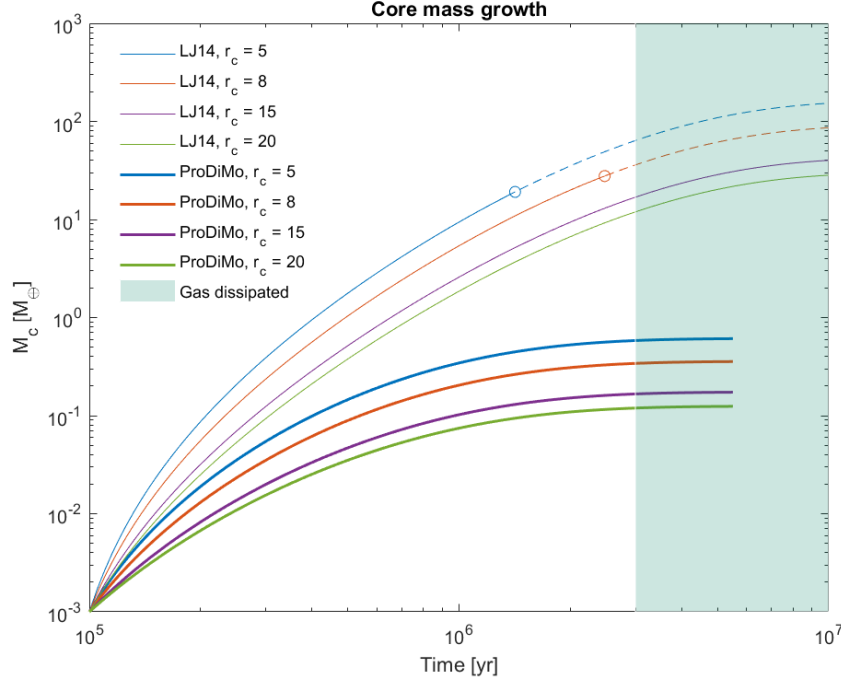


Figure 5.7: Core growth over time for the AA Tau evaluated with both the Σ calculated by ProDiMo and the simple exponential Σ .

5.3. Gas giant atmospheres

As opposed to the planetesimal accretion scenario, for the pebble accretion scenario there is not much literature about how the gas or atmosphere accretion develops. Therefore, for the cores that reach $M_{c,crit}$ the method that is used to calculate the gas mass that is accreted is very simple.

First, the conditions for accreting large amounts of gas must be determined. Once a core has formed it may be massive enough to also accrete a massive gaseous atmosphere. Three conditions are identified:

1. M_c : The core must be massive enough to be able to gravitationally compress the gas, so a minimum mass of $10 M_{\oplus}$ (Lambrechts and Johansen, 2014).
2. \dot{M}_c : The accretion of pebbles onto the core has an effect on the direct environment of the core, referred to as the envelope. This can be viewed as a small atmospheric layer. It is made up of dust particles and gas from sublimated ices from pebbles due to the heat that is released from the accretion of pebbles. This envelope is sustained in hydrostatic equilibrium by gravitational potential and the atmospheric pressure that is maintained by pebble accretion. When the pebble accretion rate decreases, the amount of heat and gas released into the atmosphere decreases as well. So there can exist a moment during pebble accretion that the hydrostatic equilibrium can not be sustained any longer, which leads to rapid accretion of massive amounts of gas can start (Lambrechts *et al.*, 2014).
3. t : The disk dissipation time scale is important. If the right mass and mass accretion rate conditions occur too late in the disk life time, there will not be enough gas left in the disk to accrete the massive atmospheres.

In this project, the conditions for the onset of gaseous envelope accretion is simplified:

1. $M_c = M_{c,crit} = 10 M_{\oplus}$.
2. $\dot{M}_c \approx 0$
3. $t < \tau_{disk}$

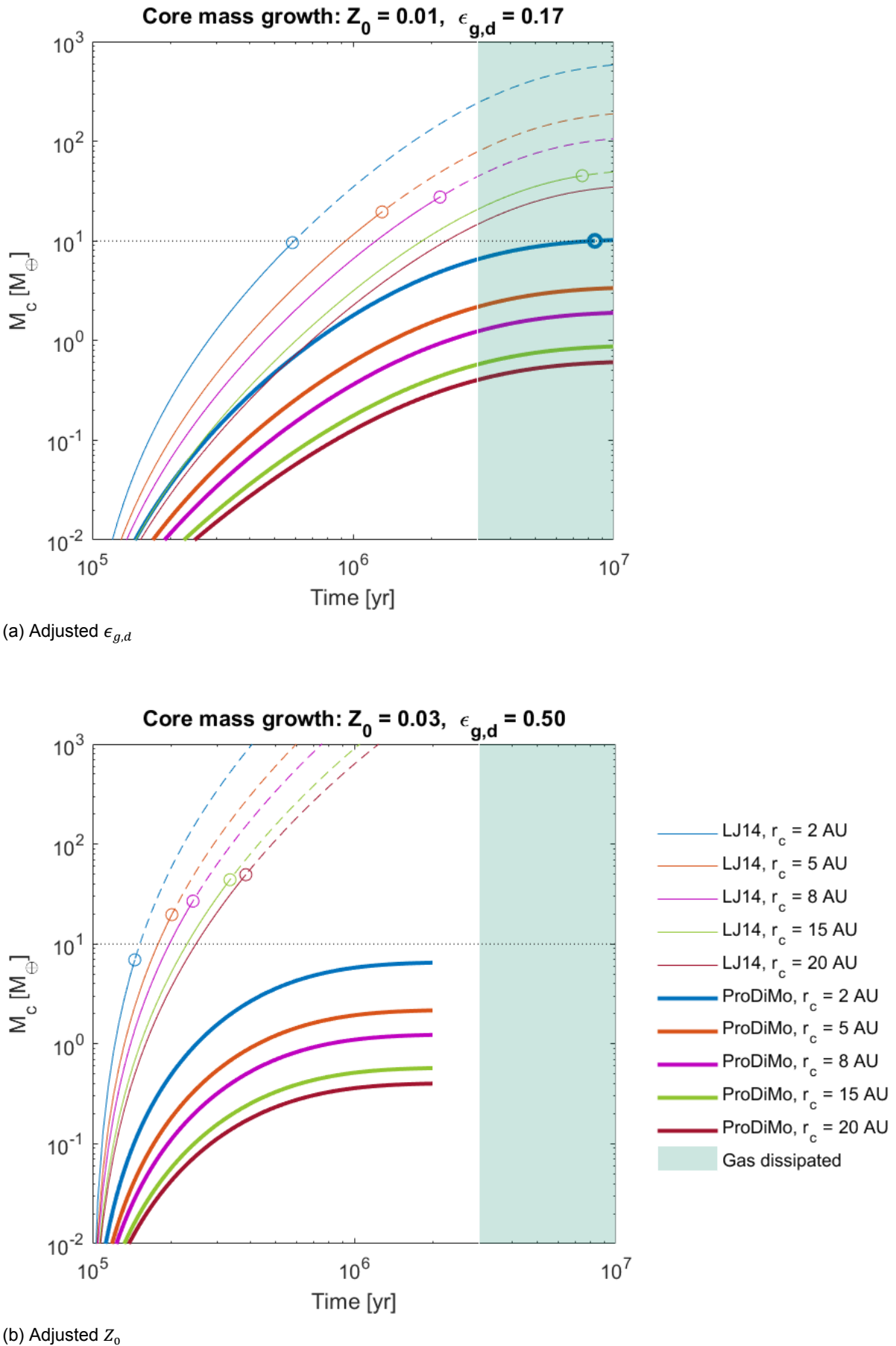


Figure 5.8: Mass evolution with adjusted coagulation efficiency and dust to gas mass ratio respectively.

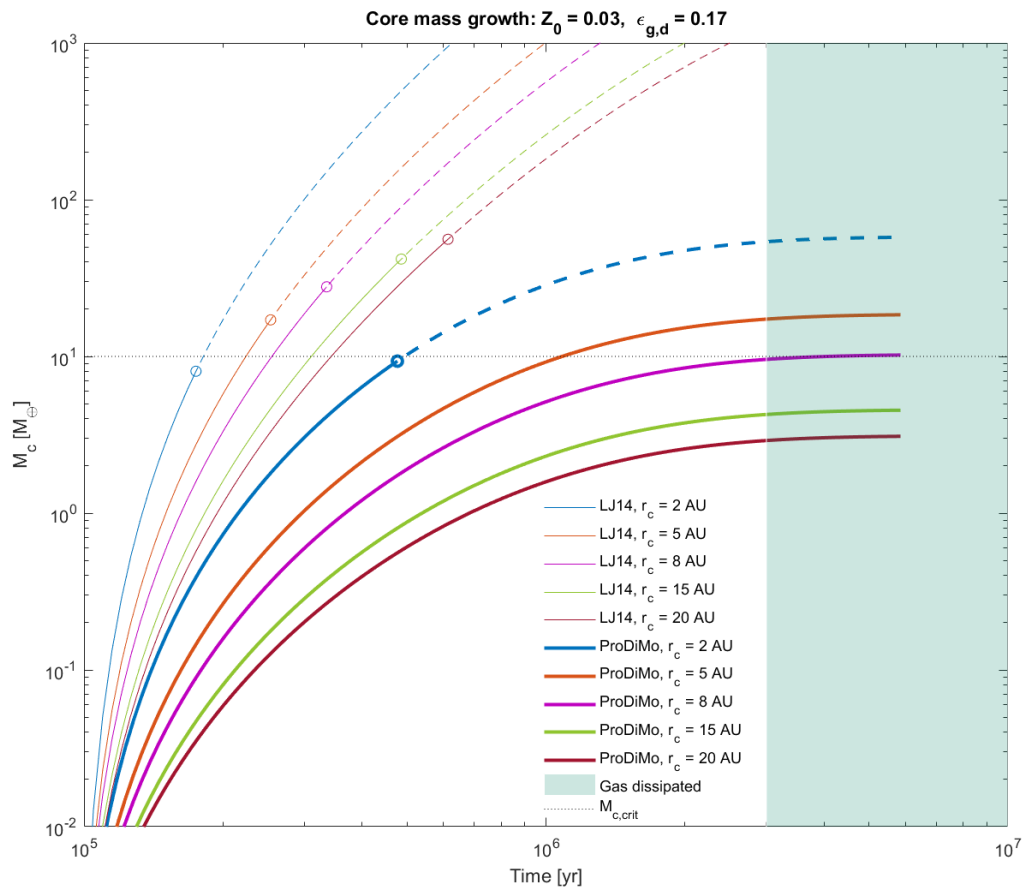


Figure 5.9: Mass evolution for Disk 1 with $Z_0=0.03$, and $\epsilon_{d,g} = \epsilon_p = 0.17$ at several radii.

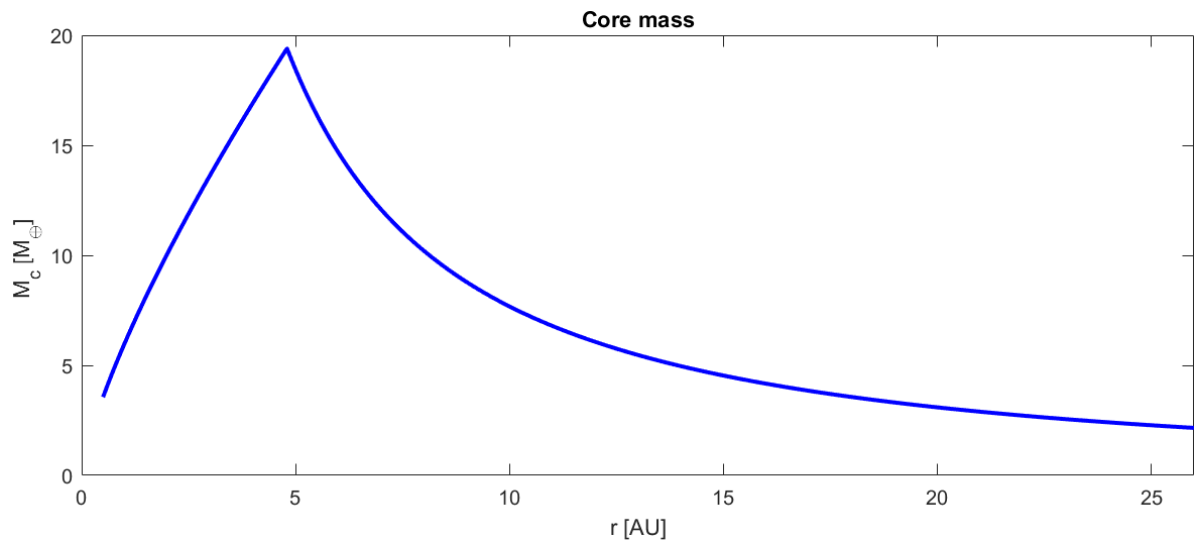


Figure 5.10: Final core mass as a function of the radius.

If and when the core complies to all these criteria, a gaseous envelope is assumed to accreted. A simple method to estimate the mass of the atmosphere and the total planet mass is used. It is assumed that the planet clears annulus of gas from the disk. The width of this gap is defined by the Hill radius r_H of the planet. So by integrating the surface density between $r_H - r_c$ and $r_H + r_c$ and approximation of the total atmospheric mass can be determined. This integral and the summation to solve it numerically are shown in Equation 5.35.

$$M_g = 2\pi \int_{r_c - r_H}^{r_c + r_H} \Sigma_g r dr \quad (5.35)$$

$$\approx 2\pi \sum_{j=1}^n \frac{\Sigma_g(r_{j-1})r_{j-1} + \Sigma_g(r_j)r_j}{2} \Delta r_j$$

The sum of the core mass and the atmospheric mass is the planet mass M_p . The Hill radius r_H is determined by Equation 5.36, which is similar to Equation 5.19, but now with M_p instead of M_c .

$$r_H = r \left(\frac{M_p}{3M_*} \right)^{1/3} \quad (5.36)$$

This is important because this means that r_H and M_p are interdependent. So an iterative scheme must be used to find the final planet mass.

This is shown in the flow diagram in Figure 5.11.

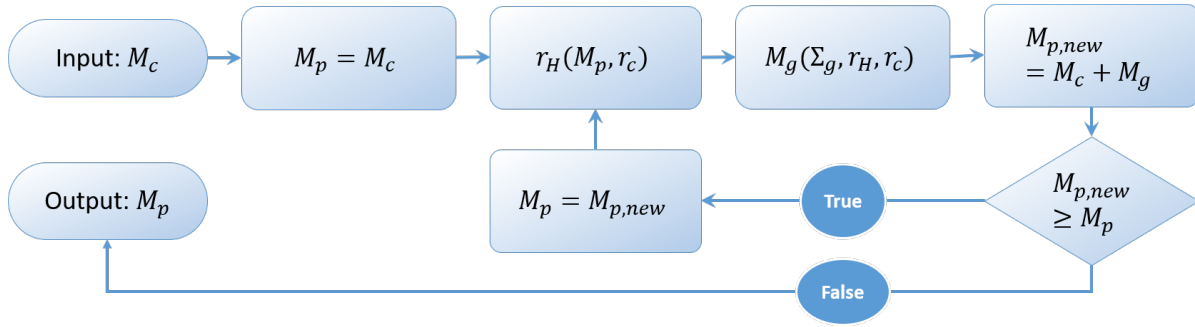


Figure 5.11: Flow diagram of the method used to compute the Planet mass when it forms a gap of $2r_H$ at the radius of core formation.

First r_H is calculated using $M_p = M_c$. Then M_g is calculated using Equation 5.35. If $M_c + M_g$ is larger than M_p , M_p is set to $M_c + M_g$ which is then used to calculate the new r_H . If on the other hand $M_c + M_g$ is equal to or smaller than M_p , $M_c + M_g$ is taken as the final planetary mass.

This method to compute the gas mass and the total planet mass is applied to the cores that are formed in section 5.2. In Figure 5.12 the results are shown.

From this figure, it is seen that cores will only accrete a giant atmosphere between 2 and 8 AU. Outside of this interval, the core does not reach the critical mass of $10 M_\oplus$. The radii where gas giants form can also be divided into 2 regions, separated by 4.8 AU where M_{iso} is reached just before the pebble flux is terminated.

Even though the core mass increases up to 4.8 AU, the atmospheric mass first increases, and then rapidly decreases with radius. The decrease is attributed to the fact that the gas dissipates from the disk with time scale τ_{disk} . The highest planet mass, at $M_p = 110 M_\oplus$, does not correspond to the highest core mass where the $M_p = 38 M_\oplus$. So for a high planet mass it is more favourable to reach the critical core mass and isolation mass early, than it is to take more time to accrete a high core mass.

For the radii higher than 4.8 AU the core mass declines but the atmospheric mass increases. The result is that the planet mass stays approximately constant at $M_p \sim 37 M_\oplus$ for all radii in this region and even increases a little bit in the end. Note that from 4.8 AU the final mass is reached at the time that the pebble flux is terminated. This moment is the same for the entire disk. It means that between radii in this region the disk does not dissipate any further. The final core mass increases a little bit with radius, because further from the star, r_H is larger.

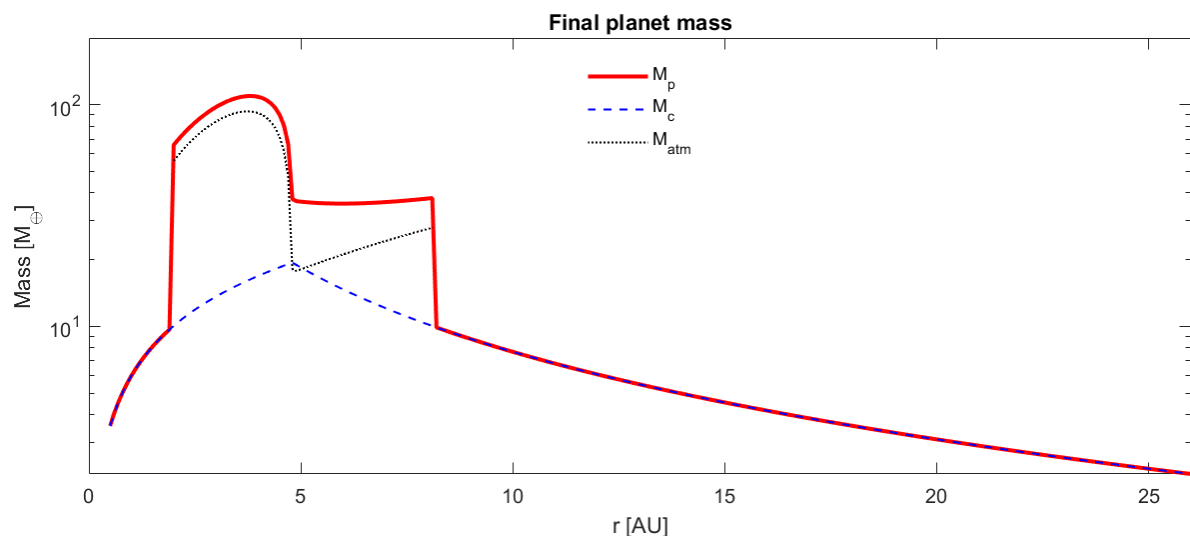


Figure 5.12: The dashed blue line is the core mass, the dotted black line is the mass of the atmosphere, and the solid red line is the total planet mass.

Planet composition

In chapter 5 the mass of the core and the atmosphere of planets forming in AA Tau is calculated. The result is useful to determine whether planets and gas giant will form. However, the composition of the resulting planets are not known yet. In this Chapter, the mass accretion is converted into accretion of material with different composition. First for the core and after that for the atmospheres if the conditions are adequate for gas accretion.

6.1. Pebble core compositions

The core mass evolution of the planet cores have been determined in the last chapter. The final step is to combine it with the ProDiMo composition data of AA Tau to get the composition of the cores. To do this it is essential to relate the mass accretion rate to the location where the mass came from.

So, in order to compute the chemical composition of the final cores, the composition of the pebbles accreted has to be determined as a function of time. To do this the fraction of $\dot{M}_{c,x}$ for each species x the mass fraction $f_{x,ice}$ at each time at the core location is computed. Then the mass accretion rate for each species $\dot{M}_{x,ice}$ can be computed as shown in Equation 6.1.

$$\dot{M}_{c,x} = \dot{M}_c(t) f_{x,ice}(t) \quad (6.1)$$

$$M_{c,x} \approx \sum_{j=1}^N \frac{\dot{M}_{x,ice}(t_{j-1}) + \dot{M}_{x,ice}(t_j)}{2} \Delta t_j \quad (6.2)$$

$$1 = \sum_{x \in \text{Species}_{ice}} f_{x,ice}(t) + f_{dust}(t) \quad (6.3)$$

Integrating the species accretion rate $\dot{M}_{c,x}$ over time leads to the total mass fraction of the core that consists of species x . This is computed using numerical integration as shown in Equation 6.2. Moreover, the pebbles consists mostly of dust material. The dust mass is computed in the same fashion using the fraction of the accreted mass at each time that consists of dust $f_{x,ice}$. So the sum of all the fractions $f_{x,ice}$ and dust fraction f_{dust} must add up to 1 as shown in Equation 6.3.

For the core mass evolution with the method of Lambrechts and Johansen (2014), it is not necessary to determine the composition or location origin of the mass that is accreted. For this it is sufficient to determine the quantity of pebbles that is accreted. As can be seen from Equation 5.16 the factor that is responsible for the composition is the pebble surface density Σ_p . The other factors have no effect on the composition. In turn the composition of the surface density Σ_p is dependent on M_{peb} . Looking at how M_{peb} is calculated in Equation 5.12, the pebble mass flux is not calculated at the location of accretion. Instead, the equivalent quantity of material is calculated at the pebble production line for that time using $\Sigma_{d,0}(r_g, t)$. A method to determine the composition is developed and presented next.

To get the location of origin of the accreted material, the time history of the pebbles has to be tracked. For this Figure 5.1 is used again. A column of material at some location r_a is followed, this material is indicated by the dashed red rectangle. Disk 1 depicts time $t = 0$ yr. The evolution of the accreted

material can be divided into two phases: chemical evolution and dynamic evolution. The first phase, chemical evolution, starts when the disk is formed, $t = 0$ in disk 1, and ends at the time that the dust is grown to pebble size which consequently start drifting. The end of phase one can also be explained as the time it takes the pebble production line to reach r_a . During phase one, the material is assumed to be stationary and the evolution of the material is only chemical as explained in section 3.3. The end of the first phase marks the start of the second phase. This transition moment is shown in disk 3, where the pebble production line, the purple line, meets the column of particles at r_a . At the beginning of phase two the pebbles set an inwards course towards the central star with velocity $v(r, t)$ (Equation 5.8). The second part is ended by reaching the orbit of the planet core as depicted in disk 5. The arrival at the orbit at the end of phase two is sufficient for the calculation of the core composition. At this point it is either accreted by the planet core or drifts past the core towards the central star of the disk.

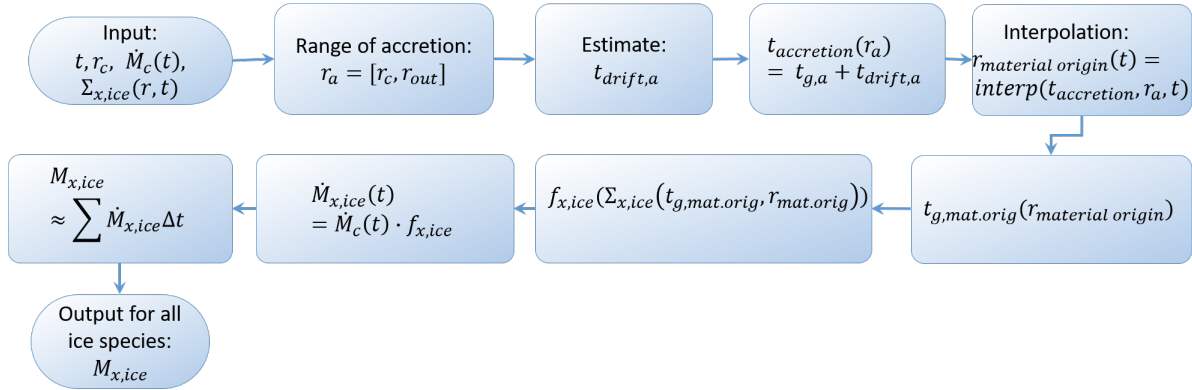


Figure 6.1: Flow diagram of the calculation of composition of the core mass accreted through pebble accretion.

The r_c for which the composition is computed are different from the cores that are formed in chapter 5. This is done deliberately so that a variety of cores can be generated. There are two r_c for which the core just reaches the critical mass $M_{crit} = 10M_{\oplus}$. The first, at 2 AU, is cut off at M_{iso} due deflection of pebbles instead of accretion by the core. The other one just reaches the critical mass as the pebble flux terminates so no further growth is possible at 8 AU. So outside this range the cores will not develop into gas giants. The highest core mass is achieved when M_{crit} is just reached at the time that the pebble flux is finished, which occurs at 4.8 AU. In addition the extreme cases at 1 and 25 AU can provide interesting insights into the composition differences between larger radial separations. Moreover, the core at 12 AU to bridge the large gap between the inner 8 and 25 AU. The mass evolution of the cores is shown in Figure 6.2.

Here it can be seen that there are several different radii ranges that dictate the evolution path of mass evolution. For $r_c \lesssim 2$ AU the cores reach isolation mass, but this mass is not high enough to trigger rapid gas accretion to form giant atmospheres because it is smaller than $M_{c,crit} = 10 M_{\oplus}$. For radii $2 \lesssim r_c \lesssim 4.8$ AU, cores will reach isolation mass faster than the disk dissipation time scale $\tau_{disk} = 3$ Myr. If $r_c \gtrsim 4.8$ isolation mass is not reached before $\tau_{disk} = 3$ Myr and again no giant atmospheres will form. If the cores reaches $M_{c,crit}$ after τ_{disk} however, there is still gas at a reduced density in the disk that can be accreted. These planets accrete substantially less amounts of gas than what are called gas giants, leading to ice giants Lambrechts *et al.* (2014).

To analyse the composition of the cores, the abundance of the most abundant ices in the cores are shown in Figure 6.3.

Furthermore, in Figure 6.4 the radius of origin for each core for the duration of accretion is shown, to get a better understanding of where the pebbles originated for each core.

The pebble origin lines for each of the cores lie close to each other. This makes it difficult to distinguish between each of the lines, especially for $r_c = 5, 8$ and 12 AU. To verify that calculations are done correctly, it is important to state that none of the lines cross each other. At the start of pebble accretion the origin of the pebbles for all cores lie between 20 and 26 AU, so a range of ~ 6 AU. This spread of radii where the pebbles originate increases over time. By the time pebble flux is halted the range is increased to 20 AU. This means that the material of origin for all core locations lies very close to each other, both in time and in radius.

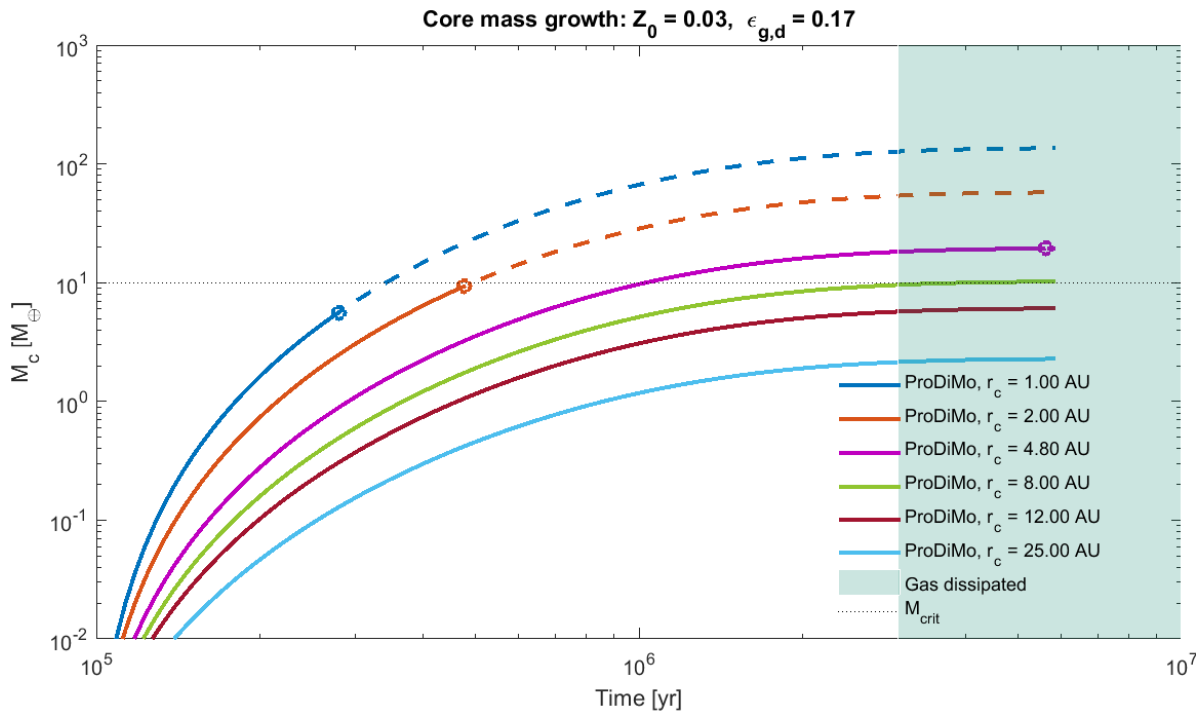


Figure 6.2: Core mass evolution for formation radii specified in the legend. The dashed lines indicate the mass evolution path without pebble isolation. The solid lines are the mass evolution paths of the different cores, and the circles indicate the isolation time and mass if it is reached.

By projecting Figure 6.4 onto each of the species abundances in Figure 6.3, an indication of the abundance variations of each species between the cores can be determined. To be able to easily apply these curves onto the panels and get an indication of the origin of the accreted material, Figure 6.5 shows a scaled version of Figure 6.4. It is concluded that no major abundance changes take place in time or over the radius for the region of the origin material. This also means that the composition of the accreted material does not change from core to core. This is exactly what can be seen in Figure 6.6 on the panels on the left-hand side.

Figure 6.6, shows the compositions for the final core masses. That is either when M_{iso} is reached, or when the pebble mass flux from the outer disk has stopped. The radius of formation, final core mass and the time at which the core is fully formed t_c is shown below each core composition. In addition, Table B.1 a complete list all the species abundances is shown.

To look at the composition in some detail, the dust and ice percentages are shown in the upper left corner of each sub-figure. Each large pie chart shows the chemical composition if the ice present in the core. The left-hand cores are formed with the pebble accretion method, the right-hand cores are formed through planetesimal accretion and will be discussed in Figure 6.1.

Looking at the composition of the cores in Figure 6.6a, c, e, g, i and k, it is seen that indeed the compositions of the cores are very similar to one another. From Figure 6.4 it is seen that by the time the core is introduced to the disk at $t = 10^5$ yr, the pebbles that reach the cores are coming from different locations. In addition it is seen that the cores at 1 and 2 AU stop accreting before the last four cores. This outcome means that the scenario of pebble accretion results in cores with similar compositions. The composition is computed with the assumption that the pebble composition is fixed from the moment it starts to drift away, could have a significant impact on this outcome.

The dominant ice species is H_2O followed by another high percentage of CH_3OH . This outcome shows that the differences in composition between the cores formed at several radii is similar. In all cores almost half of the icy material consists of H_2O , which slightly increases with larger radius.

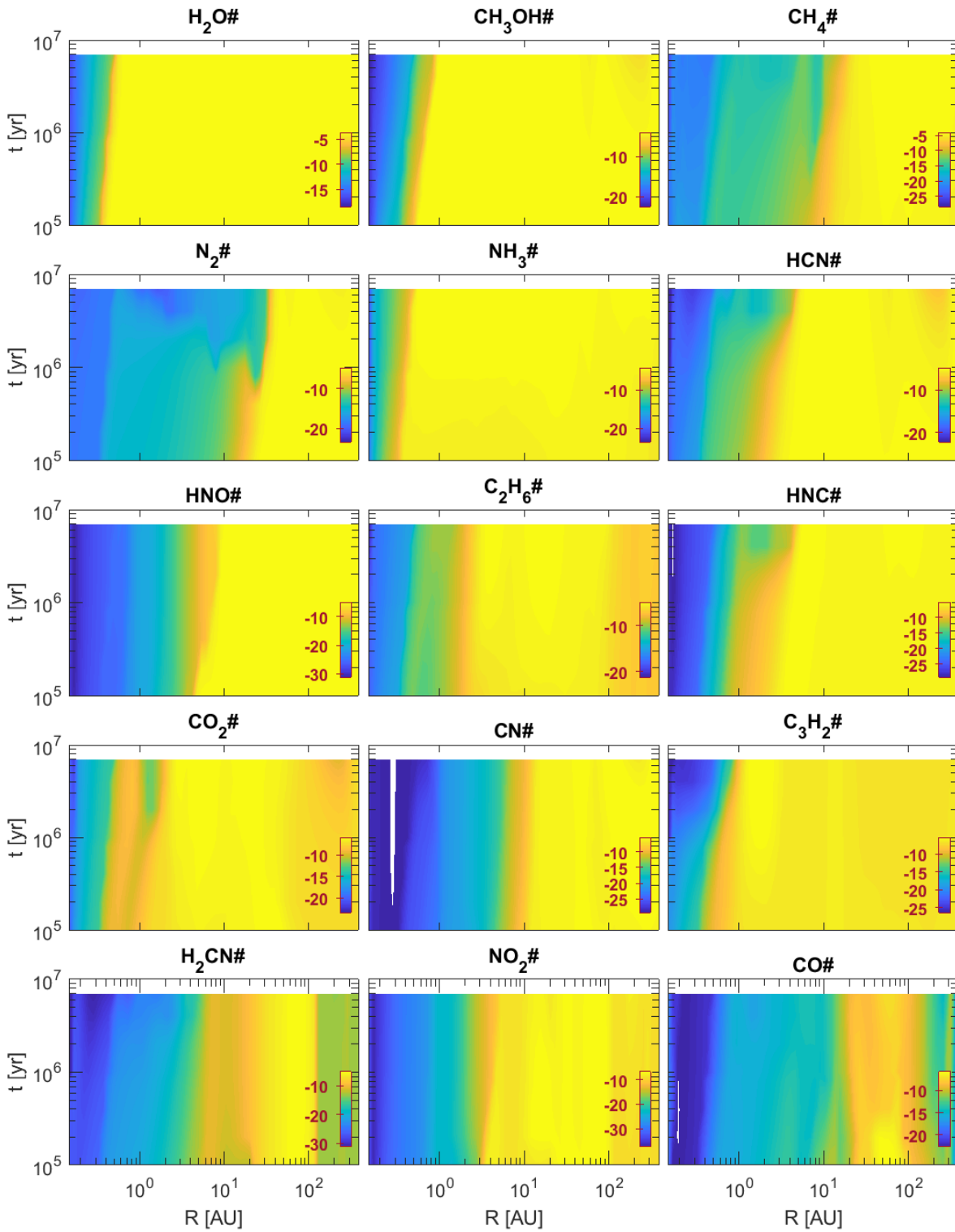


Figure 6.3: Abundance of the columns of the ices represented most in the core formed via pebble accretion. The unit of the colorbar is $\log_{10}(n_x/n_{<H>})$. The red lines indicate the ice-lines of the species.

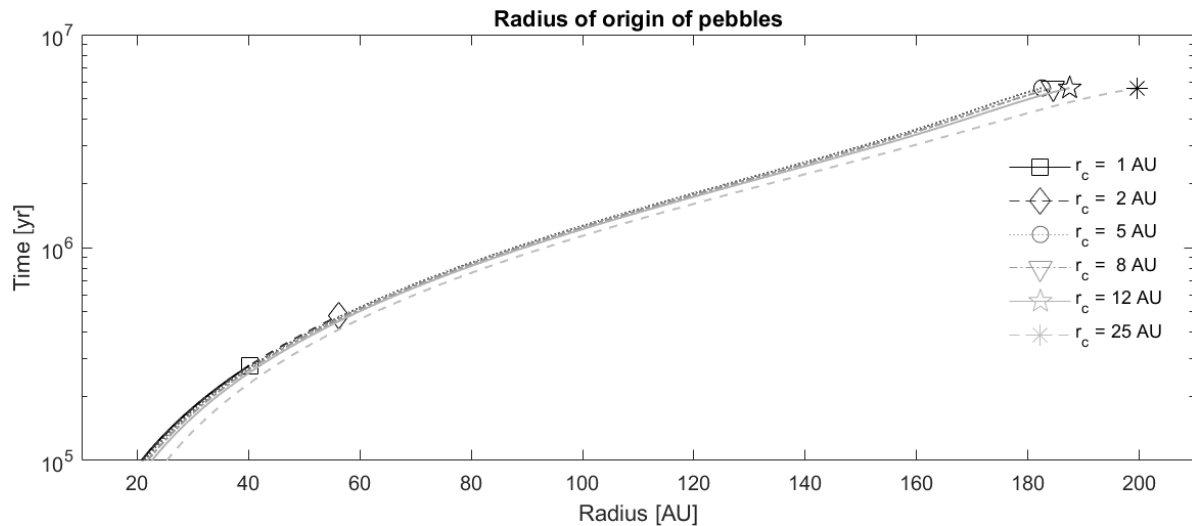


Figure 6.4: Origin of the pebbles accreted as function of radius and time of accretion. The markers indicate where and when the last pebbles to be accreted originate.

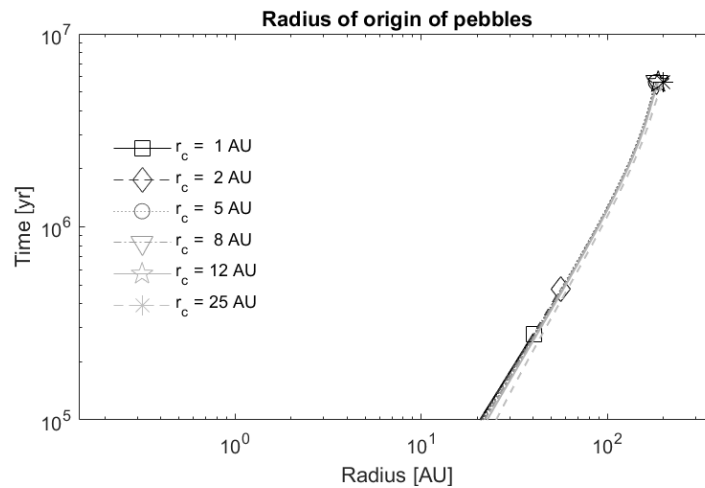


Figure 6.5: Origin of the pebbles accreted as function of radius and time of accretion. The scale is applied so that it can easily be compared to the composition panels in Figure 6.3.

Core composition comparison

The cores formed by pebble accretion are very similar to each other due to the fact that source material originates from the same region; pebbles from the outer disk. In this section these pebble cores are compared to cores that are formed locally via the method of planetesimal accretion.

Methods to simulate the mass evolution of planets via planetesimal accretion are described in Ida and Lin (2004); Cridland *et al.* (2016); Kokubo and Ida (2002). Because the focus of this report is the pebble accretion scenario, a simple method is used to determine the core composition via planetesimal accretion. The composition of the core formed via this local method is simply assumed to be the composition of the mid-plane at the radius of formation; at radii r_c as the pebble accretion method. The decision to take the local composition as the core composition is considered justified because the Hill radii of the cores are small compared to the grid points of ProDiMo. This also means that only the composition can be compared, and not the core mass.

Since no mass evolution of the core is taken into account the duration of the core formation is unknown. This is important because the chemical composition of the disk model does evolve. Taking the chemical composition of a 1 yr old disk will give a different result than the composition at the same location at 10 Myr. For simplicity, once planetesimals have formed it is assumed that the chemical evolution halts. As described in section 3.2, surface chemistry will continue, however in the case of

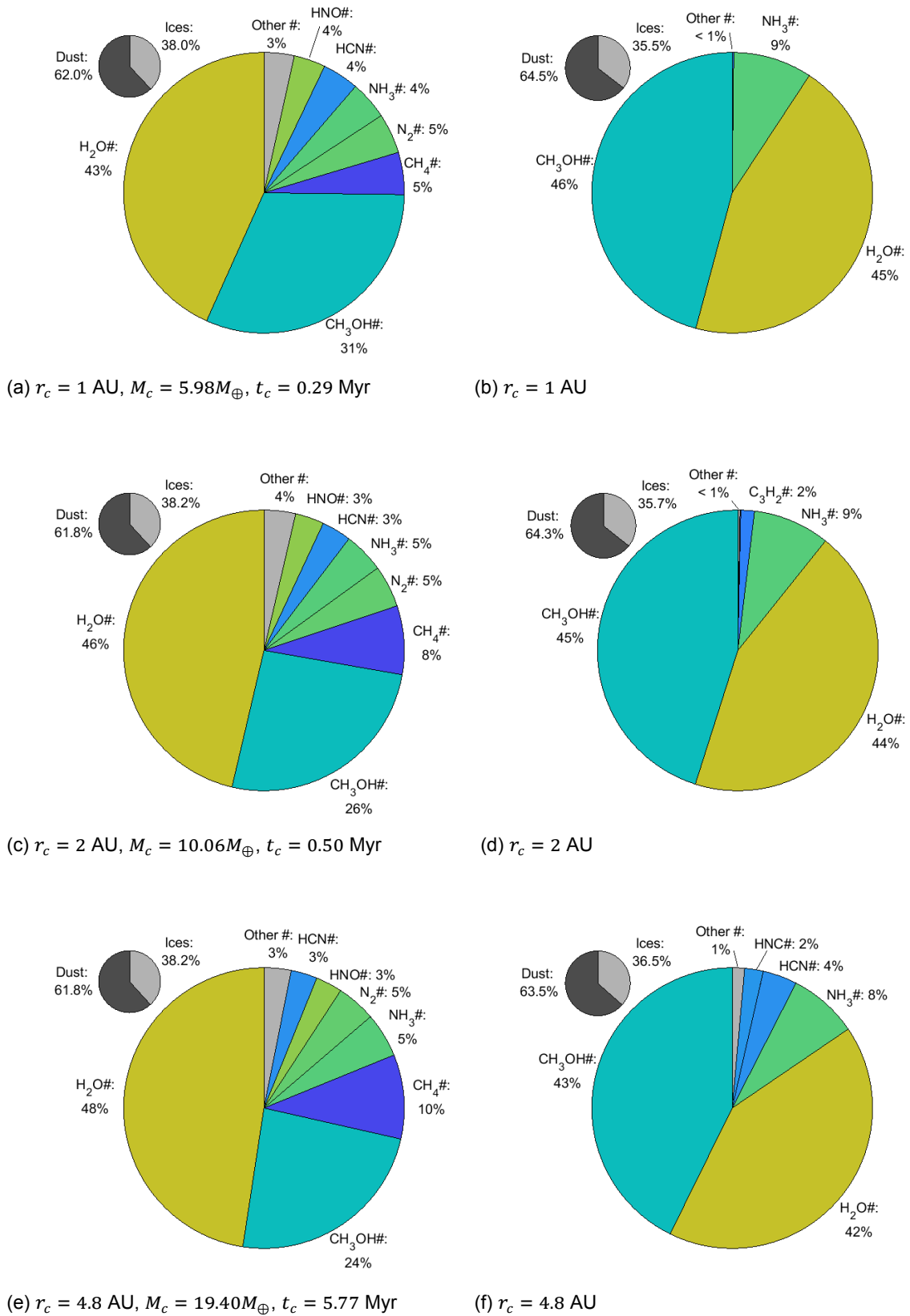


Figure 6.6: Core composition found by the planetesimal accretion scenario for different accretion radii. In the upper left corner dust and ice percentages are shown

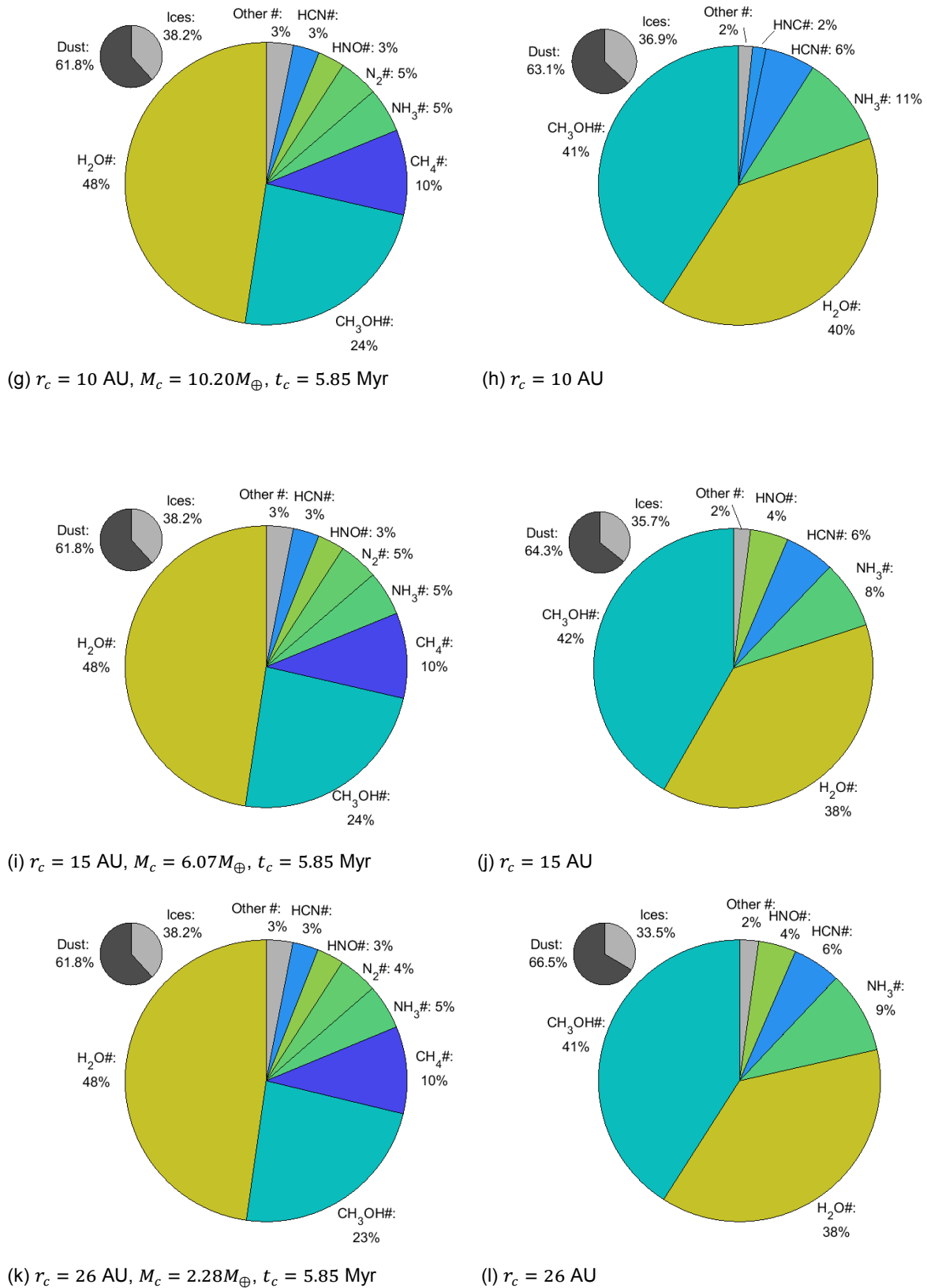


Figure 6.6: Core composition found for the pebble accretion scenario on the left and the planetesimal accretion scenario for different accretion radii. In the upper left corner of each panel the dust and ice percentages of the total core mass are shown. The large pie charts show the mass percentage of the ice in the core.

planetesimals the mass fraction that is chemo-reactive is very small because it is restricted to a thin layer on the surface.

Furthermore, it is assumed that the interior of the planetesimals does not evolve either. So the chemical evolution after planetesimal formation is neglected. This restricts the problem to the determination of the time that the planetesimals are formed. As suggested by Montmerle *et al.* (2006) it is assumed that at $t = 10^6$ yr the planetesimals have formed. So the composition of the solids at $t = 10^6$ is computed for the cores at the same locations as the cores formed by pebble accretion. The results are shown in Figure 6.6 on the right-hand side panels.

Similar to what is found in the pebble cores, the bulk of the ice in the planetesimal cores consists of H_2O and CH_3OH . It is not clearly visible in the H_2O ice plot that beyond ~ 1 AU the abundance decreases slightly, while the other species stay approximately constant or even increase slightly with radius. This explains why the percentage of water decreases from 45% at 1 AU to 38% at 25 AU. It allows the other species to take over some of that percentage. The third most abundant species in the pebble cores, CH_4 making up between 5% and 10% of the ice mass, but here it is barely present. This is explained with the CH_4 abundance plot. There it is visible that ice only starts to form beyond ~ 20 AU. The ice-line itself, beyond which more than half of the species is present in ice form, is located at an even higher radius. Since all of the cores formed inside of this radius, they will not get a chance to accrete CH_4 ices. The most important difference from the pebble cores is that the location of formation changes the composition more in pebble cores.

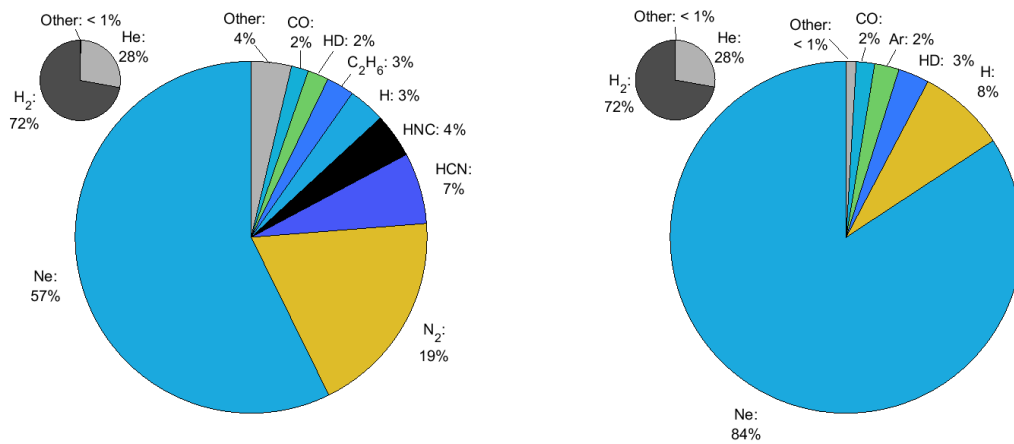
6.2. Atmosphere composition

If a core has formed and the mass has reached $M_{c,crit}$ the core may also accrete massive amounts of gas to form a gas giant as described in section 5.3. The composition of this accreted gaseous atmosphere is calculated by the same technique as used for the mass. The difference is that the mass of each element is determined with the surface density of each individual species as shown in Equation 6.4. Again, the surface density is only known at discrete radii, so the trapezoidal technique is used to evaluate the integral numerically as shown in Equation 6.5.

$$M_{x,gas} = 2\pi \int_{r_c-r_H}^{r_c+r_H} \Sigma_{x,gas} r dr \quad (6.4)$$

$$\approx 2\pi \sum_{j=1}^n \frac{\Sigma_{x,gas}(r_{j-1})r_{j-1} + \Sigma_{x,gas}(r_j)r_j}{2} \Delta r_j \quad (6.5)$$

The resulting gas compositions are shown in Figure 6.7. The complete list of gas percentages is shown in Table B.2.



(a) $r_c = 2$ AU, $M_c = 10.1 M_{\oplus}$, $M_p = 65.8 M_{\oplus}$ (Figure 6.6c), 0.23% of the total atmospheric mass (Fig-ure 6.6e), 0.15% of the total atmospheric mass

(c) $r_c = 8$ AU, $M_c = 10.2 M_{\oplus}$, $M_p = 27.6 M_{\oplus}$ (Fig-ure 6.6g), 0.16% of the total atmospheric mass

Figure 6.7: Gas compositions of the formed giant planets.

As expected the atmospheres are dominated by H_2 and He, so the scale of these species compared to the other species is shown in the left upper corner of each panel. The composition of the remaining species of the atmosphere is shown in the large pie charts.

Here it stands out that the most abundant species by far for all of the atmospheres is Ne. This is due to the fact that in ProDiMo there are no reactions or phase changes defined involving Neon other than ionisation. The same holds for Helium and Argon. This means that these 3 elements stay constant relative to each other throughout the disk and over time. The reason that the share of Ne increases is the freeze out of the gasses. The forming ices reduce the amount of gas, but the amount of Neon gas stays the same, and thus increasing the percentage of Neon. This also happens with Argon as can be noticed by the presence of Argon only in the outer two cores.

Besides the huge difference of Neon, there are a few more significant differences between the cores. Especially between the core at 2 AU and the outer 2 cores. N_2 for example, this gas has a share of a fifth in at 2 AU, but at 4 AU already its share has dropped to less than 1%. To analyse this, the gas composition of the gas species most abundant in the atmosphere are given in Figure 6.8. Here it is seen that in the first subplot N_2 is shown. Looking at the locations of formation of the planets and the time at which they form, it is seen that the amount of N_2 is sensitive to both time and location, especially around 1 Myr. By looking carefully at the plot it is concluded that the 2 AU planet lies just within the region of high N_2 abundance and the outer two planets lie just outside of it. The disappearance of HCN, HNC and C_2H_6 have an explanation similar to the N_2 . But to a lesser degree due to the overall lower abundances. And C_2H_6 is not so sensitive over time. Lastly, the amounts of CO, HD, and H stay steady because they have only minor fluctuations over time and spatially. In addition it should be noted that all of the planets here form beyond the water ice-line. Which means that

6.3. C/O ratio of the atmosphere

One way to characterise the atmosphere of gas giants is to list the abundances of all species. However, even if the species do not evolve significantly during the accretion process, over time the atmospheres will undergo environmental changes due to the stellar and interstellar radiation variations. Moreover, the extreme pressure and temperatures inside the atmosphere lead to conditions for chemical activity. So over millions of years the chemical composition is unlikely stay the same. Assuming that there is no material leaving or entering the planet atmosphere, the chemical species change, but the elemental abundances will remain constant. In order to link the formation of gas giants to their composition, instead of looking at the individual species, the elemental abundances are investigated. Over 99% of the elements of gas giants consists of H and He, just like the universal abundances. The interesting information is in the <1% of the gas other than these two bulk elements. The number fraction of elements relative to elemental H is called the metallicity.

The third and fourth most abundant species are C and O. Moreover, species like CO, CO₂, CH₄ and H₂O also have the most accessible spectral signatures making them the most observed species in both gas giants and PPDs. So the C/O ratio, or simply C/O, is a widely used to link the gas giant's atmosphere to the formation scenario and location of origin. Therefore the C/O is computed for the disk and the atmospheres that are formed in section 6.2. This is done using a the abundance of the C atoms of all species $n_{<C>}$. Then the same is done for the O atoms, $n_{<O>}$ after which the C/O (number) ratio $n_{<C>}/n_{<O>}$ is found. The results of both the atmosphere and the planets are shown in Figure 6.9.

The dotted light grey to black lines are the C/O of the gas in the disk. The C/O of the atmospheres is shown in the red, where the horizontal bars are used to indicate the size of the Hill radius to see the range of C/O that the atmosphere consists of. In addition the three atmospheres that are formed in section 6.2 are highlighted by the black circles. Since the star and the disk formed from the same region in the MC, the assumption is made that the star and the disk have the same composition. So the stellar C/O in Figure 6.9 is equivalent to the disk C/O.

The C/O shows high values between 0.5 and ~ 4.8 AU. These values go up to 140. This means that the gas is strongly depleted of O-bearing molecules. The cause for this can be found in the ice-lines as shown in Figure 6.10. The major ice-lines, the ones with highest abundances, are shown in red as indicated by the legend. From this is visible that indeed the spike is caused by a depletion of O-bearing gasses due to the water ice-line. The most abundant O-rich species H₂O and CO₂ start to freeze out at a radius of about 0.6 AU. This is leaving the gas with most of the carbon until the HCN and HNC ice-lines which are located at about 4.8 AU. Between these two ice-lines the C/O is very high, with two peaks. The cause for this can be seen in the HCN and HNC ice abundance plots in Figure 6.3. Outside of this range the C/O tends to the global or stellar value of 0.46, meaning that the gas is depleted of equal fractions of C- and O- bearing species. The C/O of the atmospheres of the planets are in good agreement with the local gas disk at the time of formation. This is due to the fact that the atmosphere is accreted locally. Moreover, the Hill radii are not large enough to span regions with significantly variable C/O. So the assumption that the C/O of a gas giant atmosphere is equal to the gas disk works well here.

6.3.1. C/O of the cores

As stated above, the atmospheric C/O will remain constant over time given that no species have the opportunity to enter or leave the atmosphere. Up to now the core and the atmosphere are considered to be have strictly separate compositions. However, the core has a reservoir of species that are assumed in ice phase at the time of accretion. During and after acquiring the atmosphere the pressure and temperature of the core reach very high values due to the high mass of the gas giant. Under the condition that these species are not trapped deep inside the core, these species can out-gas from the core into the atmosphere. By dissolving the core species into the atmosphere, the C/O can also be affected if it is different from the atmosphere's.

To analyse what happens if the core ices enrich the atmosphere with metals, i.e. species other than H and He, the C/O of the ices are shown in Figure 6.11. The increasingly dark dotted blue lines are the overall C/O of the ice in the disk. Only the line for 1 Myr is solid because this is the time at which the planetesimals are assumed to form.

From the inner radius the up to about 1 AU the C/O is almost zero. This is due to the fact that molecules such as H₂O and SO₂ already have a small fraction of ices while the C-rich molecules

freeze at lower temperatures, so in this region species like CH_4 have no ices whatsoever. This is a consequence of a numerical code. Analysis of this part of the curve leads to the conclusion that no ices are expected in this region whatsoever. So this section of the curve can be interpreted as 'no ice'. Ice-lines or ice-lines are usually defined in as a radius at which the ice species freezes. Since ProDiMo computes whether ices form not just based on the temperature, there is no line dividing the disk into a part with just the gaseous species and another with only ice. Instead there is a gradual transition from the gaseous phase to the solid phase. This means that another way to define the ice-lines must be introduced. In this case the ice-line will be defined as the smallest radius at which the ice and the gas of the species are equal. This also means that the ice-lines are not necessarily close to the region where the increase in ice is directly visible since it could take a large distance from where half of the species is frozen to reach disk conditions that are ideal for the ice species.

Beyond 1 AU, CO_2 and CO also start to freeze out as can be seen from Figure 6.3. This leads to an increase in the C/O. Moreover, the radius at which this increase is seen shifts outward. This corresponds to the H_2O and CH_3OH ice-lines as shown in Figure 6.10, that move outward over time due to the increasing temperature in the disk. Note the increasing level at the top of the figure around 2 AU. This is due to the increase of CO_2 over time starting from 1 Myr.

From about 5 AU, especially in the dense mid-plane, the disk becomes very cold so that the C-bearing species HCN, HNC, CH_4 freeze out in large quantities. From here on the C/O in the ice remains approximately stellar. In the far regions of the disk interstellar radiation affects the C/O to a small extent. However, since neither the pebble cores or the planetesimal cores are made from this material, this region is not of interest.

As seen in Figure 6.4 the pebbles for the pebble cores are made of material that originates roughly between 20 and 200 AU. So the C/O of the core should and does reflect this. The fact that the C/O is approximately equal for all formation radii could have been concluded from the fact that the composition of all of the cores does not change significantly.

The planetesimal cores follow the C/O of the solid disk almost exactly, because the C/O of the planetesimal cores is in this case defined as the local one. This can be seen as the red squares in Figure 6.11. The slight elevation with respect to the C/O at 1 Myr here, is due to the fact that planetesimals consist of local material. So from the disk mid-plane, while the disk C/O here is calculated for the columns of gas parallel to the radial direction. In the mid-plane the disk is colder, so that the C-bearing species can join the O-bearing species in the solid phase.

6.3.2. Tracing atmospheres to location of formation

To link the C/O of a given gas giant to a location in the disk, it is important that the disk produces atmospheres with a C/O that varies with location. Fortunately this is the case as seen in Figure 6.9. Any location in the disk will result in super-stellar C/O, but differences from location to location are quite high. Considering no contamination from the core ice species, planets with with C/O >10 will have formed in the very inner disk between 2 and 3 AU. Then there is a region from 3 to 5 AU where the C/O declines rapidly, which means that the atmosphere composition is very sensitive to the radius of formation. This sensitivity is very useful to link the composition to the formation.

By taking into account that the ices of the core can evaporate and enter the atmosphere, it is found that if ice species of the core are mixed into the atmosphere, the atmosphere's C/O can only be decreased. In the extreme case the core ices are completely mixed into the atmosphere.

For the planetesimal formation this means it is equal to the disk or stellar C/O. That is, if the planet formed from the total gas and ice mass of a radial range. Both the core and the gas are formed from the same vertical column. As explained in chapter 3, ProDiMo does not consider radial exchange of material which leads to fixed abundances of each element at all radii. So if a planet is completely formed from local material, the C/O will be the same as for the star. However, it is very unlikely that all of the ices end up in the core of the gas giant. So it will depend on the mass ratio of the core and the atmosphere. Since the core mass is not calculated for planetesimal formation, the M_c from the pebble accretion scenario is used. The planetesimal core is formed from mid-plane material only, since the mid-plane has the lowest temperature, a small excess in C/O is observed with respect to the column C/O at the same time. This can be seen in Figure 6.11 as the small deviation of the red squares from the solid blue line. The effect this has on the planetesimal cores is not computed and shown as the magenta squares in Figure 6.13.

The C/O of the original atmosphere without any core ices is represented by the black line with

asterisks. In addition the atmospheres mixed with the ices from the pebble cores are plotted as the blue triangles. The addition of core ices into the atmospheres is not very effective, even when the ices contribute a C/O of 0. This is due to the relatively small mass of the core ices the core mass fractions are shown in Figure 6.14. As expected outside of the region where gas accretion takes place, the core mass fraction is 1. Between 2 and 4 AU the values are ~ 0.14 . From 4 to 4.8 AU it rapidly increases to a value of 0.52. And finally it steadily declines to 0.27 at 8 AU.

The ices are approximately 38% of M_c as seen in Figure 6.6, so the effect is only a small reduction of the C/O. In the very inner disk region up to about 4.8 AU, the C/O takes on values between 2.2 and 13. From 4.8 AU the C/O gradually decreases from 2.2. to about 2.3. The validity of these results is discussed in chapter 7.

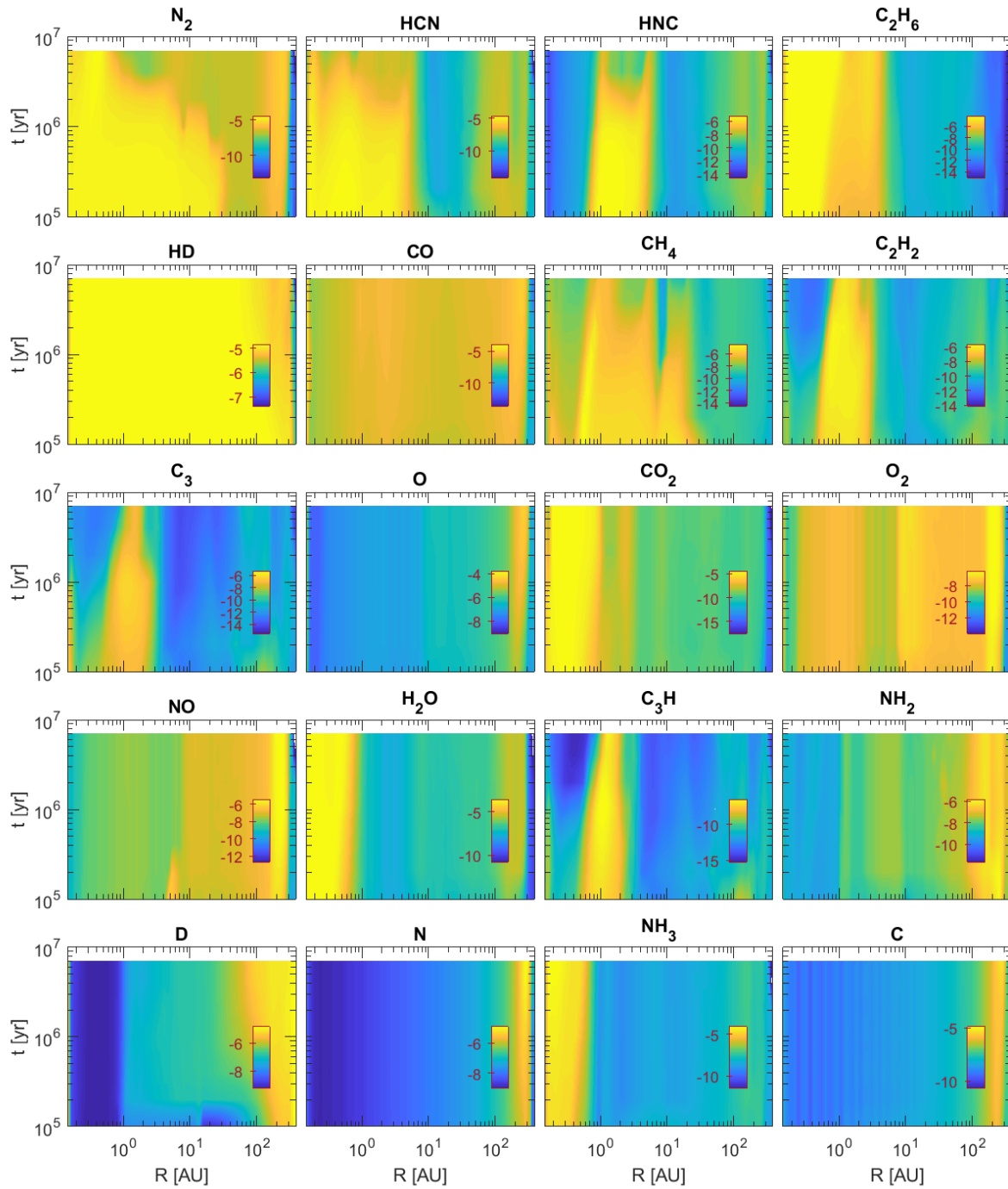


Figure 6.8: Column density evolution of the species most common in the atmospheres shown in Figure 6.7a.

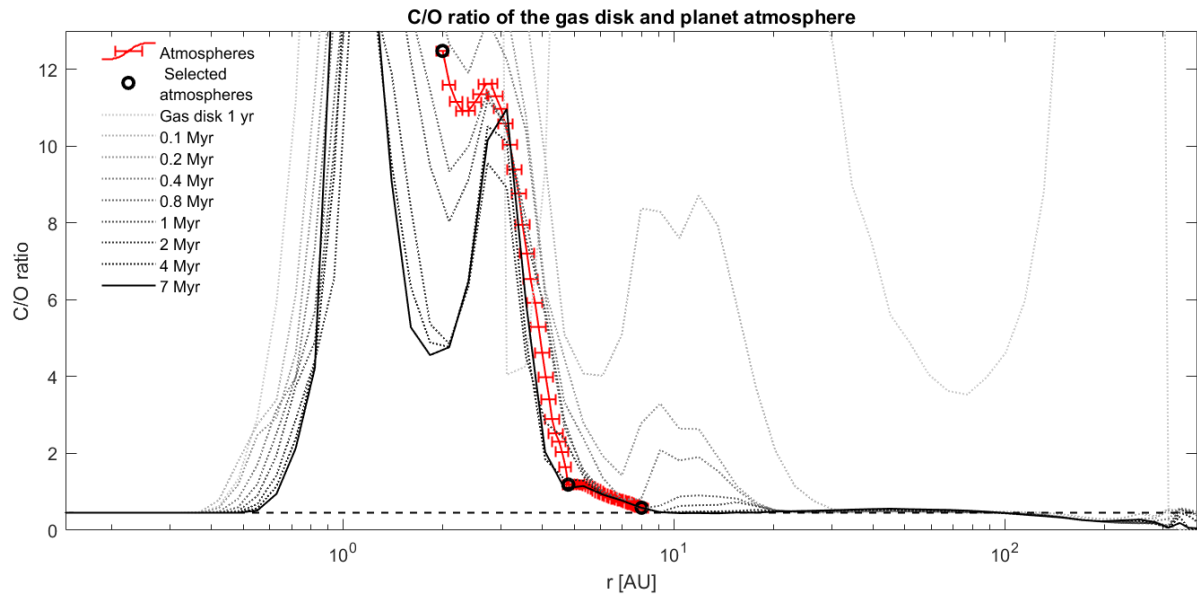


Figure 6.9: C/O of the disk gas over the total disk height and the atmospheres of the formed gas giants.

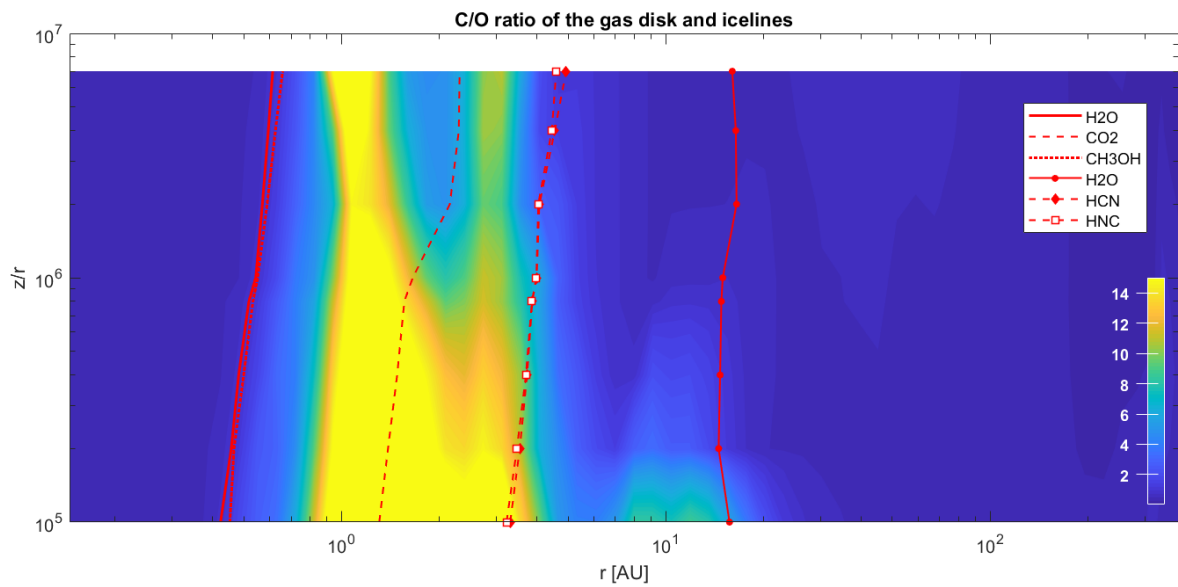


Figure 6.10: C/O of the total disk height in the gas as function of time and radial distance. The colour is scaled up to 15, so the bright yellow region is means that the C/O is 15 or higher (also see Figure 6.9).

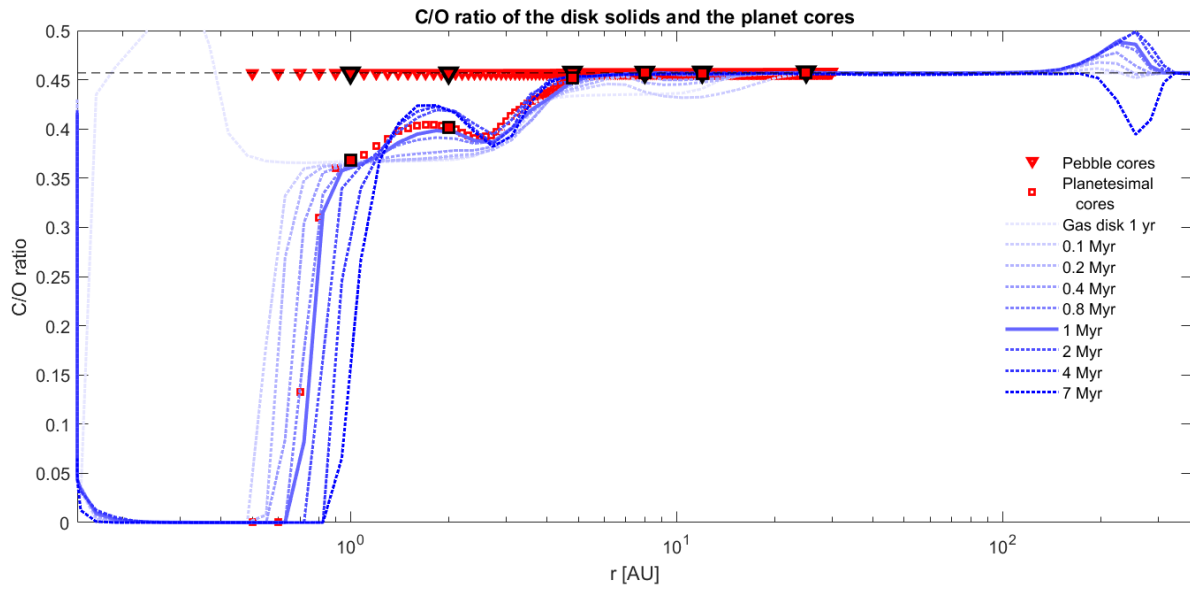


Figure 6.11: C/O of the total disk height in the ice is shown as the dotted and solid lines from light blue to dark blue, the cores formed via pebble accretion indicated by red triangles and the planetesimal cores as red squares. The selected core formation locations are indicated by a black edge of the mark.

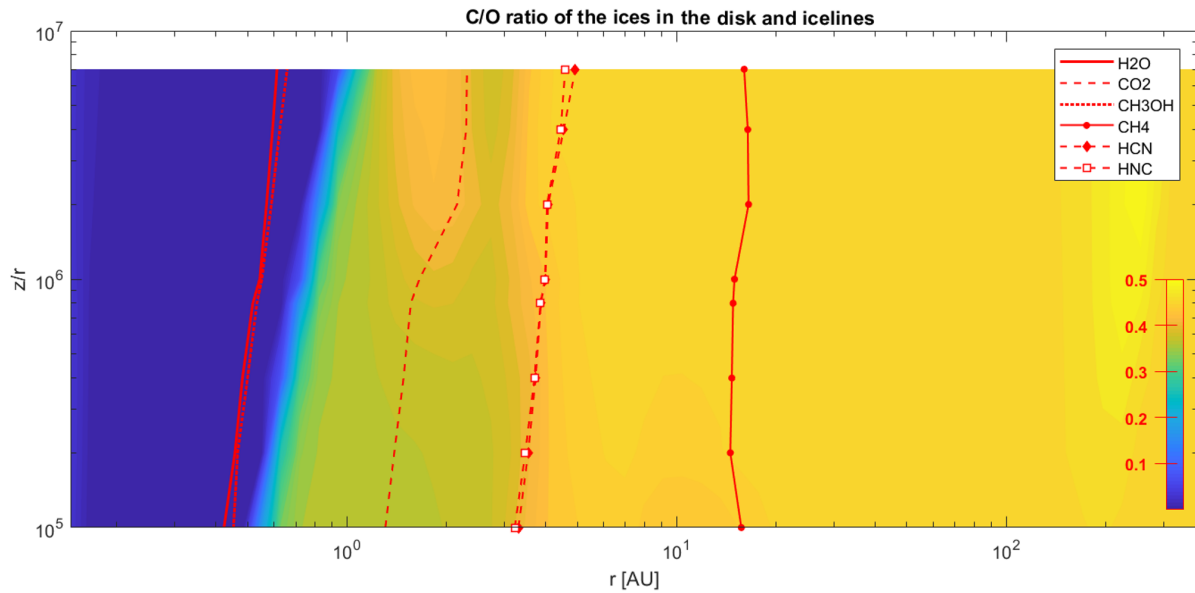


Figure 6.12: C/O in the disk ices as function of time and radial distance.

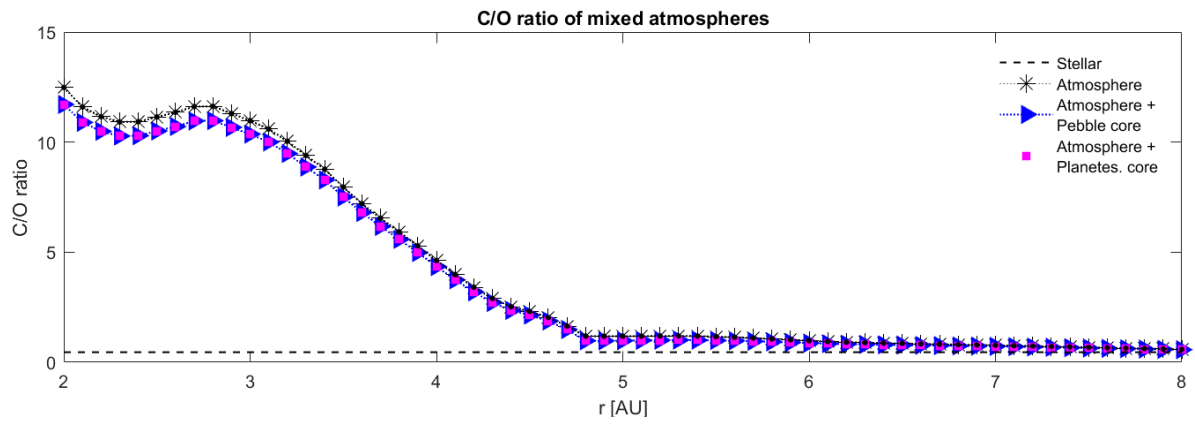


Figure 6.13: C/O of the atmospheres with and without core ices dissolved into the atmosphere.

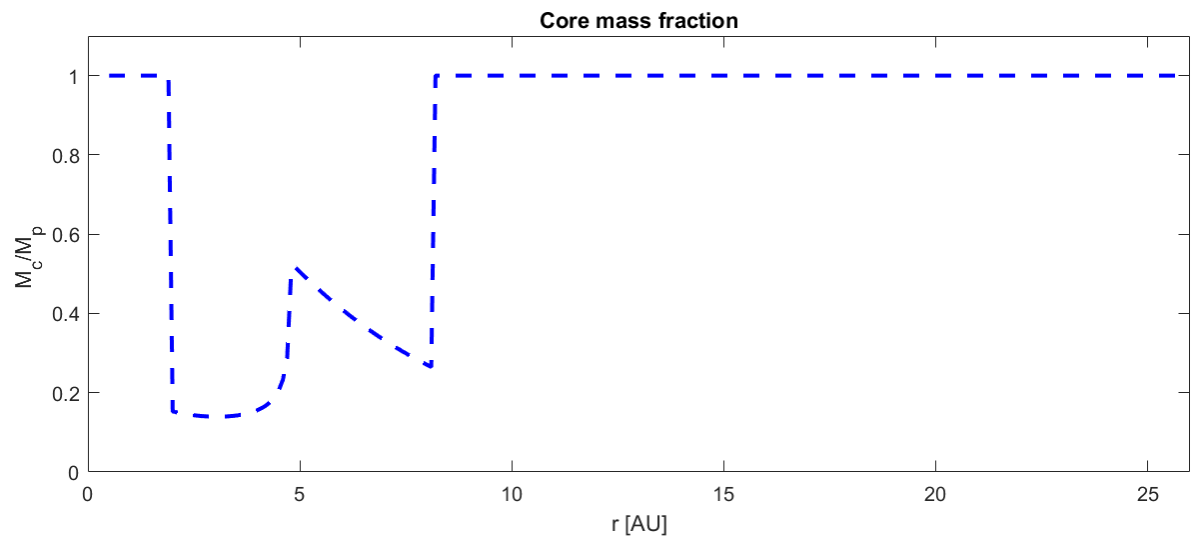


Figure 6.14: Core mass fraction of the total planet mass.

7

Discussion

The results presented in chapter 5 and 6 can not be taken as fact. Unfortunately, to comprehensively model the disk, the core and atmosphere masses and composition, many assumptions and simplifications are made. This causes the results to be inaccurate. In this chapter, the most important assumptions and simplifications are addressed. Additionally, an indication of the possible effects of the assumptions is given where possible. Firstly the disk model AA Tau from ProDiMo is treated. Then the core accretion model and the adjustments made to enable application to the ProDiMo model are addressed. Lastly the composition of the core and atmospheric C/O ratio are discussed.

7.1. Composition

The composition provided by ProDiMo has a relatively complex chemical model in comparison to other studies. The 242 chemical species and the chemical network of over 8000 reactions, allows the chemical composition of the disk and later formed planets to be very detailed. The species included are either observed or expected to be present in the disk or have an impact on the disk chemistry.

ProDiMo is developed in the first place to make synthetic SEDs of the PPDs. Therefore, up to recently, time dependency was not high on the agenda of the development of ProDiMo. So, the code is not necessarily suited for making planets that are formed in time-dependent environments. The assumption that the disk density decays exponentially in chapter 5, is only part of the solution. The most important issue of ProDiMo for time-dependent proposes is this disk structure. The disk structure is a very important aspect that influences the radiation field. In turn the radiation field is responsible for the temperature and chemical reactions. By just reducing the density, the self-consistent temperature and chemistry is violated. In addition the dust grain size range is expected to shift from small particles to large particles. The effects of this are seen in section 4.1. All in all, the compositions computed by ProDiMo will be different from a consistent solution with the new decayed structure with different dust grain sizes.

The ice on the dust particles is considered to have a fixed composition from the moment it has reached pebble size. In reality, the composition of the ice will change. Depending on how long and how far the pebbles have to travel before they are accreted by the cores, the pebbles will encounter different conditions from where they formed. The temperature and the radiation environment can have significant effects on the species. Moreover, gasses on the drift path of the pebbles can freeze out on top of the pebbles. The impact of this assumption is unknown, so the results of the core compositions should be taken with care, because the contributions of the elemental abundances of C and O could also change due to this assumption.

Furthermore, due to the heat of the accretion impacts of pebbles on the core, the ices on the pebbles sublime and develop a gaseous envelope. This means that the ices encounter a new environment with conditions that affects the chemistry. So the core composition as presented in chapter 6 is probably not exactly what would be the case if these reactions are taken into account. However, unlike the chemical changes during the drift phase, this will not have an impact on the C/O ratio because the elements are conserved on in the system. It may play a role in the level of core ice mixing into the atmosphere.

7.2. Pebble accretion model

As seen in chapter 5, the pebble cores do not grow beyond 5.85 Myr. This is due to the fact that the mass accretion rate is dependent on the pebble flux M_{peb} . The pebble flux is conserved throughout the disk interior to the pebble production line, so at the production line reaches the outer edge of the disk the pebble flux throughout the entire disk becomes $M_{peb} = 0$. This would mean the pebble distribution stays fixed from that time, which is very unlikely. Moreover, it is not difficult to imagine that this condition is violated in real disks due to gaps, or overdensities in the density profile. So objectively, this conservation condition can be a good first approximation of the pebble flux, but is not necessarily accurate.

In section 5.2 it is explained that in order to get a gas giant forming disk, some of the models parameters have to be adjusted. Lambrechts *et al.* (2014) do state that this method to form planets requires a disk of a significant radial extent. No minimum is given, but it is suggested that disks with observed outer radii of ~ 210 AU would be sufficient. Since AA Tau has an outer radius of 382 AU this should not give any problems. Looking more carefully at the disk surface density, it is noted that the taper radius, where the surface density starts to reduce with respect to the exponential surface density, is located at 50 AU. Assuming the surface density of this disk is parametrized as in Equation 5.6, the density structure of ProDiMo is only of comparable density up to 50 AU. So it could be argued that the AA Tau disk does not have the radial extent that the method requires.

7.3. Discussion of the C/O ratios

The results are compared to two other studies that try to find a connection between the C/O and the formation path through modelling. Firstly, Cridland *et al.* (2019) conducted a similar study by combining a chemical disk model and a gas giant formation model. In that study, the formation model that is investigated thoroughly is also a core accretion scenario but with planetesimals instead of pebbles. The chemical model that is used there is taken from Eistrup *et al.* (2018). This model is similar to ProDiMo but uses a less extensive chemical model, with a smaller chemical network, i.e. less species and less types of reactions, and a simple temperature profile. Moreover, only the disk mid-plane is considered. The time dependency of the structure is more sophisticated, as the volume density in the mid-plane is determined based on the disk evolution. Whereas in ProDiMo the structure is considered to be fixed and only after the compositions at different times is computed, a power law is applied to account for disk dissipation. In addition the inner disk material is assumed to be accreted by the star from the inner edge of the disk. The formation method Cridland *et al.* (2019) used is taken from Cridland *et al.* (2017), which is based on Ida and Lin (2004). In this formation model, not only is the mass of the planet evolving, but also the orbital radius of the planet evolves. This results in a migration path of the planets, carrying them through different gas composition environments during mass accretion.

Even though the study is similar, the disk parameters such as the disk and star masses are not exactly the same because . But since the majority of the atmospheres of both studies comes from similar regions, the fact that the accretion scenarios are different does not have a major effect on the C/O. So the relative result can be compared; whether the C/O is sub-stellar, stellar or super-stellar. Cridland *et al.* (2019) finds that the C/O in the planets formed between 1 and 3 AU can have super-stellar C/O, but only up to the value of ~ 0.7 , while stellar is assumed 0.54, so a slight C-enrichment of 1.3 with respect to stellar. The majority of the planets however, result in sub-stellar C/O. To compare this to the C/O of the atmospheres of section 6.3, the atmospheric C/O relative to the stellar C/O, $(C/O)_{planet}/(C/O)_{stellar}$, is shown in Figure 7.1. Comparing this C/O to the C/O found by Cridland *et al.* (2017), the values of the formation at radii up to 4.8 AU, between 2.1 and 28, considered are extremely high. This excessive C/O is traced back to the depletion of O-bearing between the O-rich ice-lines and the C-rich ice-lines as explained in section 6.3. Beyond 4.8 AU the value decreased from 2.1 to 1.3 which are considered reasonably in line with Cridland *et al.* (2017).

Another similar study is conducted by Madhusudhan *et al.* (2016b). The chemical model that is used is described in section 4.2. The only species considered to affect the C/O are CO, CO₂ and H₂O. The chemistry and time-dependency is accounted for by the temperature reduction due to cooling of the disk over time. Moreover, besides the change of phase of the species, no chemical evolution is considered. Just like in this report, the formation method used is the pebble accretion scenario. However, migration of the planets during formation is also considered. The hot Jupiters in Madhusudhan

et al. (2016b) originate between 4 and 12 AU and migrate inward to an orbital radius of 0.1 AU. This is considered to be comparable to the range between 2 and 8 AU considered in this report. The resulting C/O of these gas giants are predicted around ~ 0.7 ; between 0.64 and 0.76 with a stellar value of 0.54, or $(C/O)_{planet}/(C/O)_{stellar}$ of 1.2-1.4. So again, the results produced in this thesis seem excessively high for the planets up to 4.8 AU.

A third way to qualify the results from section 6.3 is to compare it to actually observed giant exoplanets. As explained in chapter 2, by spectral observations of exoplanets the C/O can be estimated. However, with current observations, only for hot Jupiters the measured C/O can be obtained reliably. This is because their atmospheres are considered well mixed due to the highly irradiated atmospheres by their host stars. Gas giants observed farther out in the disk have colder atmospheres allowing for condensation or cloud formation of species in the atmosphere. These clouds are made of condensate of the gas phase molecules which are on layers in the atmosphere that cannot be observed by current instruments. To determine the elemental C/O of cold Jupiters, atmospheric models have to be applied. Modelling the atmosphere is also a very complex issue, so it brings its own uncertainties.

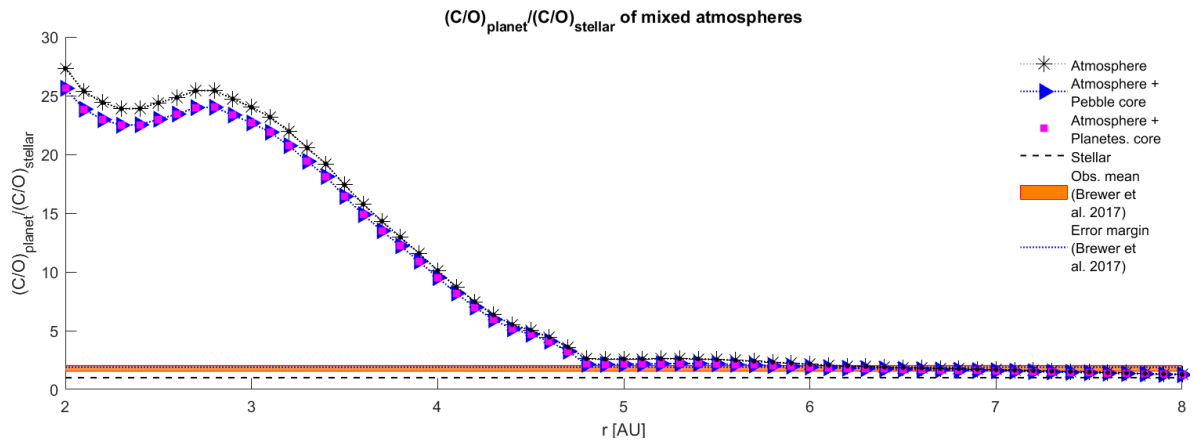
Gas giants are considered hot Jupiters only when their orbital radius is very small, with orbital periods from less than day up to several days. Since it is not possible that the hot Jupiters formed in situ, they must have formed farther out in the disk. Furthermore, as shown in chapter 5, with the pebble accretion scenario no gas giants can form at radii smaller than 2 AU. So in order to compare the observations to the results in Figure 6.13, it must be assumed that the complete or majority of the atmosphere is accreted in the region of the indicated location of formation. After this the planet migrated inward to acquire a stable orbital period in the order of days.

Brewer *et al.* (2017) presents the atmospheric C/O relative to their respective stellar C/O of a selection of hot Jupiters. The mean of their values is $1.9^{+0.14}_{-0.35}$ and shown in Figure 7.1. Comparing the observations to the atmospheric C/O according to section 6.3, observed planets with $(C/O)_{planet}/(C/O)_{stellar}$ between 2.2 and 1.3 for the cores could have formed at an orbital radius between 4.8 and 8 AU. But the values of the atmospheres between 2 and 4.8 AU are once more excessively high in comparison to the observed hot Jupiters, between 2.2 and 28 for the pure atmospheres and between 2.1 and 26 for the mixed atmospheres.

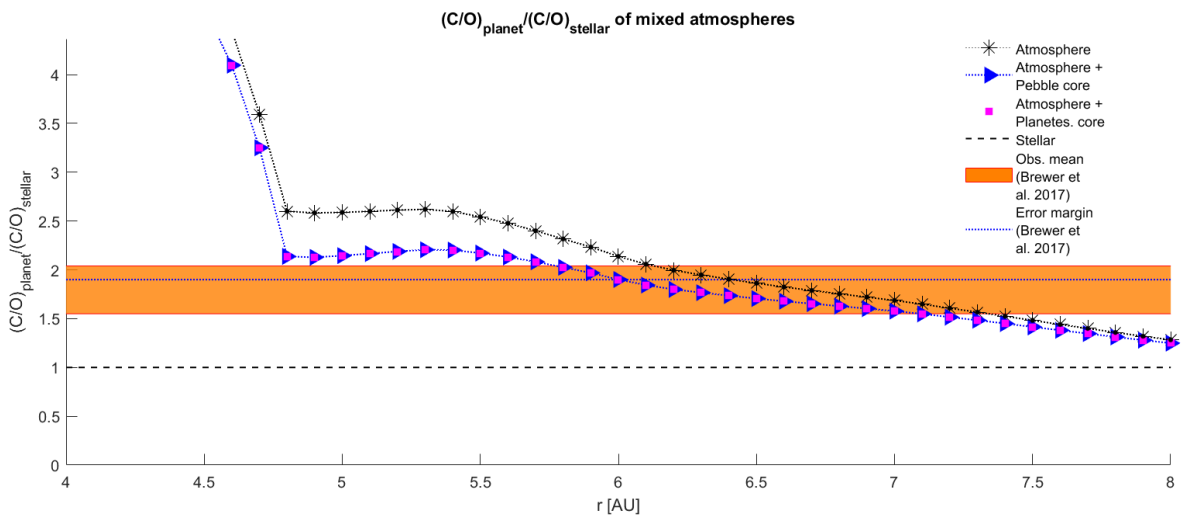
Considering that the results of the model between 2 and 4.8 AU do not correspond to any of the observations, some suggestions for the cause of this are presented:

- The observed hot Jupiters from Brewer *et al.* (2017) are formed between 5.8 and 7 AU after which they migrated inward where they became a hot Jupiter.
- The atmosphere that is observed is not the original atmosphere that it accreted in the first few million years. Icy bodies with O-rich volatiles from further out in the disk were accreted by the atmosphere after formation.
- The C/O ration provided by ProDiMo is inaccurate.

To determine which of these suggestions are the actual cause, further investigation is required.

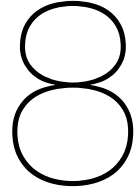


(a) Full range of atmospheres.



(b) Selected range of atmosphere, between 4 and 8 AU.

Figure 7.1: $(C/O)_{\text{planet}}/(C/O)_{\text{stellar}}$ of the atmospheres. The black dotted line with asterisks represents the isolated atmosphere, the blue triangles are the atmosphere mixed with the ices of the core formed from pebble accretion, the atmosphere mixed with the planetesimal core ices is shown as the magenta squares. In addition the mean of the observed values from Brewer *et al.* (2017) is given as the blue dotted line, with the error margins as the orange areas.



Conclusions and Recommendations

Now that all the research questions are addressed and answered in the previous chapters, a concluding chapter is due. The main research question was: *How can ProDiMo be used to investigate the formation pathways of hot Jupiters through composition analysis?*. This question was addressed in 4 stages. First, options of ProDiMo were explored and analysed by comparing it to simple disk models. From this it was found that an observed disk with its data fitted to ProDiMo gives the most realistic disk. One of the ProDiMo disk models that were fitted to observations was chosen to model disk formation. Furthermore, time-dependency and surface chemistry options must also be switched on.

Second, the core formation scenario through pebble accretion was explored, first with the original disk model. For the ProDiMo model it was found that several adjustments are necessary to generate cores that can produce gas giants; the dust to gas ratio has to be higher, and the disk structure has to be modified by reducing surface density over time. Furthermore, there is a delicate balance between the dust to gas ratio Z_0 and the dust coagulation efficiency $\epsilon_{g,d}$. These two parameters must be chosen such that the pebble production is not too fast and not too slow. Both are detrimental to the formation of cores that can acquire a giant gaseous atmosphere.

With $Z_0 = 0.03$ and $\epsilon_{g,d} = 0.17$, cores from the ProDiMo model AA Tau can grow up to $20 M_{\oplus}$. Once formed, the pebble cores are very similar in composition. This is a result of exclusively accreting pebbles from the outer disk. Moreover, the C/O ratio of the core ices is always practically stellar. This is due to the fact that origin of the material lies beyond most of the ice-lines, where almost all of the volatiles are in ice phase. Between 2 and 8 AU the cores grow large enough to accrete a giant atmosphere as well. The total mass of these planets varies between 36 and $110 M_{\oplus}$.

The C/O ratio of the gas giants varies significantly with radius. From 2 up to 4.8 AU the $(C/O)_{planet}/(C/O)_{stellar}$ varies between 26 and 2.1. This would suggest that locating the radius of formation of an observed planet can be very precise. However, gas giants are not observed to have C/O as high as 28 times the stellar value. So to determine a connection between the location of formation and the composition further investigation is required. This leads to a set of recommendations:

- In this research project, the mass accretion model is applied to the ProDiMo model but the models are computed independent from one another. In reality the disk structure and dynamics dictating the mass evolution is coupled to the disk temperature, radiation field and chemistry. This means that even though the ProDiMo model is self-consistent, the combination with the diminishing disk density is not self-consistent. By updating the disk structure between time steps, this is in principle possible.
- Furthermore, it was shown that the region between 1 AU and 4.8 AU has a very high C/O ration in the gas due to the depletion of mostly O-bearing species. Especially in the mid-plane. This is not necessarily wrong, but it is worth investigating for further development of planet formation models with ProDiMo.
- The formation model was applied to a single ProDiMo model AA Tau because it is close to a standard disk model. But there are numerous other observed disks that are fitted, or could be

fitted by ProDiMo. By applying it to variety of observed disks, a larger variety of planets could be found.

- For the model, changing the parameters is easy. However, if the Z_0 and $\epsilon_{g,d}$ have to be so delicately balanced in real disks, this either means that the parameters are correlated so that the formation of gas giants occurs often, or that gas giant formation should be rare. So the delicate balance between Z_0 and $\epsilon_{g,d}$ is also worth investigating.
- The C/O ratio is not the only composition parameter that can say something about the formation pathway. Other chemical indicators are O/H, C/H and H₂O/H₂. In addition the combination of these indicators can also be useful. If for example the C/O is super-stellar, but the O/H is sub-stellar. This can constrain not only the
- The planet core, and the gas giant were now assumed to be stationary during planet formation. However, migration during formation may also play a role in both the total accreted core mass and the composition it accretes. Moreover, interactions with the core will lead to a different pebble flux Morbidelli and Nesvorny (2012).

All in all, the research questions have been answered. But, as stated in the introduction; besides the answers to the questions, more questions to be answered have been found.

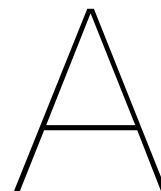
Bibliography

- Andrews, S. M. and Williams, J. P., *High-resolution Submillimeter Constraints on Circumstellar Disk Structure*, *The Astrophysical Journal* **659**, 705 (2007).
- Andrews, S. M., Wilner, D. J., Hughes, A. M., Qi, C., and Dullemond, C. P., *Protoplanetary Disk Structures in Ophiuchus*, *The Astrophysical Journal* **700**, 1502 (2009).
- Andrews, S. M., Wilner, D. J., Zhu, Z., *et al.*, *Ringed Substructure and a Gap at 1 AU in the Nearest Protoplanetary Disk*, *The Astrophysical Journal Letters* **820**, 5 (2016).
- Birnstiel, T., Klahr, H., and Ercolano, B., *A simple model for the evolution of the dust population in protoplanetary disks*, *Astronomy & Astrophysics* **539**, 148 (2012).
- Bouvier, J., Chelli, A., Allain, S., *et al.*, *Magnetospheric accretion onto the T Tauri star AA Tauri I. Constraints from multisite spectrophotometric monitoring*, *Astronomy & Astrophysics* **349**, 619 (1999).
- Brewer, J. M., Fischer, D. A., and Madhusudhan, N., *C/O and O/H Ratios Suggest Some Hot Jupiters Originate Beyond the Snow Line*, *The Astronomical Journal* **153**, 83 (2017).
- Chambers, J. E., *Planetary Migration: What Does It Mean for Planet Formation?* *Annual Review of Earth and Planetary Sciences* **37**, 321 (2009).
- Chiang, E. I. and Goldreich, P., *Spectral Energy Distributions of T Tauri Stars With Passive Circumstellar Disks*, *The Astrophysical Journal* **490**, 368 (1997).
- Cridland, A. J., Pudritz, R. E., and Alessi, M., *Composition of Early Planetary Atmospheres I: Connecting Disk Astrochemistry to the Formation of Planetary Atmospheres*, *Monthly Notices of the Royal Astronomical Society* **461**, 3274 (2016), arXiv:arXiv:1605.09407v2 .
- Cridland, A. J., Pudritz, R. E., Birnstiel, T., Ilesedore Cleaves, L., and Bergin, E. A., *Composition of Early Planetary Atmospheres II: Coupled Dust and Chemical Evolution in Protoplanetary Disks*, *Monthly Notices of the Royal Astronomical Society* **469**, 3910 (2017), arXiv:arXiv:1705.02381v1 .
- Cridland, A. J., Eistrup, C., and Van Dishoeck, E. F., *Connecting planet formation and astrochemistry Refractory carbon depletion leading to super-stellar C/O in giant planetary atmospheres*, *Astronomy & Astrophysics* (2019), arXiv:1901.08896v1 .
- Cuppen, H. M., Walsh, C., Lamberts, T., *et al.*, *Grain Surface Models and Data for Astrochemistry*, *Space Science Reviews* **212**, 1 (2017).
- de Gouveia Dal Pino, E. M., *Cosmic magnetic fields*, in *Physica B: Physics of Condensed Matter*, Vol. 211 (AIP, 1995) pp. 306–315, arXiv:0603065 [astro-ph] .
- Eistrup, C., Walsh, C., and Van Dishoeck, E. F., *Setting the volatile composition of (exo)planet-building material Does chemical evolution in disk midplanes matter?* *Astronomy & Astrophysics* **595**, 83 (2016).
- Eistrup, C., Walsh, C., and Van Dishoeck, E. F., *Molecular abundances and C/O ratios in chemically evolving planet-forming disk midplanes*, *Astronomy & Astrophysics* **613**, 14 (2018), arXiv:1709.07863v1 .
- Ferreira, J., Pelletier, G., and Appl, S., *Reconnection X-winds: spin-down of low-mass protostars*, *Monthly Notices of the Royal Astronomical Society* **312**, 387 (2000).
- Ferrière, K. M., *The interstellar environment of our galaxy*, *Reviews of Modern Physics* **73**, 1031 (2001), arXiv:0106359 [astro-ph] .

- Fitzpatrick, E. L. and L., E., *Correcting for the Effects of Interstellar Extinction*, The Publications of the Astronomical Society of the Pacific **111**, 63 (1998), arXiv:9809387 [astro-ph] .
- Fraser, H. J., Hill, C. R., Blum, J., and Heisselmann, D., *Building Small Icy Bodies: the Process of Icy Grain Aggregation - NASA/ADS*, in *IAU General Assembly (2015)* p. 2255485.
- Graedel, T. E., Laboratories, B., Langer, W. D., and Frerking, M. A., *The Kinetic Chemistry of Dense Interstellar Clouds the NASA Astrophysics Data System*, The Astrophysical Journal Supplement Series **32**, 321 (1982).
- Greaves, J. S., *Dense gas discs around T Tauri stars*, Monthly Notices of the Royal Astronomical Society **351**, 99 (2004).
- Güdel, M., Briggs, K. R., Arzner, K., et al., *The XMM-Newton Extended Survey of the Taurus Molecular Cloud (XEST)*, Astronomy & Astrophysics **468**, 353 (2007).
- Henning, T. and Semenov, D., *Chemistry in protoplanetary disks*, Chemical Reviews **113**, 9016 (2013), arXiv:1011.4770 .
- Ida, S. and Lin, D. N. C., *Toward a Deterministic Model of Planetary Formation. I. A Desert in the Mass and Semimajor Axis Distributions of Extrasolar Planets*, The Astrophysical Journal **604**, 388 (2004), arXiv:0312144 [astro-ph] .
- Johansen, A. and Lambrechts, M., *Forming Planets via Pebble Accretion*, Annual Review of Earth and Planetary Sciences **45**, 359 (2017).
- Kamp, I., Thi, W.-F., Woitke, P., et al., *Consistent dust and gas models for protoplanetary disks II. Chemical networks and rates*, Astronomy & Astrophysics **607**, 23 (2017), arXiv:1707.07281v1 .
- Kenyon, S. J. and Hartmann, L., *Spectral Energy Distributions of T Tauri Stars: Disk Flaring and Limits on Accretion*, The Astrophysical Journal **323**, 714 (1987).
- Kokubo, E. and Ida, S., *Formation of Protoplanet Systems and Diversity of Planetary Systems*, The Astrophysical Journal **581**, 666 (2002).
- Lambrechts, M. and Johansen, A., *Rapid growth of gas-giant cores by pebble accretion*, Astronomy & Astrophysics **544**, 32 (2012).
- Lambrechts, M. and Johansen, A., *Forming the cores of giant planets from the radial pebble flux in protoplanetary discs*, Astronomy & Astrophysics **572**, 107 (2014).
- Lambrechts, M., Johansen, A., and Morbidelli, A., *Separating gas-giant and ice-giant planets by halting pebble accretion*, Astronomy & Astrophysics **572**, 35 (2014).
- Lewis, J. S., *The temperature gradient in the solar nebula*. Science (New York, N.Y.) **186**, 440 (1974).
- Lissauer, J. J. and de Pater, I., *Fundamental Planetary Science* (Cambridge University Press, New York, NY, USA, 2013) p. 583, arXiv:1011.1669v3 .
- Lissauer, J. J., *Formation of the Outer Planets*, Space Science Reviews **116**, 11 (2005).
- Lodders, K., *Solar System Abundances and Condensation Temperatures of the Elements*, The Astrophysical Journal **591**, 1220 (2003).
- Madhusudhan, N., Agúndez, M., Moses, J. I., et al., *Exoplanetary Atmospheres-Chemistry, Formation Conditions, and Habitability*, Space Science Reviews **205**, 285 (2016a).
- Madhusudhan, N., Bitsch, B., Johansen, A., and Eriksson, L., *Preprint*, Tech. Rep. (2016) arXiv:1611.03083v2 .
- Mathis, J. S., Rumpl, W., and Nordsieck, K. H., *The Size Distribution of Interstellar Grains*, The Astrophysical Journal **217**, 425 (1977).
- Mayor, M. and Queloz, D., *A Jupiter-mass companion to a solar-type star*, Nature **378**, 355 (1995).

- Mcelroy, D., Walsh, C., Markwick, A. J., *et al.*, *The UMIST database for astrochemistry 2012*, *Astronomy & Astrophysics* **550**, 36 (2013).
- Mohr, P. J., Taylor, B. N., and Newell, D. B., *CODATA Recommended Values of the Fundamental Physical Constants: 2006*, *Review of Modern Physics* **80**, 633 (2007), arXiv:0801.0028 .
- Montmerle, T., Augereau, J.-C., Chaussidon, M., *et al.*, 3. *Solar System Formation and Early Evolution: the First 100 Million Years*, *Earth, Moon, and Planets* **98**, 39 (2006).
- Morbidelli, A. and Nesvorny, D., *Dynamics of pebbles in the vicinity of a growing planetary embryo: hydro-dynamical simulations*, *Astronomy & Astrophysics* **546**, 18 (2012).
- Murray, N., *Star Formation Efficiencies and Lifetimes of Giant Molecular Clouds in the Milky Way*, *The Astrophysical Journal* **729**, 133 (2011).
- Muzerolle, J., Calvet, N., Hartmann, L., and Alessio, P. D. ., *Unveiling the Inner Disk Structure of T Tauri Stars*, *The Astrophysical Journal* **597**, 149 (2003).
- Natta, A., Testi, L., Calvet, N., *et al.*, *Dust in Protoplanetary Disks: Properties and Evolution*, in *Protostars and Planets V*, edited by Reipurth, V. B., Jewitt, D., and Keil, K. (University of Arizona Press, Tucson, 2007) Chap. Dust in Pr, pp. 767–781.
- Öberg, K. I., Murray-Clay, R. A., and Bergin, E. A., *The Effects of Snowlines on C/O in Planetary Atmospheres*, *The Astrophysical Journal* **743**, L16 (2011).
- Ormel, C. W., *The Emerging Paradigm of Pebble Accretion*, in *Formation, Evolution, and Dynamics of Young Solar Systems*, edited by Pessah, M. and Gressel, O. (Springer, Cham, Copenhagen, Denmark, 2017) Chap. The Emergi, pp. 197–228.
- O'sullivan, M., Truss, M., Walker, C., *et al.*, *Modelling the photopolarimetric variability of AA Tau*, *Monthly Notices of the Royal Astronomical Society* **358**, 632 (2005).
- Pontoppidan, K. M., *Spatial mapping of ices in the Ophiuchus-F core A direct measurement of CO depletion and the formation of CO 2*, *Astronomy & Astrophysics* **453**, 47 (2006).
- Rab, C., *PROtoplanetary Disk MOdel*, (2018).
- Richer, H. B., Anderson, J., Brewer, J., *et al.*, *Probing the faintest stars in a globular star cluster*. *Science* (New York, N.Y.) **313**, 936 (2006).
- Savage, B. D. and Sembach, K. R., *Interstellar Abundances From Absorption-Line Observations With the Hubble Space Telescope*, *Annual Review of Earth and Planetary Sciences* **34**, 279 (1996).
- Shu, F. H., Adams, F. C., and Lizano, S., *Star Formation in Molecular Clouds: Observation and Theory*, *Annual Review of Astronomy & Astrophysics* **25**, 23 (1987), arXiv:arXiv:1011.1669v3 .
- Wang, H., Bell, R. C., Iedema, M. J., Tsekouras, A. A., and Cowin, J. P., *Sticky Ice Grains Aid Planet Formation: Unusual Properties of Cryogenic Water Ice*, *The Astrophysical Journal* **620**, 1027 (2005).
- Weidenschilling, S. J., *Aerodynamics of solid bodies in the solar nebula*, *Monthly Notices of the Royal Astronomical Society* **180**, 57 (1977a).
- Weidenschilling, S. J., *The distribution of mass in the planetary system and solar nebula*, *Astrophysics and Space Science* **51**, 153 (1977b).
- Weingartner, J. C. and Draine, B. T., *Dust Grain-Size Distributions and Extinction in the Milky Way, Large Magellanic Cloud, and Small Magellanic Cloud*, *The Astrophysical Journal* **548**, 296 (2001), arXiv:0008146 [astro-ph] .
- Williams, J. P. and Cieza, L. A., *Protoplanetary Disks and Their Evolution*, *Annual Review of Astronomy and Astrophysics* **49**, 67 (2011), arXiv:1103.0556 .
- Windmark, F., Birnstiel, T., Güttler, C., *et al.*, *Planetesimal formation by sweep-up: how the bouncing barrier can be beneficial to growth*, *Astronomy & Astrophysics* **540**, 73 (2012).

- Woitke, P., Kamp, I., and Thi, W.-F., *Radiation thermo-chemical models of protoplanetary disks I. Hydrostatic disk structure and inner rim*, *Astronomy & Astrophysics* **501**, 383 (2009).
- Woitke, P., Min, M., Pinte, C., *et al.*, *Consistent dust and gas models for protoplanetary disks. I. Disk shape, dust settling, opacities, and PAHs*, *Astronomy & Astrophysics* **586** (2016), 10.1051/0004-6361/201526538, arXiv:1511.03431 .
- Woitke, P., Kamp, I., Antonellini, S., *et al.*, *Consistent dust and gas models for protoplanetary disks III. Models for selected objects from the FP7 DIANA project*, *Publications of the Astronomical Society of the Pacific* **131**, 064301 (2019), arXiv:1812.02741v1 .
- Woitke, P., *A typical T Tauri ProDiMo model*, (2013).



Input files ProDiMo

These are the input files of the model considered in this thesis. They are modified to include time dependency and surface chemistry. The original files are found on http://www-star.st-and.ac.uk/~pw31/DIANA/SEDfit/AATau_model_index.html [date accessed:2-7-2019].

Elements.in

```
13
H 12.00 1.0079
He 10.984 4.0026
C 8.14 12.011
N 7.90 14.007
O 8.48 15.999
Ne 7.95 20.180
Na 3.36 22.990
Mg 4.03 24.305
Si 4.24 28.086
S 5.27 32.066
Ar 6.08 39.948
Fe 3.24 55.845
D 7.18 3.0219
0.1

Without PAH
PAH 5.48 666.736

Comments for the selected Abundances
*****
The values for He and Ne are from Lodders (2003) Tabel 2 Recommended Elemental Abundances of
↳ the Proto-Sun
All other values are from Savage & Sembach (1996) Table 5 Ophiuchi cool.
The metals (all Elements except H,He,C,N,O,Ne,Ar,) are depleted further by a factor of 100
↳ following Graedel (1982) (low metals)

The abundances in "normal numbers" (relative to H)
He 9.64E-2
C 1.38E-4
N 7.94E-5
O 3.02E-4
Ne 8.91E-5
Na 2.29E-9
Mg 1.07E-8
Si 1.74E-8
S 1.86E-7
Ar 1.20E-6
Fe 1.74E-9
```

Parameters.in

```

-----
*** standard DIANA parameter input-file for ProDiMo ***
*** works with small and large DIANA chemical standards ***
-----

----- star and irradiation -----
0.85      ! Mstar      [Msun]   : stellar mass
0.7799    ! Lstar      [Lsun]   : stellar luminosity
4013      ! Teff        [K]      : stellar effective temperature
0.004     ! fUV         [-]      : LUV/Lstar
3.0       ! pUV         [-]      : UV powerlaw exponent
.true.    ! Xrays       [-]      : use Xray chemistry and heating?
3.641e+30 ! Xray_Lum     [erg/s]   : X-ray luminosity
40793350  ! Xray_Temp    [K]      : X-ray emission temperature
1.7E-17   ! CRI          [1/s]    : cosmic ray ionisation of H2
1.0       ! CHI_ISM     [-]      : strength of incident vertical UV

----- dust parameters -----
2.094     ! rho_gr       [g/cm^3]: dust grain material mass density
4.18124539E-01 ! amin       [mic]   : minimum dust particle size
1.12302607E+03 ! amax       [mic]   : maximum dust particle size
3.66589146E+00 ! apow       [-]     : dust size distr f(a)~a^-apow
2          ! settle_method : dust settling (Dubrulle et al. 1995)
5.26270788E-02 ! a_settle   : turbulence alpha
0.8       ! hollow_sphere : max hollow volume ratio
dust_opacity_list2.txt ! dust_opacity_list_file
3         ! NDUST       : number of selected dust species
0.611215414249118 Mg0.7Fe0.3SiO3[s]
0.138784585750882 amC-Zubko[s]
0.25      vacuum[s]

----- PAH parameters -----
.false.   ! PAH_in_RT   : are PAH opacities included in rad.trans.?
.false.   ! PAH_from_RT : PAH heating from cross-sections?

----- gas parameters -----
0.01      ! dust_to_gas [-] : the dust-to-gas mass ratio
0.2       ! ChemHeatFac [-] : efficiency of chemical heating
0.15      ! v_turb      [km/s]  : turbulent Doppler width
.true.    ! UMIST2012
.true.    ! Eads_from_file : use UMIST2012 adsorption energies
onlyadd   ! handle_UMIST : handle UMIST-data (erase/overwrite/onlyadd)
0         ! num_noerase  : exceptions from erasing UMIST data

----- Surface chemistry -----
.true.    ! chemanalysis
.true.    ! surface_chemistry
0.01     ! evap_fac
.true.    ! tunnelling
.true.    ! Eley_Rideal
.true.    ! H2_no_surf_Cazaux : keep old H2 Cazaux formation, suppress H# + H# -> H2

----- disk mass & shape -----
1.31248130E-02 ! Mdisk      [Msun] : disk mass
.false.       ! soft_edges : add confining boundary layers?
.false.       ! solve_diskstruc : solve the vertical hydrostatic eq.?
.true.       ! MCFOST_LIKE : parametric disk structure like in MCFOST?
1.45127599E-01 ! Rin        [AU]   : inner disk radius
5.00000000E+01 ! Rtaper     [AU]   : tapering-off radius
3.00000000E+02 ! Rout       [AU]   : outer disk radius
1.0          ! epsilon    [-]    : column density exponent
1.09031647E+01 ! MCFOST_H0  [AU]   : scale height ...
1.00000000E+02 ! MCFOST_RREF [AU]   : ... belonging to reference radius
1.15733100E+00 ! MCFOST_BETA : flaring power

----- the big molecules -----
.true.    ! H2O_rovibration : big ro-vib H2O models?
.true.    ! H2O_Daniel2011 : new H2O collision rates

```

```

----- dimensions -----
70      ! NXX      (increase to ~150 for publications!)
60      ! NZZ      (increase to ~100 for publications!)
10      ! Ninner
10      ! NnewWall
0.5     ! NXratio
40      ! NLAM
.true.  ! refine_Spitzer
9       ! NUV
3       ! N1UV
19      ! Ntheta
11      ! Nphi
50      ! RTitmax
3.0     ! tau_cutoff

----- accelerations -----
.true.  ! parallel_chem
.false. ! parallel_debug
.false. ! ignore_Tg_midplane
.false. ! use_chemsol

----- image and SED parameters -----
.true.  ! calcSED      : calculate SED and images?
.true.  ! monoSED      : use monochromatic mode?
300     ! NlamSED      : number of lambda gridpoints
0.0912  ! lminSED      : minimum lambda[mic]
10000.0 ! lmaxSED      : minimum lambda[mic]
140.0   ! dist        [pc] : distance
70.0    ! incl        [deg] : inclination (0=face-on)
.false. ! compute_visibilities

----- line transfer? -----
.true.  ! line_transfer : calculate line transfer?
.false. ! write_pop     : write output for immediate line transfer?
.false. ! immediate_lines : line RT directly after init?
.false. ! line_cube     : 3D-line cube output?
.false. ! FLiTs         : want to run FLiTs afterwards?
300     ! line_Ndisk
144     ! line_Ntheta
301     ! line_image_side_Npix

----- time-dependent chemistry parameters
.true.  ! molecular_cloud
.false. ! mc_only
1.0     ! CHI1_mc : UV field in band 1
1.0     ! CHI2_mc : Uv field in band 2  400 Habart
2e4     ! nH_mc
10.0    ! Tg_mc
10.0    ! Td_mc
10.0    ! Av_mc
0.1     ! a1_mc [mic]
1.0     ! fPAH_mc
66      ! N_age_mc
1e-20 1e-15 1e-10 1e-5 0.0001 0.00100000 0.00146780 0.00215443 0.00316228 0.00464159
↪ 0.00681292 0.0100000 0.0146780 0.0215443 0.0316228 0.0464159
↪ 0.0681292 0.100000 0.146780 0.215443 0.316228 0.464159
↪ 0.681292 1.00000 1.46780 2.15443 3.16228 4.64159 6.81292
↪ 10.0000 14.6780 21.5444 31.6228 46.4159 68.1292
↪ 100.000 146.780 215.444 316.228 464.159 681.292 1000.00
↪ 1467.80 2154.44 3162.28 4641.59 6812.92 10000.0
↪ 14678.0 21544.4 31622.8 46415.9 68129.2 100000. 146780.
↪ 215443. 316228. 464159. 681292. 1.00000e+06 1.46780e+06 2.15443
↪ e+06 3.16228e+06 4.64159e+06 6.81292e+06 1.00000e+07
1.7E-17 ! CRI_mc
.false. ! time_dependent : solve time-dependent disk chemistry?
.true.  ! time_chem_disk
9       ! N_age : no of successive output ages
1 1e5 2e5 4e5 8e5 1e6 2e6 4e6 7e6 : disk ages in years
.true.  ! numericalJacobian

```

```
.true.      ! DVODEF90

----- tolerances -----
0.05       ! tol_convergence   : convergence criterion for global interation
1.0E-8     ! tol_diskstruc    : rel.&abs. tolerance for vertical disk struc
1.0E-8     ! temp_precis      : rel. precision in T-determination
1.0E-9     ! chem_precis      : precision in solve_chemistry
2.0E-5     ! rtol_chem         : rel. tolerance for advance_chemistry
1.0E-99    ! atol_chem         : abs. tolerance for advance_chemistry
20.0      ! cputime_max [s]  : max. CPU time for advance_chemistry

----- switches -----
0          ! verbose_level    : how much output? (-1...4)
.true.     ! solve_temp        : solve the heating/cooling balance?
.false.    ! restart           : run from restart?
.true.     ! radtrans          : continuum radiative transfer?
.true.     ! chi_from_RT       : calculate chi from UV rad. transfer?
.true.     ! Td_from_RT        : calculate dust temp. from rad. transfer?
.true.     ! Jback_from_RT     : calculate background Jnu from rad. transfer?
```

Species.in

H	C ₄	NH ₃ ⁺	SiH ₃	C ₃ #
H ⁺	C ₄ ⁺	NH ₄ ⁺	SiH ₃ ⁺	C ₃ H#
Hm	C ₄ H ⁺	N ₂	SiH ₄	C ₃ H ₂ #
H ₂	CN	N ₂ ⁺	SiH ₄ ⁺	C ₄ #
H ₂ ⁺	CN ⁺	HN ₂ ⁺	SiH ₅ ⁺	CN#
H ₃ ⁺	HCN	NO	SiC	HCN#
H ₂ exc	HCN ⁺	NO ⁺	SiC ⁺	HNC#
D	HCNH ⁺	NO ₂	HCSi ⁺	H ₂ CN#
D ⁺	HNC	NO ₂ ⁺	SiN	OCN#
HD	H ₂ CN	HNO	SiN ⁺	CO#
HD ⁺	OCN	HNO ⁺	HNSi ⁺	HCO#
He	OCN ⁺	H ₂ NO ⁺	SiO	CO ₂ #
He ⁺	CO	NS	SiO ⁺	C ₂ O#
HeH ⁺	CO ⁺	NS ⁺	SiOH ⁺	H ₂ CO#
C	HCO	HNS ⁺	SiS	CH ₃ O#
C ⁺	HCO ⁺	O	SiS ⁺	CH ₂ OH#
C ⁺⁺	CO ₂	O ⁺	HSiS ⁺	CH ₃ OH#
CH	CO ₂ ⁺	O ⁺⁺	Mg	CS#
CH ⁺	HCO ₂ ⁺	OH	Mg ⁺	HCS#
CH ₂	C ₂ O	OH ⁺	Mg ⁺⁺	H ₂ CS#
CH ₂ ⁺	C ₂ O ⁺	H ₂ O	Fe	OCS#
CH ₃	HC ₂ O ⁺	H ₂ O ⁺	Fe ⁺	N#
CH ₃ ⁺	H ₂ CO	H ₃ O ⁺	Fe ⁺⁺	NH#
CH ₄	H ₂ CO ⁺	O ₂	Na	NH ₂ #
CH ₄ ⁺	CH ₃ O	O ₂ ⁺	Na ⁺	NH ₃ #
CH ₅ ⁺	H ₃ CO ⁺	O ₂ H	Na ⁺⁺	N ₂ #
C ₂	CH ₂ OH	O ₂ H ⁺	Ne	NO#
C ₂ ⁺	CH ₃ OH	H ₂ O ₂	Ne ⁺	NO ₂ #
C ₂ H	CH ₃ OH ⁺	SO	Ne ⁺⁺	HNO#
C ₂ H ⁺	CH ₃ OH ₂ ⁺	SO ⁺	Ar	NS#
C ₂ H ₂	CS	SO ₂	Ar ⁺	O#
C ₂ H ₂ ⁺	CS ⁺	SO ₂ ⁺	Ar ⁺⁺	OH#
C ₂ H ₃	HCS	HSO ₂ ⁺	H#	H ₂ O#
C ₂ H ₃ ⁺	HCS ⁺	S	Mg#	O ₂ #
C ₂ H ₄	H ₂ CS	S ⁺	Fe#	O ₂ H#
C ₂ H ₄ ⁺	H ₂ CS ⁺	S ⁺⁺	Na#	H ₂ O ₂ #
C ₂ H ₅	H ₃ CS ⁺	HS	C#	SO#
C ₂ H ₅ ⁺	OCS	HS ⁺	CH#	SO ₂ #
C ₂ H ₆	OCS ⁺	H ₂ S	CH ₂ #	S#
C ₂ H ₆ ⁺	HOCS ⁺	H ₂ S ⁺	CH ₃ #	HS#
C ₂ H ₇ ⁺	N	H ₃ S ⁺	CH ₄ #	H ₂ S#
C ₃	N ⁺	Si	C ₂ #	Si#
C ₃ ⁺	N ⁺⁺	Si ⁺	C ₂ H#	SiH#
C ₃ H	NH	Si ⁺⁺	C ₂ H ₂ #	SiH ₂ #
C ₃ H ⁺	NH ⁺	SiH	C ₂ H ₃ #	SiH ₃ #
C ₃ H ₂	NH ₂	SiH ⁺	C ₂ H ₄ #	SiH ₄ #
C ₃ H ₂ ⁺	NH ₂ ⁺	SiH ₂	C ₂ H ₅ #	SiC#
C ₃ H ₃ ⁺	NH ₃	SiH ₂ ⁺	C ₂ H ₆ #	SiN#
SiS#	SiO#			

Table A.1: List of the species considered in the model AA Tau by ProDiMo.

B

Core and atmosphere compositions

B.1. Core compositions

	Pebbles						Planetesimals								
	0.000	0.000	0.000	0.000	0.000	0.000	0.000	0.000	0.000	0.000	0.000	0.000	0.000	0.000	0.000
Mg#	0.000	0.000	0.000	0.000	0.000	0.000	0.000	0.000	0.000	0.000	0.000	0.000	0.000	0.000	0.000
Fe#	0.000	0.000	0.000	0.000	0.000	0.000	0.000	0.000	0.000	0.000	0.000	0.000	0.000	0.000	0.000
Na#	0.000	0.000	0.000	0.000	0.000	0.000	0.000	0.000	0.000	0.000	0.000	0.000	0.000	0.000	0.000
C#	0.000	0.000	0.000	0.000	0.000	0.000	0.000	0.000	0.000	0.000	0.000	0.000	0.000	0.000	0.000
CH#	0.000	0.000	0.000	0.000	0.000	0.000	0.000	0.000	0.000	0.000	0.000	0.000	0.000	0.000	0.000
CH₂#	0.000	0.000	0.000	0.000	0.000	0.000	0.000	0.000	0.000	0.000	0.000	0.000	0.000	0.000	0.000
CH₃#	0.000	0.000	0.000	0.000	0.000	0.000	0.000	0.000	0.000	0.000	0.000	0.000	0.000	0.000	0.000
CH₄#	4.858	7.919	9.711	9.747	9.801	10.018	0.000	0.000	0.000	0.000	0.000	0.000	0.000	0.003	1.291
C₂#	0.000	0.000	0.000	0.000	0.000	0.000	0.000	0.000	0.000	0.000	0.000	0.000	0.000	0.000	0.000
C₂H#	0.000	0.000	0.000	0.000	0.000	0.000	0.000	0.000	0.000	0.000	0.000	0.000	0.000	0.000	0.000
C₂H₂#	0.000	0.000	0.000	0.000	0.000	0.000	0.000	0.000	0.000	0.000	0.050	0.000	0.000	0.000	0.000
C₂H₃#	0.000	0.000	0.000	0.000	0.000	0.000	0.000	0.000	0.000	0.000	0.001	0.005	0.000	0.000	0.000
C₂H₄#	0.000	0.000	0.000	0.000	0.000	0.000	0.000	0.000	0.000	0.006	0.068	0.009	0.000	0.000	0.000
C₂H₅#	0.000	0.000	0.000	0.000	0.000	0.000	0.000	0.000	0.000	0.000	0.087	0.010	0.000	0.000	0.000
C₂H₆#	1.616	1.374	0.710	0.705	0.696	0.659	0.000	0.000	0.000	0.000	0.017	1.140	0.573	1.141	0.043
C₃#	0.000	0.000	0.000	0.000	0.000	0.000	0.000	0.000	0.000	0.000	0.002	0.000	0.000	0.000	0.000
C₃H#	0.000	0.000	0.000	0.000	0.000	0.000	0.000	0.000	0.000	0.001	0.011	0.000	0.000	0.000	0.000
C₃H₂#	0.131	0.121	0.099	0.099	0.099	0.098	0.000	0.000	0.000	0.149	1.575	0.154	0.158	0.162	0.129
C₄#	0.008	0.006	0.006	0.006	0.006	0.006	0.000	0.000	0.000	0.011	0.015	0.015	0.015	0.015	0.011
CN#	0.394	0.497	0.524	0.529	0.535	0.560	0.000	0.000	0.000	0.000	0.000	0.000	0.000	0.004	0.099
HCN#	4.193	3.410	3.026	3.016	3.002	2.947	0.000	0.000	0.000	0.000	0.001	3.949	5.789	5.765	5.512
HNC#	0.601	0.640	0.707	0.707	0.707	0.708	0.000	0.000	0.000	0.000	0.000	2.145	1.544	0.591	0.573
H₂CN#	0.094	0.519	0.886	0.880	0.873	0.846	0.000	0.000	0.000	0.000	0.000	0.000	0.000	0.000	0.000
OCN#	0.000	0.000	0.000	0.000	0.000	0.000	0.000	0.000	0.000	0.000	0.000	0.000	0.000	0.000	0.000
CO#	0.058	0.145	0.034	0.034	0.033	0.031	0.000	0.000	0.000	0.000	0.000	0.000	0.000	0.000	0.000
HCO#	0.000	0.000	0.000	0.000	0.000	0.000	0.000	0.000	0.000	0.000	0.000	0.000	0.000	0.000	0.000
CO₂#	0.438	0.224	0.058	0.057	0.056	0.051	0.000	0.000	0.000	0.000	0.029	0.038	0.031	0.031	0.030
C₂O#	0.000	0.000	0.000	0.000	0.000	0.000	0.000	0.000	0.000	0.000	0.000	0.000	0.000	0.000	0.000
H₂CO#	0.024	0.030	0.009	0.009	0.009	0.008	0.000	0.000	0.000	0.000	0.000	0.000	0.000	0.000	0.000
CH₃O#	0.000	0.000	0.000	0.000	0.000	0.000	0.000	0.000	0.000	0.000	0.000	0.000	0.000	0.000	0.000
CH₂OH#	0.000	0.000	0.000	0.000	0.000	0.000	0.000	0.000	0.000	0.001	0.000	0.000	0.000	0.000	0.000
CH₃OH#	31.498	25.889	23.863	23.816	23.750	23.475	45.827	45.105	42.711	40.930	41.728	40.960	40.960	40.960	40.960
CS#	0.000	0.001	0.000	0.000	0.000	0.000	0.000	0.000	0.000	0.000	0.000	0.000	0.000	0.000	
HCS#	0.000	0.000	0.000	0.000	0.000	0.000	0.000	0.000	0.000	0.000	0.000	0.000	0.000	0.000	
H₂CS#	0.000	0.000	0.000	0.000	0.000	0.000	0.000	0.000	0.000	0.001	0.000	0.000	0.000	0.000	

Table B.1 continued from previous page

Species	Pebbles						Planetesimals					
	$r_c = 1$	$r_c = 2$	$r_c = 4.8$	$r_c = 8$	$r_c = 12$	$r_c = 25$	$r_c = 1$	$r_c = 2$	$r_c = 4.8$	$r_c = 8$	$r_c = 12$	$r_c = 25$
OCS#	0.000	0.000	0.000	0.000	0.000	0.000	0.000	0.000	0.000	0.000	0.000	0.000
N#	0.000	0.000	0.000	0.000	0.000	0.000	0.000	0.000	0.000	0.000	0.000	0.000
NH#	0.000	0.000	0.000	0.000	0.000	0.000	0.000	0.000	0.000	0.000	0.000	0.000
NH ₂ #	0.002	0.001	0.000	0.000	0.000	0.000	0.000	0.044	0.026	0.002	0.000	0.000
NH ₃ #	4.426	4.665	5.116	5.120	5.126	5.150	9.086	8.842	7.974	10.513	7.858	9.437
N ₂ #	4.615	4.834	4.518	4.515	4.512	4.499	0.000	0.000	0.000	0.000	0.000	0.000
NO#	0.016	0.004	0.007	0.007	0.007	0.006	0.000	0.000	0.000	0.002	0.014	0.000
NO ₂ #	0.063	0.053	0.056	0.055	0.055	0.053	0.000	0.000	0.004	0.001	0.000	0.000
HNO#	3.638	3.313	3.058	3.065	3.074	3.109	0.000	0.000	0.000	0.878	4.381	4.312
NS#	0.000	0.000	0.000	0.000	0.000	0.000	0.000	0.000	0.000	0.000	0.000	0.000
O#	0.000	0.000	0.000	0.000	0.000	0.000	0.000	0.000	0.000	0.000	0.000	0.000
OH#	0.006	0.002	0.009	0.009	0.009	0.009	0.000	0.000	0.000	0.000	0.000	0.000
H ₂ O#	43.295	46.338	47.591	47.610	47.639	47.756	44.911	44.145	41.801	39.556	38.296	37.593
O ₂ #	0.002	0.001	0.001	0.001	0.001	0.001	0.000	0.000	0.000	0.000	0.000	0.000
O ₂ H#	0.000	0.000	0.000	0.000	0.000	0.000	0.000	0.000	0.000	0.000	0.000	0.000
H ₂ O ₂ #	0.014	0.006	0.002	0.002	0.002	0.002	0.000	0.000	0.002	0.000	0.000	0.000
SO#	0.001	0.001	0.001	0.001	0.001	0.001	0.000	0.000	0.002	0.002	0.002	0.002
SO ₂ #	0.001	0.001	0.001	0.001	0.000	0.000	0.007	0.001	0.001	0.001	0.001	0.001
S#	0.000	0.000	0.000	0.000	0.000	0.000	0.000	0.000	0.000	0.000	0.000	0.000
HS#	0.000	0.000	0.000	0.000	0.000	0.000	0.000	0.000	0.000	0.000	0.000	0.000
H ₂ S#	0.006	0.006	0.006	0.006	0.006	0.006	0.000	0.003	0.006	0.005	0.006	0.005
Si#	0.000	0.000	0.000	0.000	0.000	0.000	0.000	0.000	0.000	0.000	0.000	0.000
SiH#	0.000	0.000	0.000	0.000	0.000	0.000	0.000	0.000	0.000	0.000	0.000	0.000
SiH ₂ #	0.000	0.000	0.000	0.000	0.000	0.000	0.000	0.000	0.000	0.000	0.000	0.000
SiH ₃ #	0.000	0.000	0.000	0.000	0.000	0.000	0.000	0.000	0.000	0.000	0.000	0.000
SiH ₄ #	0.000	0.000	0.000	0.000	0.000	0.000	0.000	0.000	0.000	0.000	0.000	0.000
SiC#	0.000	0.000	0.000	0.000	0.000	0.000	0.000	0.000	0.000	0.000	0.000	0.000
SiN#	0.000	0.000	0.000	0.000	0.000	0.000	0.000	0.000	0.000	0.000	0.000	0.000
SiO#	0.001	0.001	0.001	0.001	0.001	0.001	0.000	0.001	0.001	0.001	0.001	0.001
SiS#	0.000	0.000	0.000	0.000	0.000	0.000	0.000	0.000	0.000	0.000	0.000	0.000

Table B.1: List of all ice species for cores in percentages.

B.2. Atmosphere compositions

List of all gas species for giant planets

Table B.2: List of the most abundant species in the atmospheres in percentages

	Composition			Composition other than H ₂ and He		
	$r_c = 2$	$r_c = 4.8$	$r_c = 8$	$r_c = 2$	$r_c = 4.8$	$r_c = 8$
H	0.008	0.012	0.017	3.39	8.04	10.75
H₂	72.136	72.183	72.181	-	-	-
D	0.000	0.000	0.000	0.01	0.01	0.02
HD	0.004	0.004	0.004	1.93	2.84	2.76
He	27.640	27.664	27.663	-	-	-
CH₄	0.003	0.000	0.000	1.20	0.13	0.00
C₂H₂	0.001	0.000	0.000	0.64	0.00	0.00
C₂H₆	0.006	0.000	0.000	2.54	0.08	0.00
C₃	0.000	0.000	0.000	0.16	0.00	0.00
C₃H	0.000	0.000	0.000	0.01	0.00	0.00
HCN	0.015	0.000	0.000	6.53	0.12	0.00
HNC	0.009	0.000	0.000	4.08	0.04	0.00
CO	0.004	0.003	0.002	1.57	1.69	1.12
CO₂	0.000	0.000	0.000	0.03	0.00	0.00
N	0.000	0.000	0.000	0.00	0.00	0.01
NH₂	0.000	0.000	0.000	0.00	0.02	0.02
N₂	0.043	0.001	0.001	18.97	0.38	0.44
NO	0.000	0.000	0.000	0.02	0.01	0.06
O	0.000	0.000	0.000	0.05	0.06	0.13
H₂O	0.000	0.000	0.000	0.01	0.04	0.19
O₂	0.000	0.000	0.000	0.02	0.01	0.15
Ne	0.129	0.129	0.129	57.29	84.26	82.15
Ar	0.003	0.003	0.003	1.53	2.25	2.19